2024

Brittle-viscous deformation cycles at the base of the seismogenic zone in the continental crust

Prando, Francesca

UNIVERSITY OF
PLYMOUTH

Brittle-viscous deformation cycles at the base of the seismogenic zone in the continental crust

by

Francesca Prando

A thesis submitted to the University of Plymouth
in partial fulfilment for the degree of

DOCTOR OF PHILOSOPHY

School of Geography, Earth and Environmental Sciences

March 2023

Acknowledgments

The journey leading to the end of the PhD has been a long and winding one, and truly, it might have not been possible without all the people I've met along the way.

First and foremost, I would like to thank my supervisors Prof. Luca Menegon, Prof. Mark Anderson, Prof. Giulio Viola, and Prof. Jussi Mattila, who have given me a great deal of guidance and support throughout the course of this PhD and whose patience, time and tireless enthusiasm I am most grateful for. The experiences of working under their supervision greatly contributed to the researcher and the person that I grew to be. I thank Luca for his support during countless moments of the PhD and for challenging me when I needed to be pushed to take ownership of my work. I'm truly grateful for every time he was available to guide me and his patience in doing so, be it for collecting EBSD maps, networking, or writing. I would like to thank Mark for his countless suggestions in how to interpret the bigger picture of this work, always useful when I got too lost into the details. Further thanks go to Giulio and Jussi, for their availability to answer to my badly written, random e-mails and especially for the support and encouragement shown to me every time we were discussing the PhD progress.

I would like to thank the team that examined my thesis on the 27th of June 2023: Pr. Iain Stewart and Pr. Pietari Skyttä. Thanks to you, my viva was a very pleasant and thrilling discussion! Thank you very much to Dr Sarah Boulton for her role as a Chair.

Special thanks to Prof. Florian Fusseis and Dr. Ian Butler the data acquisition and their help in the processing of the micro-CT dataset at Edinburgh University. I might have rarely left the workstation, but I always felt welcome and received a great support when mostly needed. I would like to thank Prof. Giuliano Laudone, Dr. Katie Jones and Ben Veater for introducing me to the wonderous world of porosity measurements. Thank you for all the support in using the helium pycnometer and mercury porosimeter, for the

answer to the countless doubt in data analysis, and for always being there to open the lab door. All the Plymouth Electron Microscopy Centre (PEMC) staff is greatly thanked for their support with the SEM analyses. Andrea Risplendente is thanked for support with EMPA analysis at the University of Milan. Dr. Luiz Morales is thanked for the help in CL-SEM analysis at ETH Zurich. Many thanks go to Fabrizio Nestola for giving me access to the microRaman spectrometer of the University of Padova.

Further thanks are due to Dr.Jodie Fisher for always having a kind word and the help with the camera's at the optical microscopy lab in the old Fitzroy building and Robert Hall for his patience in checking all the coshh form that I had to fill during the project.

Posiva oy is thanked for the financial support to the PhD project.

I would also like to extend a big thank you to my fellow PhD colleague Barbara, discussing with you the ups and down of Onkalo geology has been an honour. Camille and Louise are especially thanked for their cheers and for being the best women in geosciences sharing the same journey. Hoayda, Mads, Kilian and Marta are thanked for being wonderful housemates, living in Plymouth would have not been the same without you. Thank you to Wycliff, Josh, Symeon, and the visiting Alberto, Simone and Samuele, for sharing this PhD journey and lots of good evening at the JSV.

A special thanks to Giulia, for not only being always an amazing friend, but as usual an inspiring geologist. We both came long way from being in the same group during field work I in Padova, arguing on whether the faults we mapped were connected or not.

To the Simply, the friends back home, an immense thank you for all your support during my life abroad. A thank you to my family that waited patiently while I was going through it all.

Lasty I am extremely grateful to Gabriele, for being my constant support and cheerleader, even when I've been burning in water and drowning in flame. I was always lucky to have you in my life, that will never change. Thank you for everything, I wish you all the best.

Author's Declaration

At no time during the registration for the degree of Doctor of Philosophy has the author been registered for any other University award without prior agreement of the Doctoral College Quality Sub-Committee.

Work submitted for this research degree at the University of Plymouth has not formed part of any other degree either at the University of Plymouth or at another establishment.

A programme of advanced study was undertaken, which included GEES519 Environmental Knowledge: From Field to Stakeholder (17/AU/SB/M)

The following external institutions were visited for research and consultation purposes:

-Edinburgh University (micro-CT)

- Università degli Studi di Milano (microprobe)

-ETH Zurich (CL-SEM)

- Università degli Studi di Padova (microRaman)

This study was financed with the aid of a studentship from the University of Plymouth (School of Geography, Earth and Environmental Sciences) and Posiva Oy.

Publications (or public presentation of creative research outputs):

Prando, F., Menegon, L., Anderson, M., Marchesini, B., Mattila, J., and Viola, G.: Fluid-mediated, brittle–ductile deformation at seismogenic depth – Part 2: Stress history and fluid pressure variations in a shear zone in a nuclear waste repository (Olkiluoto Island, Finland), Solid Earth, 11, 489–511, https://doi.org/10.5194/se-11-489-2020, 2020

Presentations at conferences:

Prando, F., Menegon, L.,Jones, K., Fusseis, F., Anderson, M., Laudone, G.M. Porosity evolution in fault rocks at the brittle ductile transition. Poster presentation, Tectonic Studies Group AGM, University of Hull, UK (2020).

Marchesini, B., Menegon, L., Prando, F., Schwarz, Garofalo, P., Keresztes Schmidt, P., Hattendorf B., Günther D., Viola, G. Evidence of low-temperature plasticity in hydrothermal pyrite. Deformation Mechanisms, Rheology and Tectonics Conference, Tubingen, Germany. (2019)

Menegon, L., Marchesini, B., Prando, F., Garofalo, P., Viola, G., Anderson, M. and Mattila, J. Brittle-viscous oscillations and different slip behaviours in a conjugate set of strike-slip faults. PICO presentation, EGU General Assembly, Vienna, Austria (2018).

Prando, F., Menegon, L., Anderson, M., Viola, G., Mattila, J. Ductile-brittle deformation cycles in quartz-rich shear zones (Olkiluoto, Finland). Poster presentation, Joint Metamorphic Studies Group and Tectonic Studies Group AGM, University of Plymouth, UK (2018).

Prando, F., Menegon, L., Anderson, M., Viola, G., Mattila, J. Stress history and ductile-brittle deformation cycles in quartz-rich shear zones (Olkiluoto Finland). Oral presentation at the Earth Sciences Research Conference in Plymouth, UK (2017).

Prando, F., Menegon, L., Anderson, M., Viola, G., Mattila, J. Transient stresses and cyclical ductile-brittle-ductile deformation in quartz-rich shear zones (Olkiluoto, Finland). 4th EGU Summer School, Italy (2017)

Word count of main body of thesis: 29091

Signed 

Date 31/01/2024

ABSTRACT

Brittle-viscous deformation cycles at the base of the seismogenic zone in the continental crust

Francesca Prando

The main goal of the study was to determine the dynamical cycle of ductile-brittle deformation and to characterise the fluid pathways at different scale of a brittle-viscous fault zone active at the base of the seismogenic crust. Object of analysis are samples from the sinistral strike-slip fault zone BFZ045 from Olkiluoto (SW Finland), located in the site of a deep geological repository for nuclear waste.

Combined microstructural analysis, electron backscatter diffraction (EBSD), and mineral chemistry were applied to reconstruct the variations in pressure, temperature, fluid pressure and differential stress that mediated deformation and strain localization along BFZ045 across the BDTZ. Ductile deformation took place at 400-500° C and 3-4 kbar, and recrystallized grain size piezometry for quartz document a progressive increase in differential stress during mylonitization, from ca. 50 MPa to ca. 120 MPa. The increase in differential stress was localised towards the shear zone centre, which was eventually overprinted by brittle deformation in a narrowing shear zone. Cataclastic deformation occurred under lower T conditions down to T ≥ 320° C and was not further overprinted by mylonitic creep. Porosity estimates were obtained thought the combination of x-ray micro-computed tomography (μCT), mercury intrusion porosimetry, He pycnometry and microstructural analysis. Low porosity values (0.8-4.4%) for different rock type, 2-20 μm pore size, representative of pore connectivity, and microstructural observation suggest a relationship to dynamical cycle of fracturing and sealing mechanism, mostly controlled from ductile deformation. Similarly, the observation from fracture orientation analysis indicates that the mylonitic precursor of

BFZ045 played an important role in the localization of the brittle deformation. This thesis highlights the ductile-brittle deformation cycle in BFZ045 was controlled by transient oscillations in fluid pressure in a narrowing shear zone deforming at progressively higher differential stress during cooling.

“Coming back to where you started is not the same as never leaving.”

— Terry Pratchett, A Hat Full of Sky

Table of Contents

List of Figures

List of Tables

1 Introduction

1.1 Thesis rationale

According to strength envelopes of the continental crust the Brittle Ductile transition zones (BDTZ) occurs at a depth of 10-15 km in the continental crust (Kohlstedt et al., 1995, Ranalli, 1997, Bos and Spiers, 2002). Such zone corresponds conventionally to the base of the seismogenic zone (Sibson, 1982). Yet, an increasing number of studies indicate that the depth interval for the BDTZ may fluctuate transiently, reflecting variations in strength (Hirth and Tullis, 1994; Scholz, 1998; Fossen and Cavalcante, 2017; Melosh et al., 2018) and fluid pressure (Cox, 2010; Kjøll et al, 2015; Sibson and Rowland, 2003; Yardley and Baumgartner, 2007; Marchesini et al., 2019), thus controlling rheological behaviour of the crust both in the short- and long- term.

The cyclical interplay between brittle and ductile deformation has been documented being an important part of the evolution of some mid-crustal shear zones (e.g. Pennacchioni and Mancktelow, 2007; Fusseis and Handy, 2008; Wehrens et al., 2016; Melosh et al., 2018). However there are still uncertainties about the interplay between the several mechanisms underlying such cyclicity.

A critical question is whether what evidence of such cyclical fluctuations can be preserved in the geological record and if the scale of such variations may be determined by examining natural fault rocks.

The case of study presented in this thesis is a fault zone located in the migmatitic Proterozoic crystalline basement of southwest Finland on the Island of Olkiluoto and characterized by a ductile precursor. The fault is located within the location designated

to host the Finnish deep repository of high-grade nuclear waste. To produce reliable evaluation of the site's long-term stability and the corresponding risk assessment extensive research has been conducted around Olkiluoto's bedrock, and provide an incommensurable resource for the wide array of data offered.

The further refinement of knowledge about the process that characterized faults present in the basement block being excavated in Olkiluoto, brought the support of Posiva Oy, the Finnish organisation responsible for the management of the nuclear waste and the construction of the national repository (http://www.posiva.fi/en) to the research activities of this Ph.D. thesis.

This thesis is part of a larger study in regards of a defined set of conjugate subvertical structures, exhumed from the brittle-ductile transition zone (BDTZ), aimed to be used as a proxy to study fault initiation and reactivation in a crystalline basement in response to fluid pressure oscillations. This study was conducted in collaboration with the University of Bologna, (IT) where a second Ph.D. project was completed in 2020, focusing mostly on the syntectonic veins in the fault zones of the Proterozoic basement.

The main goal of this thesis study was to determine the mechanical evolution, and to characterise the multi-scale fluid pathways of brittle-viscous fault zone active at the base of the seismogenic crust.

Given the presence of a ductile precursor in fault architecture, the research focused on the role played by this ductile precursor in controlling deformation cycles at seismogenic depth.

In this thesis a multi-methodological approach was applied to pursue the set objectives.

Firstly the observation and identification of a record of transient behaviour of deformation by describing the geometry and characteristic microstructure of the fault

trough microstructural studies. Afterwards the work of study was conducted with the objective to estimate the role of different rheological parameters, most notably differential stress, P-T conditions, and fluid pressure, on the activation of brittle vs viscous deformation processes leading to the observed cyclicity. Moreover the characterization of porosity and fractures distribution along the faults was aimed toward the improvement of a proposed conceptual model of the evolution of fault slip behaviour in a cyclical brittle-ductile transition zone.

1.2 Thesis structure:

The approach to the studies presented in this thesis followed a progressive investigation of these subjects, allowing for the generation of (semi-)quantitative restrictions on the deformation mechanisms following the initial microstructural analysis using a multimethodological approach.

Chapter 2: introduces the basic concepts of rock mechanics and fault rheology in the lithosphere that form the necessary conceptual basis to the following chapters. Moreover it provides an overview of the regional geology of southwestern Finland, with a particular focus on the local geology of the Olkiluoto Island. A concise description of the long-term evolution of its basement and of the deformation stages registered is presented.

Chapter 3: gives an overview of the set of analytical techniques and methodologies employed in the study of the Olkiluoto fault rocks. Analysis setting for each technique are given in the chapter in which they have been applied.

Chapter 4: description and characterization of microstructures of the fault BFZ045 with a focus on the brittle fault zone (BFZ) presenting a ductile precursor that forms the main focus of the study. It present the constrained deformation history of the fault zone and

use quartz microstructure to estimate the stress history of the mylonitic precursor. A conceptual model of the evolution of fault slip behaviour is also presented.

This Chapter is based on the published paper :

Prando, F., Menegon, L., Anderson, M., Marchesini, B., Mattila, J., Viola, G., 2020. Fluid-mediated, brittle–ductile deformation at seismogenic depth – Part 2: Stress history and fluid pressure variations in a shear zone in a nuclear waste repository (Olkiluoto Island, Finland). Solid Earth 11, 489–511. https://doi.org/10.5194/se-11-489-2020

Chapter 5: is focused on a detailed multiscale porosity study of the fault rock type characterizing BFZ045. The methods used includes microstructural analysis, μ-CT, pycnometry, porosimetry used to assess the residual porosity of the fault rock and asses possible cyclicity or deformation mechanism controlling variation of fluid pressure.

In Chapter 6: Orientation of fluid pathways are investigated trough image analysis of 3D microtomography dataset of fault rock samples. Using the chlorites lining fractures as proxy to interpret into more the role of the ductile precursor in affecting the brittle onset of the fault deformation.

Chapter 7: final remarks of the presented study and future works

2 The Brittle-Ductile Transition in the continental crust

2.1 Crustal rheology and deformation mechanisms

The deformation behaviour of the continental crust is traditionally described by strength profiles (Kohlstedt et al., 1995). The conventional strength profile of the continental crust is a combination of the increase in frictional strength of the upper crust (which therefore is expected to deform in a dominant brittle way) with depth, and the viscous strength of the ductile middle- and lower crust, commonly described by the rheology of quartz deforming by dislocation creep. The brittle-ductile transition separates the two end-member deformation behaviours and is associated with the change from fracture and frictional sliding on one or more discrete surfaces to thermally activated creep within zones of viscous, solid-state flow (Handy et al., 2007).

The brittle upper crust is characterized by low temperatures and confining pressures; its frictional behaviour is defined by the pressure-dependent Byerlee's law (Byerlee, 1978; Kohlstedt et al., 1995; Ranalli, 1997), also described by the Mohr-Coulomb failure criteria.

$$\tau = \sigma \tan \phi + \mathrm{c} \qquad Equation\ (2.1)$$

Where τ is the shear strength, σ is the normal stress, c is the cohesion, and ϕ is the angle of internal friction.

The increase in the temperature and confining pressure in the middle crust results in the transition towards a ductile deformation style, described by a temperature and strain rate -dependent viscous flow. The deformation mechanisms in the ductile domain are described by flow laws that relate the stress to the strain rate:

$$\dot{\varepsilon} = A\ (\sigma)^n\ \exp\left(-\frac{Q}{RT}\right) \qquad Equation(2.2)$$

where έ is strain rate, σ is the differential stress raised to the stress exponent n, A is a constant (derived experimentally), Q is the activation energy, R is the gas constant, T is temperature.

The two dominant deformation mechanisms that are commonly operative in the ductile regime are: stress sensitive dislocation creep and grain size sensitive diffusion creep. Dislocation creep produces crystal plastic deformation trough motion of dislocation in a crystal lattice. Dislocations move through the crystal lattice along slip systems, defined by specific crystallographic planes and directions. The activation of a slip system depends on multiple factors, such as crystallography, temperature, orientation of the stress field relative to a slip plane, the magnitude of the shear stress, the activation energy, the amount of deformation (strain), and the strain rate (e.g. Stipp et al., 2002; Heilbronner and Tullis, 2006; Karato, 2008). Evidence of dislocation creep in the microstructural record is a strong crystallographic preferred orientation (CPO), flattened and elongate ribbon grains, development of subgrains, and dynamic recrystallization. Dynamic recrystallization is a recovery mechanism that forms new grains by bulging (BLG), subgrain rotation (SGR) or grain boundary migration (GBM) (e.g. Hirth and Tullis, 1992). BLG forms ‘bulges’ in the grain boundaries as effect of intragranular dislocation density differences between adjacent grains. Bulges might form new grains if rotated, pinched or sheared off (Stipp and Kunze, 2008).

With SGR new grains are formed from the progressive rotation of subgrains. Rotation occurs until the misorientation angle between two subgrains reach a determined threshold, usually defined at 10°. The resulting grains are smaller, strain-free grains, with a different orientations with respect to the parent grain. GBM forms new grains by fast migration of a grain boundary from a grain with lower dislocation density into a grain with greater dislocation density (Blenkinsop, 2007; Karato, 2008).

Diffusion creep produces crystal plastic deformation trough the diffusion of intracrystalline point defects along grain boundaries (Coble creep) or within the grain lattice (Nabarro-Herring creep)(Karato, 2008). Nabarro-Herring creep occurs under high temperature conditions, and is rare in crustal rocks, whilst Coble creep is a common process. Diffusion creep is characteristic of high strain rates and low differential stresses and is a grain size sensitive mechanism. Thus, it is facilitated by small grain sizes. Diffusion creep can be identified microstructurally by the fine grain size of polyphase mixtures, a high degree of phase mixing, the high frequency of triple and quadruple junctions between grains, the presence of internally strain free grains, and the absence of a crystallographic preferred orientation (Blenkinsop, 2007).

2.2 The Brittle-Ductile Transition.

The brittle-ductile transition in the continental crust (BDT) is commonly associated with a depth of 10-15 Km, corresponding to the base of the seismogenic zone (Sibson, 1982). However, a growing number of evidence of seismic behaviour below the BDT in the "ductile" crust (e.g. Menegon et al., 2017; Stewart and Miranda 2017; Prieto et al., 2017) indicates that the BDT can propagate to deeper crustal conditions.
Numerous parameters determine the behaviour of faults at the BDT zone in the crust: tectonic settings, fluid pressures, strain rate, bulk-rock composition, and the geotherm (Handy 2007). Of particular interest for this project are the roles of bulk-rock composition (and its associated rheology) and of fluid pressure.

2.2.1 Role of bulk rheology

Depending on the bulk rock composition and mineralogy, the BDT can occur at different depths resulting in "Christmas Tree" type strength profiles (e.g. Kohlstedt et al., 1995, Fig. 2.1). The strength profiles are commonly derived for single mineral phases, which are considered representative of the bulk rheological behaviour of specific crustal depths (e.g. quartz for the middle crust, plagioclase and pyroxene for the lower crust). The average bulk composition at mid crustal level is represented by granitoids, therefore the rheological proprieties of quartz and feldspar are commonly used to model the deformation behaviour of the middle crust at the BDT zone (Hirth et al 2001; Handy and Brun, 2004).

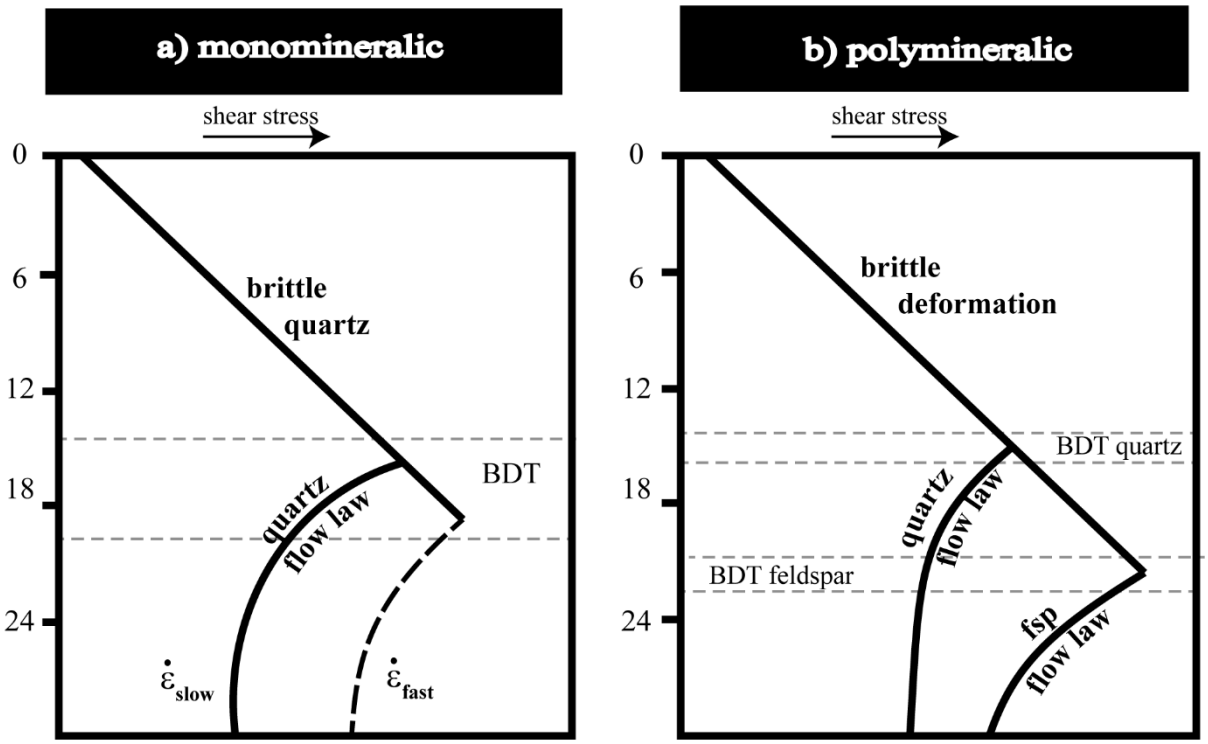

Figure 2.1 Crustal strength profiles for monomineralic (quartz) and polymineralic (quartz and feldspar) rocks (modified from Wehrens et al. 2016).

The rheological behaviour of quartz is generally used to describe the rheology of the middle crust, which typically includes also the BDT (Fig. 2.1). The transition from brittle to plastic deformation of quartz, associated with the onset of dynamic recrystallization processes, has been observed to occur at T of 280° ± 30° (Stipp et al. 2002a).

Observation of natural (Dunlap 1997, Stipp et al., 2002) and experimental (Hirth and Tullis 1992) deformed quartz identified that dislocation creep dominates plastic deformation for quartzite. Hirth et al. (2001) derived the following flow law for dislocation creep of quartzite, which is now commonly used to predict the deformation of quartz under mid crustal conditions:

$$\dot{\varepsilon} = A f_{H2O}^{m} \sigma^{n} \exp\left(\frac{-Q}{RT}\right) \qquad Equation\ (2.3)$$

With n=4, m=1, log (A) =-11.2±0.6 MPa $^{-n}$/s, f_{H2O} is the fugacity of water, Q=135±15 kJ/mol, R is the gas constant, T is temperature.

Assuming a fixed temperature for BDT, (e.g. ~300 for quartz, corresponding to lower greenschist facies metamorphic conditions), the flow law indicates that the depth at which the onset of quartz plasticity occurs can be controlled by variations in stress, strain rate, or fluid pressure.

Considering polymineralic rocks is fundamental to predict a more realistic deformation behaviour of the crust. It is especially true in transient stages involving considerable grain size variations, with potential switches from dislocation creep to diffusion creep triggered by metamorphic reactions and grain boundaries pinning effects (Herwegh et al., 2011), whereas in monomineralic rocks, the effect of secondary phases on the grain size is negligible (Herwegh and Berger 2004). In polyphase rocks, the resulting rock strength will strongly depend on the spatial distribution and amount of different phases, on their relative strength, and on the deformation mechanisms dominant in each phase (e.g. Kilian et al., 2011).

However, in this project we will use quartz microstructures as a proxy for the bulk mechanical and rheological behaviour of the fault. Quartz occurs in large amounts (> 60%) in the fault rock photolith, a veined gneiss with SiO2 content exceeding 75% (Kärki and Paulamäki, 2006), and quartz veins represent a large fraction of the studied fault rocks.

2.2.2 Role of fluids pressure

Fluid pressure has an important role in the mechanical behaviour of the crust, as it lowers the normal stress acting on a surface ($\sigma_n^{eff} = \sigma_n - P_f$ for Terzaghi's principle where σ_n^{eff} is the effective normal stress, σ_n is the normal stress and P_f is the fluid pressure), therefore facilitating brittle failure at depths where the rock would otherwise be stable or in the ductile domain. Estimating the pore fluid pressure is crucial to determine the depth and the processes of the BDT, especially in cases where pore fluid pressure has values higher than hydrostatic

(Fig. 2.2).

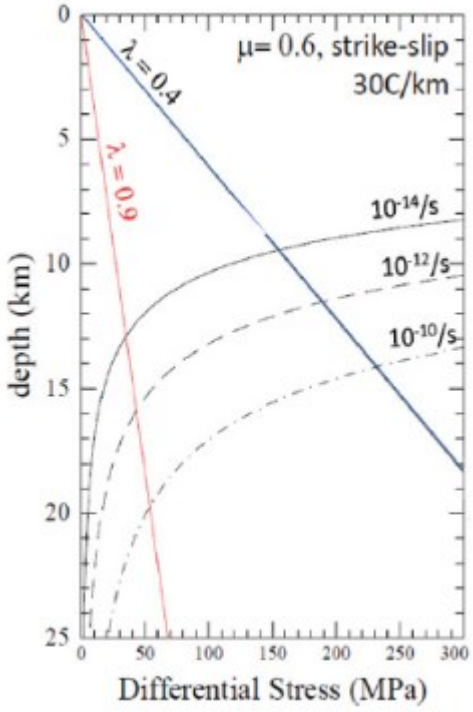

Figure 2.2 Strength profile calculated for a strike slip setting (Hirth and Beeler 2015). Strain rates calculated using quartzite flow law (Hirth et al. 2001). Brittle failure shown for ratio of pore fluid pressure l ranging from 0.4 (hydrostatic pore fluid pressure) to 0.9 (near-lithostatic pore fluid pressure).

Pore fluid pressure is expressed by the pore fluid factor λ, which is the ratio of fluid pressure P_f to vertical stress σ_v. Values of λ=0.4 are characteristic of hydrostatic fluid pressures in the crust, while λ=1 indicate a lithostatic fluid pressure. Evidence for

elevated pore fluid pressure (λ>0.4) affecting fault behaviour has been reported from the granitoid middle crust (Cox, 1995; Cox, 2007; Wehrens et al., 2016; Molli et al. 2017).

Figure 2.2 (from Hirth and Beeler, 2015) shows an example of how pore fluid factor can affect the depth of the BTD and the rheological behaviour of a strike slip fault.

Considering a possible range of differential stresses associated with fault reactivation of normal, strike-slip, and reverse faults at seismogenic depth (40 to 160 MPa, taken from the literature), Streit and Cox (2001) inferred that high pore fluid factors values are needed to have seismic reactivation of cohesive faults near the base of the seismogenic zone at ≈ 15 Km (e. g strike slip $\lambda \approx$ 0.6 to 1).

Fluid flow at the BDT depends on the competition between porosity-generating (e.g. micro cracks, dilatancy) and porosity-destructing (e.g. crack healing and sealing) processes. The competition between these mechanisms may result in transient episodes of high fluid flux associated, for example, with the emplacement of veins in an otherwise ductile environment (Cox 2002). This reflects also the competition between brittle and ductile deformation mechanisms that characterizes shear zones and faults at the BDT. In turn, the transitions in deformation mode (from viscous creep to brittle fracturing) is likely to be related to episodic fluctuation in differential stress, strain rate and fluid pressure (Cox, 1999), leading to episodic fluid flow.

To visualize the transient behaviour of faults related to the evolution of pore fluid pressure and differential stress, Cox et al. (2010) proposed the use of λ-σ failure mode diagrams.

These diagrams illustrate brittle failure envelopes and strain rates contours calculated for faults in different tectonic regimes, depth, cohesive strength, friction coefficient and orientation (as defined by the angle between σ_1 and the fault plane) (Fig. 2.3).

Brittle failure occur either by extension mode fracture or shear failure, while in some cases it may involve a component of shear and dilation, resulting in a hybrid extensional-shear failure. The mode of brittle failure depend on relative values of differential stresses and tensile strength (T). The diagram in Fig.2.3 presents the pore fluid factor-differential stress for a given depth in the crust. The extension mode envelope (in red) extends between $0 \leq \sigma_1-\sigma_3 \leq 4T$; hybrid extensional-shear failure (in green) is modelled as a parabolic failure envelope in the interval $4T \leq \sigma_1-\sigma_3 \leq 4T/\sin\theta$, with θ being the angle between σ_1 and the shear fracture. Brittle shear failure (in blue) occur on a linear failure envelope $\sigma_1-\sigma_3 \geq 4T/\sin\theta$. For all stress and pore fluid factors state occuring below the composite failure envelope, the rock mass can deform plastically or be elastically strained. Brittle failures occurs when stress or pore fluid pressure states reach the envelope. States of stresses or pore fluid factor above the envelope cannot be attained.

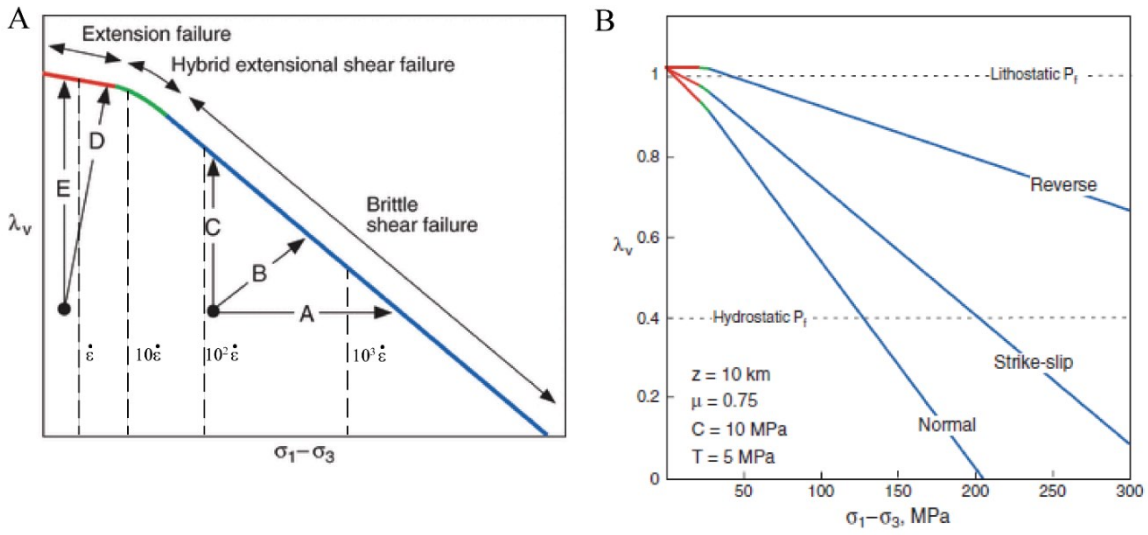

Figure 2.3 Pore fluid pressure (λ) – differential stress (σ) failure mode diagrams. A) Generic failure mode diagram at a given depth. For stresses below the composite failure envelope, the rock mass deform viscously. Strain rate contours based on a cubic power law illustrate viscous creep. Paths A-E illustrate how changes in fluid pressure and stress states can drive failure. B) Failure mode diagram for reverse, normal and strike-slip regimes at depth of 10 km. The composite failure envelop are colour coded as in A (Modified from Cox et al. 2010).

The λ-σ failure mode diagrams provide an ideal tool to model the possible evolution of failure modes as a function of oscillations in pore fluid pressure and differential stress. Brittle failure of a rock can be induced by a combination of changes in pore fluid pressure and differential stress (Sibson 2001). In the example shown in Figure 2.3, Path A represents a purely stress driven failure, while path C and E are purely fluid driven, however due to the variation in differential stresses they result in the development of a shear fracture and of an extensional fracture, respectively. Paths B and D represent cases where brittle failure is triggered by a combination of pore fluid pressure increase and differential stress increase.

2.3 Overview of the geology of southern Finland

The crystalline bedrock of Finland is part of the Precambrian Fennoscandian Shield. North Finland is characterized from the Karelian Craton and Lapland greenstone belt, Archean in age (3.5-2.5 Ga) (Vaasjoki et al., 2005). (Fig 2.4)

A younger Paleoproterozoic basement (1.93-1.8 Ga) characterises central and southern Finland, delineating the Svecofennia tectonic province (Nironen et al. 2017). The province is divided in Western and Southern subprovince, emplaced either during a single Svecofennian orogenic episode (e.g. Lahtinen et al 1994, Nironen et al. 1997, Pajunen et al. 2008) or during several separates orogenies. (e.g. Lahtinen et al 2005, Korja and Heikkinen 2005).

The accretionary event came to conclusion at approx. 1.8 Ga, marked from extensive late syn- and post- orogenic granitoids intrusion. After a 150 Ma phase of orogenic collapse, extensive melting of the lower crust characterised an extensional tectonic regime, leading to the emplacement of Mesoproterozoic Rapakivi granites (1.65-1.54 Ga) in the southern Finland craton. This tectonic phase could be related to the

development of a rift along the present Baltic Sea (Korja et al., 2001). The latest stage of crustal evolution in southern Finland is expressed by the intrusion of 1.27-1.25 Ga, N-S striking olivine diabase dikes (Suominen, 1991).

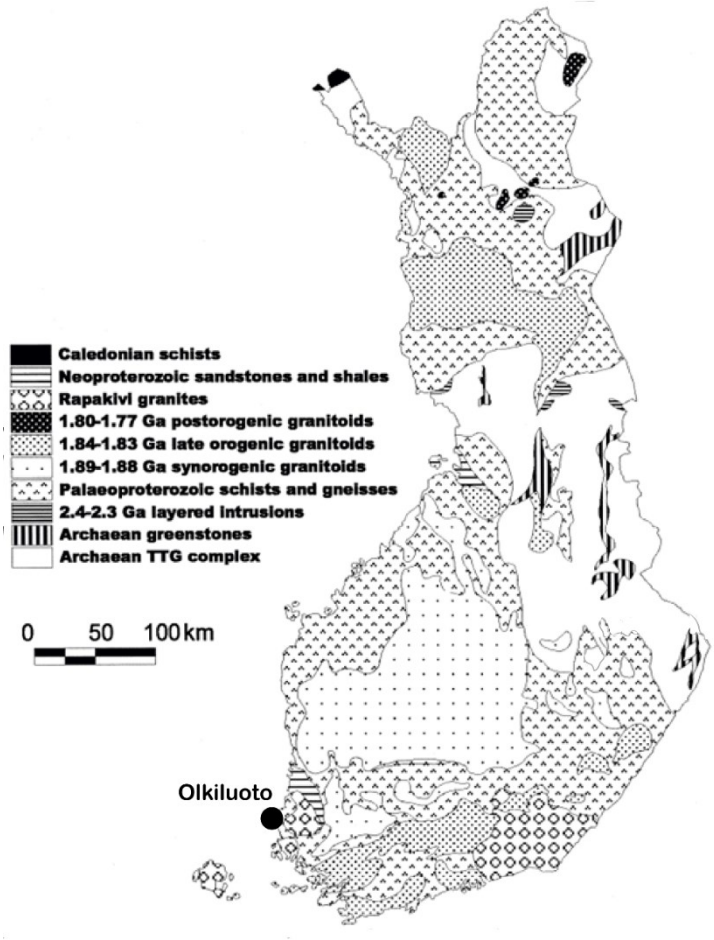

Figure 2.4 Simplified geological map of Finland (Modified from Lehtonen, 2005), showing the location of the studied area (black dot).

2.4 The study area: Olkiluoto, SW Finland

Situated at the western end of the Southern Finland subprovince, Olkiluoto island is part of the Paleoproterozoic Svecofennian orogeny. The bedrock comprises migmatitic metasedimentary rocks, injected by leucocratic granites, granodiorites and tonalities. The migmatites formed at the peak of the regional metamorphism, under upper amphibolite facies condition. The estimated age is between 1.89-1.86 Ga. The peak pressure and temperature conditions were estimated at 3.7-4.2 Kbar and 660-700° C

from the stable mineral assemblages (Tuisku and Karki, 2010). Intra-orogenic magmatism occurred at the same time of metamorphism, dated using U/Pb at 1.89 – 1.85 from intruded granites.

Retrograded greenschist facies metamorphism followed the peak conditions, ceasing with the orogenic collapse at 1.79-1.77 Ga. (Lahtinen et al., 2005). Mesoproterozoic intrusion of Rapakivi granites and diabase in the surrounding of the area took place at 1.5 Ga.(Vaasjoki et al., 2005). Crustal extension formed a NW-SE trending graben 50 Km north of Olkiluoto, filled with Jotnian sandstones.

The main lithological units in Olkiluoto are two different migmatites, a veined gneiss unit and a diatexite, intruded by small lenses of mica-bearing gneiss and granitic pegmatoids and diabase dykes.(Fig2.5) Diatexites outcrop in the eastern and south-eastern part of the island, and are characterized by high grade migmatites, containing a granitic leucosome forming up to 85% of the rock volume. The western part of Olkiluoto is characterised by the veined gneiss unit and by metatexitic migmatites with 20-40% of leucosome.

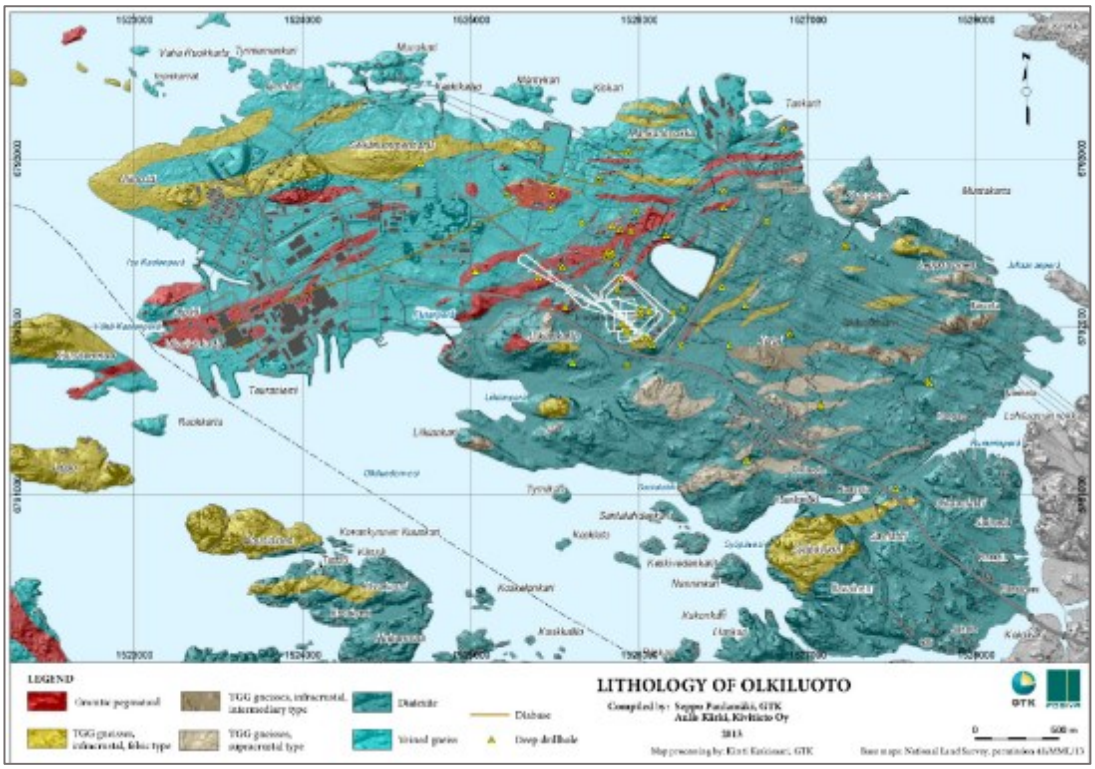

Figure 2.5 Simplified geological map of Olkiluoto (in blue migmatitic units, in red, yellow and brown lenses of granitoids and gneisses.) The white line show the extension of the Onkalo facility (Aaltonen et al., 2016)

A polyphase ductile deformation has been observed in Olkiluoto (Aaltonen et al. 2010). The earliest observed structural element of the area is the biotite foliation S1 of deformation phase D1, retained in restite blocks (20-50 cm in diameter) surrounded by high-grade migmatites, formed during the metamorphic peak.

The second phase (D2) was active at the peak of the metamorphism that caused intense migmatisation. It is characterized by a pervasive S2 foliation visible as a metamorphic banding, and its age is estimated to be close to 1.86 Ga (U-Pb age 1863±3Ma of a granitic gneiss deformed during D2). D3 phase was active between 1.86- 1.82 Ga (pegmatitic granite dated with U-Pb). It took place under amphibolite-facies conditions and formed NE-SW striking pervasive foliation (S3) and shear zones. At 1.81 Ga (Monazite age 1808±6 Ma)

D4 phase produced NNE-SSW and N-S striking shear zones, characterised by mylonitic foliation (S4). Retrograde metamorphism to green schist facies condition affected the

rocks soon after the metamorphic peak, lasting until 1.79-.172 Ga, the estimate cooling ages based on Ar^{40}/Ar^{39} analysis of biotite, muscovite and hornblend (Aaltoonen et al. 2016).

The onset of the brittle deformation in Olkiluoto can then be placed at approx. 1.75 Ga, based on biotite Ar $^{40}/Ar^{39}$cooling ages (Aaltoonen et al. 2016). Seven distinct brittle stage has been recognized through paleo stress inversion analysis of fault slip data (Fig.2.6, Mattila and Viola, 2014). The stages of brittle deformation are characterized by both the reactivation of optimally oriented pre-existing ductile structures, and nucleation of new structure (Nordbäck et al., 2022).

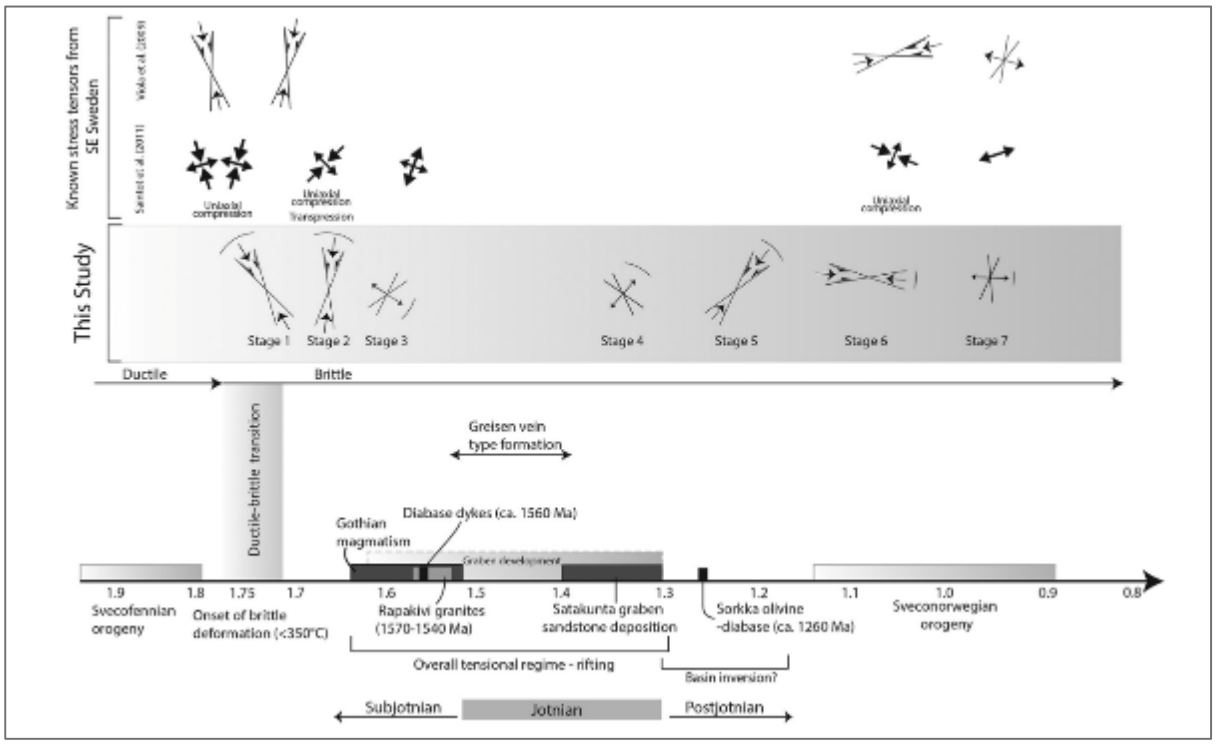

Figure 2.6 Overview of the brittle deformation history of Olkiluoto. (Modified from Mattila and Viola, 2014)

The earliest brittle structures are related to a compressional event, oriented NW-SE to NNW-SSE, occurring after the Svecofennian orogeny, ca. 1.79-1.75 (Torvela et Ehlers, 2010). Structures related to this event are both brittle reactivation of NE-SW striking ductile shear zone and N-S striking strike-slip faults at the brittle-ductile transition..

Nucleation of N-S faults zones has been interpreted to be the result of strain localisation during late stage of ductile deformation D4, linked to an anastomosing network of high-grade shear zones (Skyttä and Torvela, 2018).Shortly after an NNE-SSW oriented compression episode affected Southwest Finland. It was characterised by dextral reactivation of originally sinistral strike slip striking N-S and the development of new NE-SW trending structures.

Trastensional stresses related to tectonic events during the Gothian orogeny, ~1.6 Ga ago (Stage 3, fig 2.6), have been associated to the formation of E-W striking oblique dextral/normal faults.

The following deformation events were active in tensional regime, during a regional episode of rifting and the emplacement of Rapakivi granite in the Mesoproterozoic (1.65-1.50 Ga). In Olkiluoto the structure representing those tensional regimes are NE-SW striking diabase dykes (1.56 Ga) and greisen veins crosscutting the diabase dykes (1.56-1.38 Ga, Mänttäri et al, 2007), that occur as subvertical, NNW-SSE or N-DS striking veins in the migmatites. At approximately 1.3–1.2 Ga, NE-SW compression led to the reactivation of pre-existing fault networks, coeval with the intrusion of olivine diabase sills. At the beginning of the Sveconorwegian orogeny, approximately 1.1–1.0 Ga ago, low-angle thrust faults formed and some of the pre-existing fault systems were reactivated in response to E-W compression (Stage 6, fig. 2.6). The collapsing phase of the Sveconorvegian orogeny, ~ 0.97–0.87 Ga ago, was characterised from E-W extension that reactivated parts of the pre-existing fault systems (Stage 7, fig. 2.6). Later reactivations of faults in Olkiluoto have been linked to NW-SE to E-W crustal shortening at the first stages of the Caledonian Orogeny (Viola et al. 2011; Elminen et al., 2018;Tillberg et al., 2021) Of major interest for the project is the onset of the brittle deformation that followed the last ductile deformation stages (D4), associate with the

first compressional stages of brittle deformation (1.79-1.70 Ga) active during the cooling of the crust.

2.5 Fault complex of Olkiluoto

Faults in Olkiluoto have been grouped in four different fault system named Fault system I to IV (Nordbäck et al., 2022). Fault system I present N-S to NNE–SSW trending sinistral strike-slip faults, and Fault system II is composed of sub-vertical, NNW-SSE striking and steeply dipping dextral strike-slip faults. Given the long deformation history that has interested Olkiluoto the age of initial nucleation and localisation of the first fault system has been difficult, and is still object of study (Nordbäck et al., 2022). Formation of Fault system I and II has been described to have occurred in response to the onset of brittle deformation in Olkiluoto, that occurred in response of tectonic events in the late phases of the Svecofennian orogeny (~1.79-1.75 Ga) and have been related to the first two stages of brittle deformation described in Mattila and Viola (2014) (fig.2.6). Topological relationship between the two fault systems and the presence of mylonitic precursors only observed for Fault system I (Aaltonen et al., 2016), indicates that Fault system I formed under more ductile conditions than Fault system II. Nordbäck et al. (2022) suggest that formation of the oldest fault system might have caused changes in the local stress field, and acted as “master” faults controlling the formation of antithetic Fault system II, in accordance with the criteria for distributed strike-slip shear zones (Schreurs et al.,2003).

Fault system III is characterised from E-W striking, sub-vertical to moderately south dipping dextral fault zones, that develop along E-W trending and moderately south dipping dextral shear zones, formed ca. 1.86–1.82 Ga ago, during D3 (Mänttäri et al., 2006). Crosscutting relationships between the first two fault systems and Fault system III, coupled with observed differences in orientation and kinematics, indicate that Fault system III formed in response to a later tectonic event. Fault system IV contains SE

dipping low-angle fault zones, whose structures exploit the lithological contacts between porphyritic granite rocks and migmatitic foliation planes. K-Ar radiometric ages of samples from Fault system IV suggest nucleation ~ 1.04–1.0 Ga (Viola et al., 2011; Nordbäck et al.,2022).

Between 1.3 Ga and 0.55 Ga multiple events of structural reactivation of pre-existing fault systems have been differentiate from illite K-Ar ages of fault gouges (Mänttäri et al., 2007; Viola et al., 2011).

2.6 Structural characteristic of fault system at the ONKALO facilities

ONKALO the underground rock characterisation facility is located in the central part of Olkiluoto (Fig. 2.7a). It consists of one access tunnel, extending to a depth of ~450 meters and three shafts: a personnel shaft and two ventilation shafts.

At the end of the ONKALO tunnel, a number of pilot holes were drilled at pre-determined locations, with the purpose to characterise the hydrogeological properties of the rocks previous to the excavation of the actual repository (Fig.2.7c).

A network of vertical N–S and NW–SE faults, belonging to Fault system I and II, has been mapped and investigated at the repository scale in ONKALO with underground surveys and boreholes (Aaltonen et al., 2016, Fig. 2.7 a, b). Intersecting the repository site are a set of conjugate strike slip fault zones, named BFZ045 and BFZ300, that have been select has representative fault for Fault system I and II respectively (Fig. 2.7 b). BFZ045 is a N-S trending sinistral fault and BFZ300 is a NW-SE dextral fault (Fig. 2.7 c). Modelled fault surfaces are shown inf Fig. 2.7d, with orientation of 095°/87° dip direction/dip angle for BFZ045 and 250°/80° for BFZ300.

BFZ045 exploits a mica-rich mylonitic precursor, whereas BFZ300 cut across discordantly the metamorphic foliation and does not shows any correlation with older ductile fabrics (Aaltonen et al., 2016)

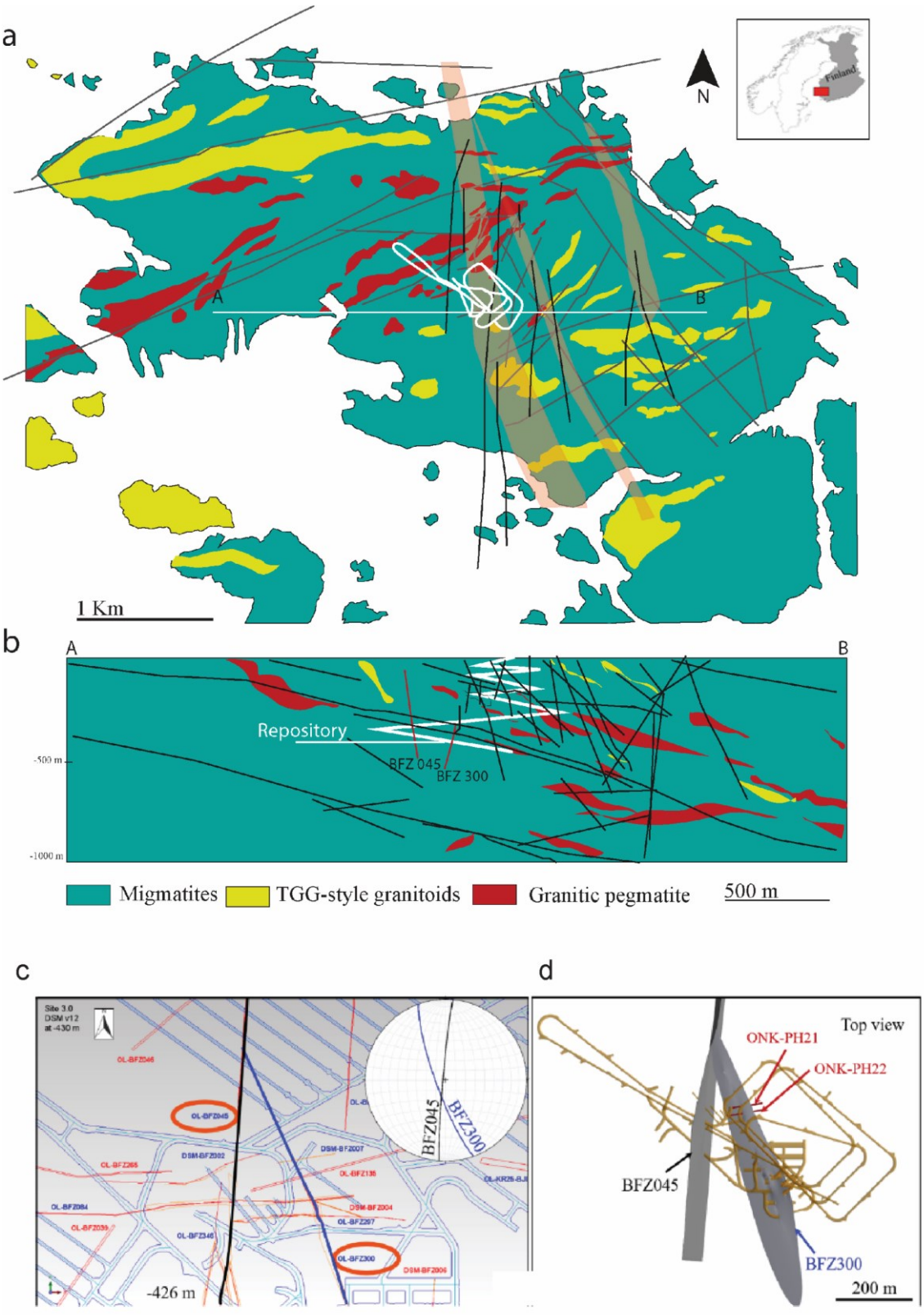

Figure 2.7 Schematic geological and structural map and site scale view of the studied system of faults. a) Geological setting of Olkiluoto, SW Finland (top-right inset). Geological map showing surface intersection of modelled brittle fault zone (BFZ) and ductile deformation zone, modified from Aaltonen et al. (2016) and Skyttä and Torvela (2018). Coordinates are for zone 34N in UTM coordinate system. The white line indicates the location of the underground ONKALO facility. A–B is the trace of the cross section shown in (b). b) East–west cross section for the underground

infrastructure, with the tunnel traces shown as white lines. Sub-vertical fault BFZ045 described in this study and its conjugate BFZ300 are shown as orange lines. c) Plan view of the facility layout and intersection of BFZ045 and BFZ300 fault segment at 426 m b.s.l. Lower-hemispere projection stereonet of modelled fault orientation. d) Northwest view of modelled set of faults in study. Underground infrastructures are marked in yellow. Photo courtesy of Posiva Oy, Finland.

This study uses the N–S sinistral strike-slip fault BFZ045 as a natural laboratory to investigate the stress history of the ductile precursor and the possible role of fluids on the deformation processes active at the brittle–ductile transition. The companion PhD project, conducted at the University of Bologna, by Marchesini et al. (2019) has thoroughly described the deformation history of the conjugate dextral BFZ300 fault.

3 Methods

This chapter aims to offer an overview of the analytical techniques applied throughout the PhD, and to familiarize the reader with terminology used in the thesis. The following sources are suggested to the reader for detailed information and comprehensive explanation of each techniques: Goldstein et al., (2017) and Reed (2005) for information regarding scanning electron microscopy and electron microprobe, Smith and Dent (2005) for an overview of Raman spectroscopy, Ketcham and Carlson (2001) and Withers et al. (2021) for a review of X-ray computed tomography, Anovitz and Cole (2015), Giesche (2006) and Webb(2001) for methods regarding porosity measurements.

Thin sections were observed under polarised light microscopy for general microstructural characterisation, and to select areas of interest for analysis such as scanning electron microscopy, electron microprobe analysis and Raman spectroscopy. Care was taken to select complementary methodologies to characterise several samples with multiple analytical methods, making possible to correlate different information, e.g., 3D orientation, porosity, microstructural and chemical data.

3.1 Scanning Electron Microscope (SEM)

Scanning Electron Microscopy (SEM) is commonly used in structural geology for its versatility, since it can be used to obtain microstructure images, compositional data, and crystallographic orientation data (Goldstein et al., 2017, Reed 2005). In this thesis, SEM was used to obtain high-resolution backscatter electron images (BSE) of deformation microstructures and pores, to identify mineral phases and their distribution using energy dispersive spectroscopy (EDS), to assess the presence of healed cracks and growth

features in quartz trough cathodoluminescence (CL), and to acquire quantitative microstructural and crystallographic orientation data for quartz using Electron Backscatter Diffraction (EBSD).

Scanning electron microscopy is based on the interactions between an accelerated high-energy electrons beam and a small volume of matter. This results in the emission of different signals, which include electron scattering (e.g., secondary electron SE and backscatter electrons BSE), and electromagnetic signals (e.g. photons and X-rays) (Fig 3.1).

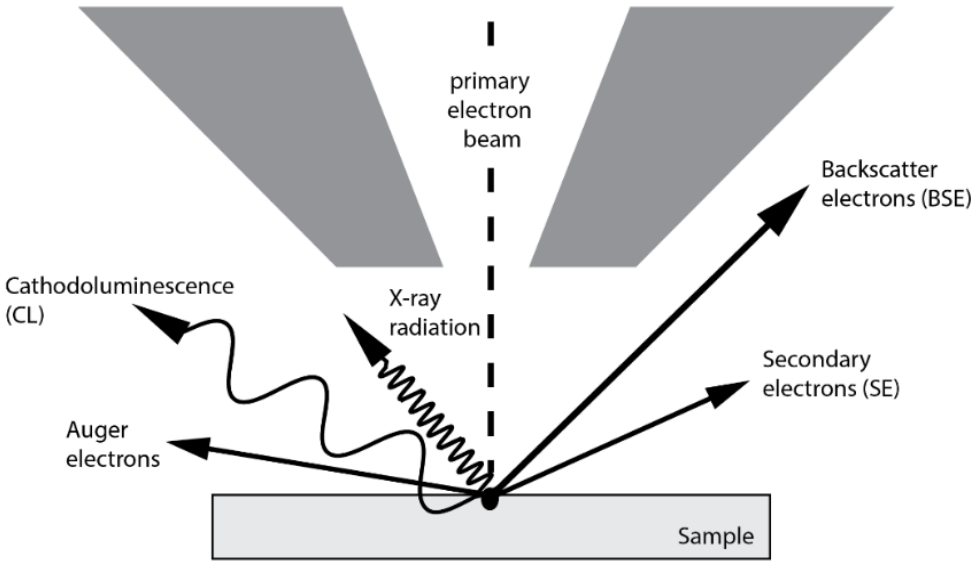

Figure 3.1 Schematic representation of beam-sample interactions and produced signals(modified from Reed 2005).

Electrons scattered as a result of the interaction between the sample's atoms and the electron beam are partially absorbed by the sample, while others are scattered back out of the sample. Secondary electrons are low energy particles (<50 eV) dislocated by the incident beam in the first few nm^3 of interaction, that are used to obtain morphological images. Backscattered electrons are charged particles belonging to the incident beam that are scattered backward after the interaction. Since their energy depends on the total

number of interactions within the sample, which is controlled by the average atomic number, their use help to discriminate phases based on the mean atomic number. Besides electron scattering, photons of characteristic wavelength can be emitted from a material interacting with a high-energy electron beam. This process is called cathodoluminescence (CL). CL signals can be controlled from defects and crystal damage effects, from impurities, and from compositional variations. This is why CL is commonly applied to obtain information on the presence of specific elements in the minerals, which can affect the CL signal, or to observe mechanically induced defects. The distribution of CL signal in the samples can be used to obtain information on crystal growth structures, replacement, dissolution and provenance (Frelinger et al. 2015). CL signal is detected with a camera (monochromatic or panchromatic), and the intensity differences results in greyscales images.

X-rays emitted from the beam-sample interaction represent the most energetic interaction that causes the electrons to gain energy and move from an orbital to another. The subsequent transition to the previous energy state triggers an emission of X-ray characteristic of the involved chemical element (known as characteristic spectrum). A semi-quantitative chemical composition of a sample can be obtained from an investigation of the emitted X-ray spectrum. The x-ray energy spectrum is recorded and processed using energy dispersive spectroscopy (EDS) to identify the abundance of the major elements in the sample and their relative concentrations. The spectrum is plotted as x-ray counts vs energy peaks (in keV) corresponding to the various elements in the sample. Due to the high intensity of characteristic spectra and low spectral resolution, EDS can acquire semi-quantitative elemental maps or spot chemical analyses.

3.1.1 Electron Backscatter diffraction (EBSD)

With Electron Backscatter diffraction (EBSD) analysis, the pattern of the BSE are analysed. At the interaction with the sample, the incoming electrons are randomly

diffracted. Electrons are diffracted by lattice planes at angles which satisfy the Bragg's equation:

$$n\lambda = 2dsin\theta \quad (3.1)$$

where n is an integer, λ is the wavelength of the electrons, d is the spacing of the diffracting plane, and θ the angle of incidence of the electron on the diffracting plane. The diffracted electrons will form diffraction cones, that correspond to each diffracting lattice plane, and can be detected when they impact an EBSD detector (phosphor screen that convert the electron to light) (Fig 3.2 a). Kikuchi bands, or "EBSP's" (electron backscatter patterns) (Fig 3.2 b), generated from the intersection of the diffraction cone with the detector are recorded by a CCD (carged couple device) camera. Kikuchi bands are projections of the geometry of the lattice planes in the crystal, and they give direct information about the crystalline structure and crystallographic orientation of the grain from which they originate. The EBSD software uses angles and position of the Kikuchi bands to recognize patterns and compares them with theoretical match units of specific mineral phases derived from their lattice parameters. The process of attributing a specific crystallographic orientation to a mineral phase is referred to as "indexing" (Fig3.2b). Noise in the EBSD pattern is subtracted using a background pattern collected before the indexing procedure. The quality of the indexing can be checked using different parameters, which are mostly depended on the software used. In this thesis indexing accuracy is expressed using the Mean Angular Deviation (MAD). MAD indicates the angle of deviation of the indexed pattern from the theoretical match unit, and a good indexing present MAD values <1°. EBSD patterns are measured in raster mode using a step size defined by the user. The obtained patterns can be visualized as crystallographic orientation maps, where each pixel represents an orientation of the crystals lattice. EBSD maps can also be used to display other quantitative information such as grain size, misorientation angles of all pixels from one specific orientation,

misorientation angles between two pixels or between set of pixels (within grains or at grain boundaries, Prior et al., 2009; Fig 3.2 c-g)). Additionally, EBSD data can be presented with pole figures (PF), which are stereographic projections showing the orientation of specific crystallographic planes and directions of the analysed phase with respect to an external reference frame (Fig 3.2e). Inverse pole figure maps (IPF) are colour-coded to visualise how a specific direction (e.g. one of the axes of the SEM chamber) is oriented with respect to the crystal lattice of the investigated phase (Fig 3.2d). The symmetry of the crystal and the known slip systems guide the choice of crystallographic planes and directions to plot. The specimen reference frame of the samples (axes X, Y, Z) investigated here can be defined from the user, and in this thesis X parallel is to the stretching lineation, Z to the pole to the mylonitic foliation, and Y is perpendicular to the XZ plane.

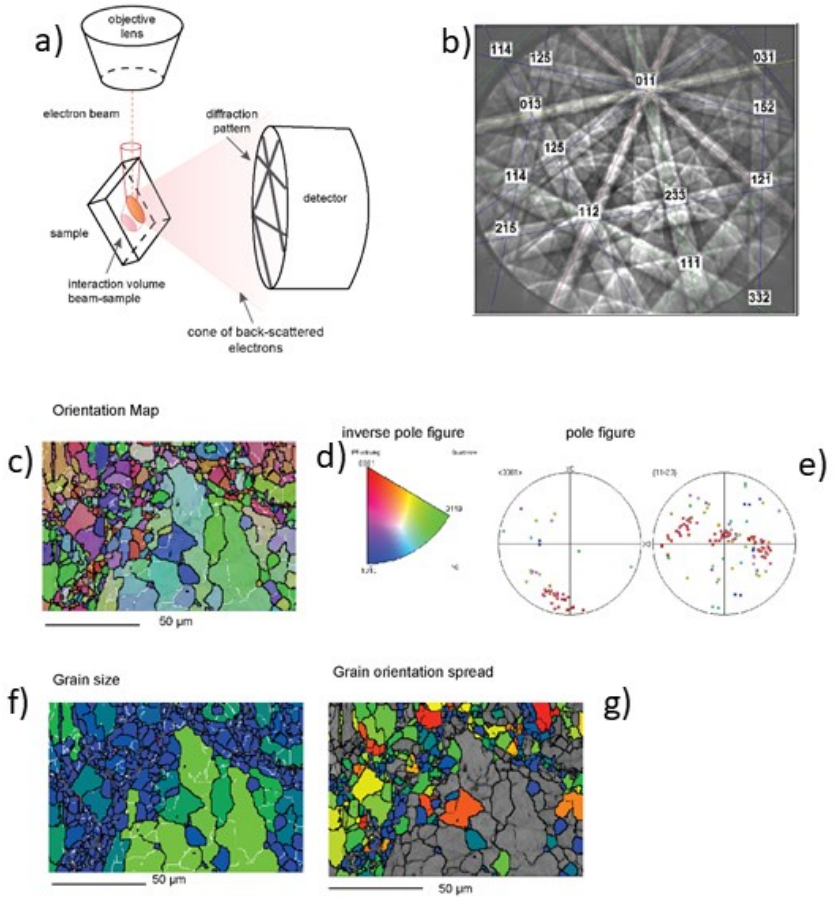

Figure 3.2 Drawing illustrating geometry of EBSD analysis and possible results of the analysis. a) Set up of sample tilted at 70° to the horizontal position. The cone of diffracted electron at the contact with the detector produces a pattern of lines (Kikuchi bands). B) example of EBSD pattern for quartz.

3.2 Electron Microprobe (EMP)

Quantitative mineral chemistry was obtained using Electron Microprobe (EMP) analysis. The electron microprobe, like the SEM, is based on the interaction between a focused electron beam and the sample. Differently than the SEM, EMP are equipped with multiple Wavelength Dispersive Spectroscopy (WDS) detectors, which measure the wavelength of X-rays emitted during the beam-sample interaction. Characteristic x-ray wavelength is defined through diffraction and is used in WDS analysis to identify

chemical elements. The sample characteristic spectrum is collimated and conveyed toward an analyser crystal, of known composition, structure and spatial orientation that optically disperses the characteristic spectrum according to the Bragg's law. By comparing the signal's strength to that of standards, element concentrations can be identified. The number of counts per second that the WDS detectors measure is the signal's intensity. The data output is a table showing the weight percent of the simple oxides that constitute each mineral.

Using stoichiometric principles, the compositional data can then be used to calculate the structural formulas of the minerals.

3.3 Raman Spectroscopy

Raman spectroscopic analysis was applied to investigate the grade of amorphization of graphite, which was used to estimate the temperature of deformation. Raman spectroscopy is based on the interaction between an incident monochromatic light (laser) beam and the sample surface (matter). This interaction results in reflected, transmitted, or scattered light beams. The radiation scattered from the material is detected in Raman spectroscopy. The light that hits the molecule causes the electron cloud to become distorted. This is called polarisation of the electron cloud, and it puts the molecule in a higher energy state called the "virtual state." (Smith and Dent, 2005). Since this state is unstable, the photon is almost immediately re emitted as scattered light. The energy of scattered light is dependent on the frequency of the light source used. The majority of the scattered light carries the same energy as the incident light. (i.e., elastic scatter: Mie and Rayleigh scattering) (Fig. 3.3 a). A small portion of the incident beam light is scattered with a different energy with respect to the incident beam (i.e., inelastic behaviour or Raman scattering). Two types of Raman scattering can be

differentiated, the Stokes scattering and the anti-Stokes scattering. In the Stokes scattering process, the molecule from the initial vibrational state (m) is excited to the virtual state and absorbs part of the energy, which after scattering, leads to a promotion of the molecule to a higher energy vibrational state (n) (Fig. 3.3b). Inversely in the anti-Stokes scattering the molecule loses energy by relaxing to a lower vibrational state (n to m in fig 3.3b), thermal energy influences the presence of molecules at an initial excited state. Since the Stokes Raman scatter is always more intense than the anti-Stokes, it is commonly the previous that is presented in Raman spectroscopy (Fig.3.3c).

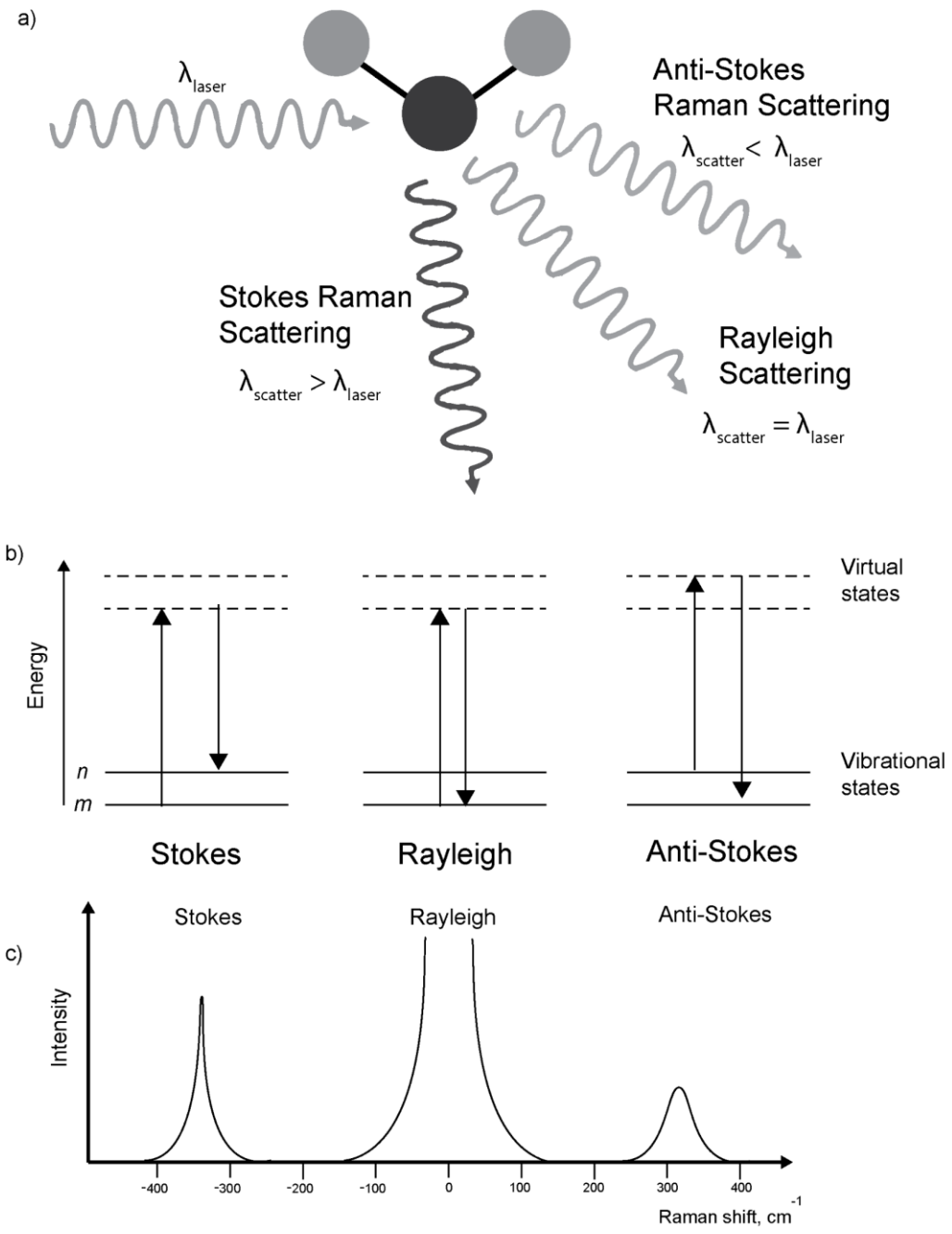

Figure 3.3 Schematic representative of Raman scattering process. a Three types of scattering processes that can occur when light interacts with a molecule. b Energy-level diagrams of Rayleigh scattering, Stokes Raman scattering, and anti-Stokes Raman scattering. Rayleigh scattering is elastic; the incident photon is of the same energy as the scattered photon. Raman scattering is inelastic; in Stokes scattering, the incident photon is of greater energy than the scattered photon, while in anti-Stokes scattering, the incident photon is of lower energy. (modified from Smith and Dent, 2005) c schematic of Raman spectrum.

In order to compare spectra acquired with various lasers, the Raman scatter wavelength is converted to the Raman shift, which is the change in wave number between the incoming and emitted photons. The wave number is the inverse of wavelength, which

represent the number of waves in a length number and is expressed in cm^{-1}. The wavenumber shift is characteristic for a material.

The Raman spectrum plots light intensity (arbitrary units) in the y-axis versus light frequency (relative wavenumbers) in the x-axis expressed as Raman shift (Fig 3.3 c). The Rayleigh line equals a value of 0 Raman shift.

3.4 X-ray Computed Micro Tomography (μCT)

X-ray Computed Micro Tomography is based on the mapping of the interaction of X-rays with the investigated materials. As the X-ray beam passes through the sample, its intensity is decreased as a function of composition and density of the sample. This intensity decrease is described by the Beer–Lambert Law for a monochromatic beam:

$$\mathrm{I} = I_0 \exp\left[-\int_{-\infty}^{\infty} \mu(x)dx\right] \qquad Equation\ (3.2)$$

where I_0 is the intensity of the original incident beam from the X-ray source, I is the attenuated intensity measured at the detector after X-rays have passed through a sample of thickness x, and $\mu(x)$ is the linear attenuation coefficient (Ketcham and Carlson, 2001; Cnudde and Boone, 2013). For multi-phase samples and polychromatic beam the attenuation in the previous equation becomes:

$$\mathrm{I} = I_0 \exp[-\textstyle\sum_i \mu_i x_i] \qquad Equation\ (3.3)$$

in which the path length and attenuation coefficients (μ_i) for all materials in the sample are considered (Ketcham and Carlson, 2001; Wildenschild and Sheppard, 2013; Kyle and Ketcham,2015). The attenuation of an X-ray beam of a given energy depends on the atomic electron density of the imaged material and its bulk density. Dense mineral phases have a high attenuation coefficients compared to less dense minerals, and appear as bright objects in the reconstructed tomographic data.

An X-ray source, a sample stage, and an X-ray detector are the three fundamental components of laboratory CT scanners. The system geometry is the so-called cone beam system, where a rotational sample holder is located between the X-ray source, commonly an X-ray tube, and the X-ray detector (Fig 3.4).

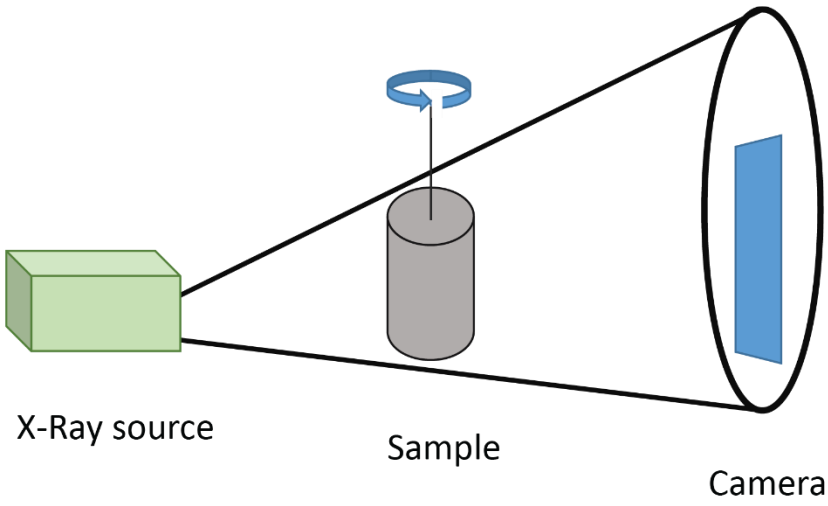

Figure 3.4 X-ray computed tomography configuration. Cone beam system characteristic of laboratory system.

In this the distance between the X-ray source and the sample can be decreased to magnify the image. The X-rays passing through the sample are collected by the detector using a scintillator screen that converts the X-rays into photons in response to the absorption of X-rays (Baker et al., 2012; Wildenschild and Sheppard, 2013, Fusseis et al., 2014). The photons are then counted, recorded and converted into a digital signal for processing by using either charge-coupled devices (CCD) or complementary-

metaloxide-semiconductor (CMOS) sensors. Radiographs of the samples are recorded in evenly spaced angular intervals through a full 360° rotation. Combination of a sufficient number of 2D radiographs slices allows to create a 3D dataset, composed of 3D pixels, called voxels, and mapped in grey values. Commonly μCT images collected during an analysis comprise of projections, which are the radiograph of the sample, of the dark current (or offset) and flat-field (or gain) images. Dark current images collect the environmental signal measured in the absence of X-rays, while flat-field images present the signals of the X-rays beam without a sample present. Flat-field and dark current are used to correct the projections from heterogeneity due to defects of the incident X-ray beam, defects of the detector or scintillator (with or without X-rays respectively). Another correction applied to the projections is to diminish the effect of brightness variations of the X-ray source (known as normalisation process: Gürsoy et al., 2014). After normalization the projections are used to generate sinograms. Considering a row of pixel in the detector, a sinogram is traced as the sample rotates, showing the variation in attenuation values across the row of pixel as the projection angle varies, producing a curve similar to a sinusoid for each pixel. The sinograms are then mathematically reconstructed and converted to tomographic 2D slices. The most common reconstruction technique is called filtered back-projection, based on the "Fourier Slice Theorem" (Landis and Keane, 2010). The reconstructed 3D dataset consists of horizontal reconstructed tomographic 2D slices stacked together along the z-axis in grey scale value (Figure 3.5a). Digital image analysis can then be applied to the reconstructed 3D dataset to visualize and quantitatively analyse the tomographic data. As reconstructed images contain noise, pre-processing using filters is needed. During this stage other common operations can include resizing, scaling, sharpening or masking of the greyscale data (Fig 3.5b). Material or structures of interest are then selected from the images by the process of segmentation. Image segmentation is a process of images

classification, which needs to be assessed based on the features and contrast present between the sample components. Several segmentation procedures have been developed in function of the different need of the case study, time constrains, computational power available and other factors (Guntoro et al., 2019). For example, objects can be divided into groups based on the range of the voxel values through the use of a global grayscale threshold methods, or by using boundary-based methods, using relative differences in greyscale to detect edges between materials.

In this thesis the used segmentation is the Weka (Waikato Environment for Knowledge Analysis) segmentation method, a supervised label-based segmentation augmented by machine learning (Arganda-Carreras et al., 2017). To do label-based segmentation, a user first selects regions of interest, from which the contour is then extended until a significant difference in material absorption is seen. The Weka has been compared to other algorithms and found to perform similarly. (Berg et al., 2018). Segmented data can be visualised as is or undergo post-processing operations to improve the clarity of the dataset (Fig. 3.5b). Operations can include morphological operations (erosion, dilation, opening, closing), and removal of unwanted segmented spots/phases.

Lastly characterization, quantification and analysis of each segmented material such as size, shape and orientation analyses are commonly carried out following similar procedure as in 2D image analysis (e.g. Heilbronner and Barrett 2013).

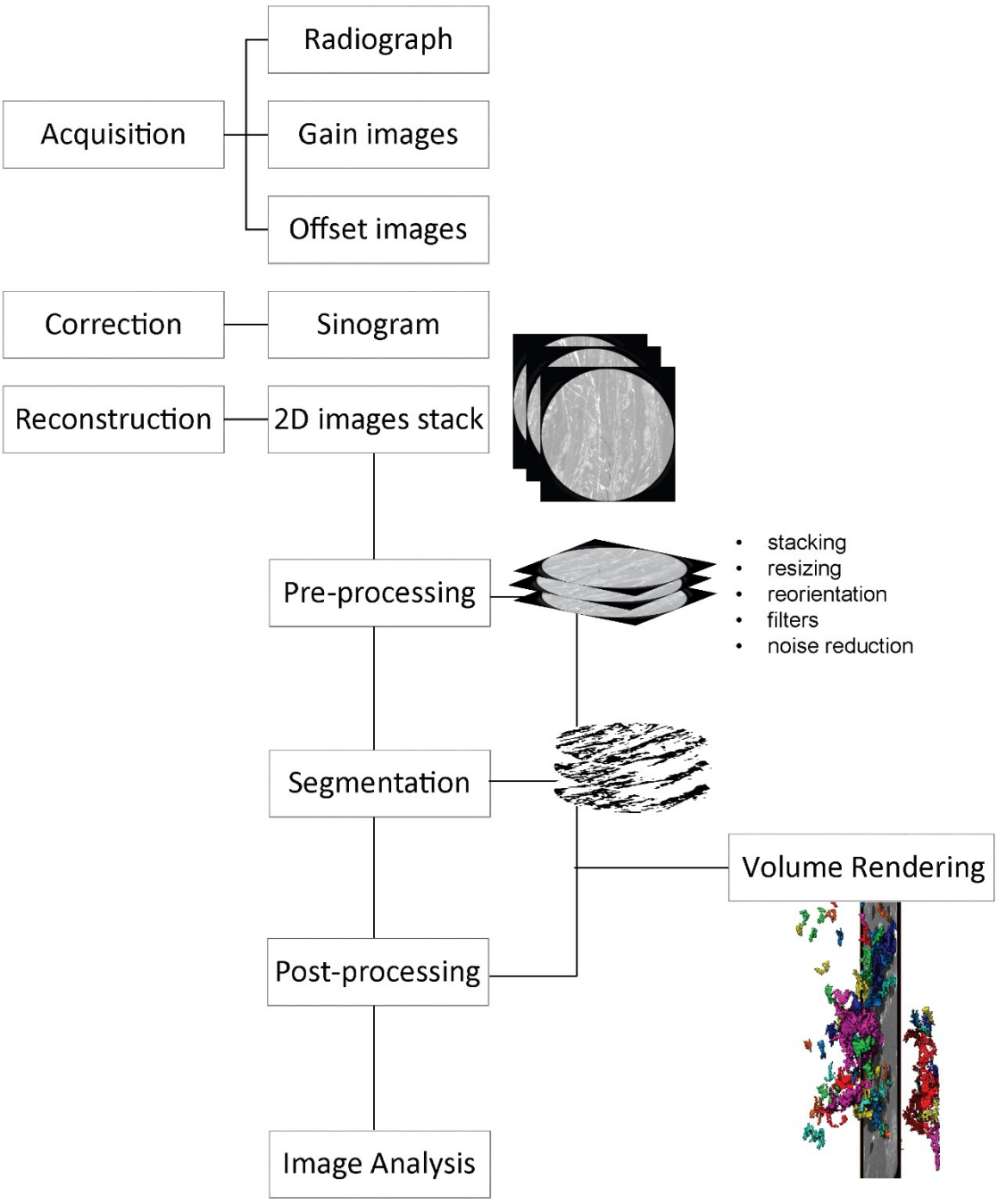

Figure 3.5 Workflow for µ-CT analysis.

3.5 Helium pycnometry

Helium pycnometry is a gas expansion method that accurately measures the effective porosity and solid-phase volume of objects of irregular or regular shape (Anovitz and Cole 2015, Tamari 2004). The method works by calculating the volume of gas, helium,

displaced by the sample. Helium is commonly chosen among other gases since, due to its size, it can easily penetrate small pore; moreover, it is inert, and can be considered an ideal gas (i.e. compressibility factor z=1.0) for ambient pressure and temperature (Weber and Bastick 1968, Neimark and Ravikovitch 1997; Talu and Myers 2001).

The instrument for He pycnometry comprises two chambers. One is the sample cell, which has volume V_{cell}. In this sits the sample, with known volume V_{samp}. So the volume of gas in the sample cell is (V_{cell} - V_{samp}). This chamber is connected through a valve to a second chamber, known as the 'expansion volume or reference chamber', with volume V_{exp}. Both the sample cell and the expansion volume chamber are at ambient pressure P_a and T_a. He gas is introduced into the sample cell and its pressure is raised to an arbitrary value P_1. Then the instrument opens the valve between the sample cell and the expansion volume. The gas expands from the sample cell into the expansion volume, until the pressures inside the two chambers are equal. This pressure P_2 will be intermediate between the two starting pressures P_1 and P_a. During the re-equilibration the Helium penetrates into the pores of the sample. The volume of the pores is then calculated by the instrument using the ideal gas law, from the following equation:

$$V_{\text{pores}} = V_{\text{samp}} - V_{cell} - V_{exp}\left(\frac{P2}{P2 - P1}\right) \qquad Equation\ (3.4)$$

3.6 Mercury intrusion porosimetry

Mercury intrusion porosimetry (MIP) is commonly employed in material science to measure the pore size distribution of powdered and bulk materials with open and connected pore structures (Webb, 2001; Cnudde et al., 2009; Sasanian and Newson, 2013; Anovitz and Cole, 2015).

The principle behind MIP is the idea that a liquid that does not wet surfaces can only enter capillaries when pressure is applied. The difference in surface tensions between a liquid and the solid surface on which it rests is expressed as contact angle. A liquid, such as water, forming a contact angle < 90 °with the solid surface is referred to as wetting (Fig 3.6). In the case of a non-wetting liquid, the surface energy of the liquid exceeds that of the solid, leading to a contact angle between 90° and 180°, and the liquid will form a bead (Fig. 3.6). For mercury the contact angle with the solid can vary between 120° to 150°, and a value of 140° is commonly assumed in MIP (Webb, 2001). The properties of the solid surface and whether or not the mercury is advancing, or retreating can be factors in the variation of the contact angle (Modrý et al., 1981; Sing 2004). There is an open discussion on whether those variations affect the MIP reliability, and development of methods to measure contact angle values for solid surfaces accurately is still underway (Salmas and Androutsopoulos, 2001; Drelich et al., 2020).

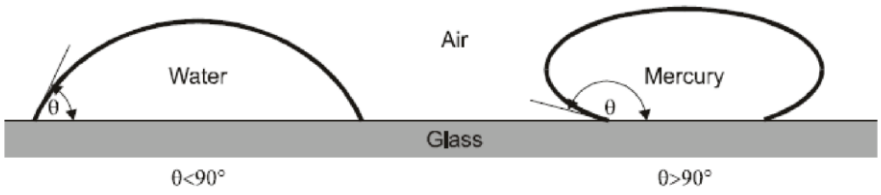

Figure 3.6 Comparison of wetting and non-wetting fluids. The shape of the fluid drop on the solid surface in the presence of air indicates its preferential wetting phase.

When pressure is applied to the mercury, it will be forced to progressively intrude the voids in the solid. The following relation, based on the Young-Laplace equation, can be used to express the pressure necessary for the mercury to intrude capillaries:

$$\Delta\rho gh = \pm\frac{2\gamma cos\theta}{r} = p \qquad Equation\ (3.5)$$

in which ρ is the density of the liquid, γ the surface tension of the liquid, θ the contact angle of the liquid, r the radius of the capillary, and p is the pressure.

MIP test is characterized by placing a sample into a sample holder, evacuating the container to remove gases and vapours, and filling the container with mercury under vacuum. The sample holder or cell is called dilatometer. The dilatometer can be separated into (i) a glass bulb that function as sample holder, for samples that can be a solid object, granules, or powder, and (ii) a capillary glass stem. The stem is greased to create a tight seal when the dilatometer is connected, and a metal bolt can be used additionally to keep connected the two units. The dilatometer stem is then covered from a metal electrode and placed into the porosimeter. A vacuum is created to remove possible trapped moisture in the sample, and the sample chamber is filled with mercury.

Pressure is then applied and the amount of mercury that intrudes the pore network is recorded as a function of the applied pressure. Pressure can be applied continuously or at increments, to assure that the flow of mercury can reach an equilibrium. The volume of intruded mercury is measured trough changes in the capacitance between the metal electrode surrounding the dilatometer stem and the column of mercury. Many MIP instruments presents a dual pressure system, with a low pressure and a high pressure set up, in which the dilatometer is placed into an oil hydraulic pressure chamber, where pressures up to 414 MPa are applied in an isostatic way. After reaching the highest pressurization event on each system, the pressure is decreased to ambient atmospheric pressure, and the volume of mercury leaving the pores is measured. The depressurization that results in the retraction of the mercury is referred to as “extrusion”. The resulting mercury porosimetry data are plotted as intrusion and extrusion curve

(Fig.3.7 a), plotted as volume of intruded mercury (expressed per unit weight of sample), as function of applied pressure.

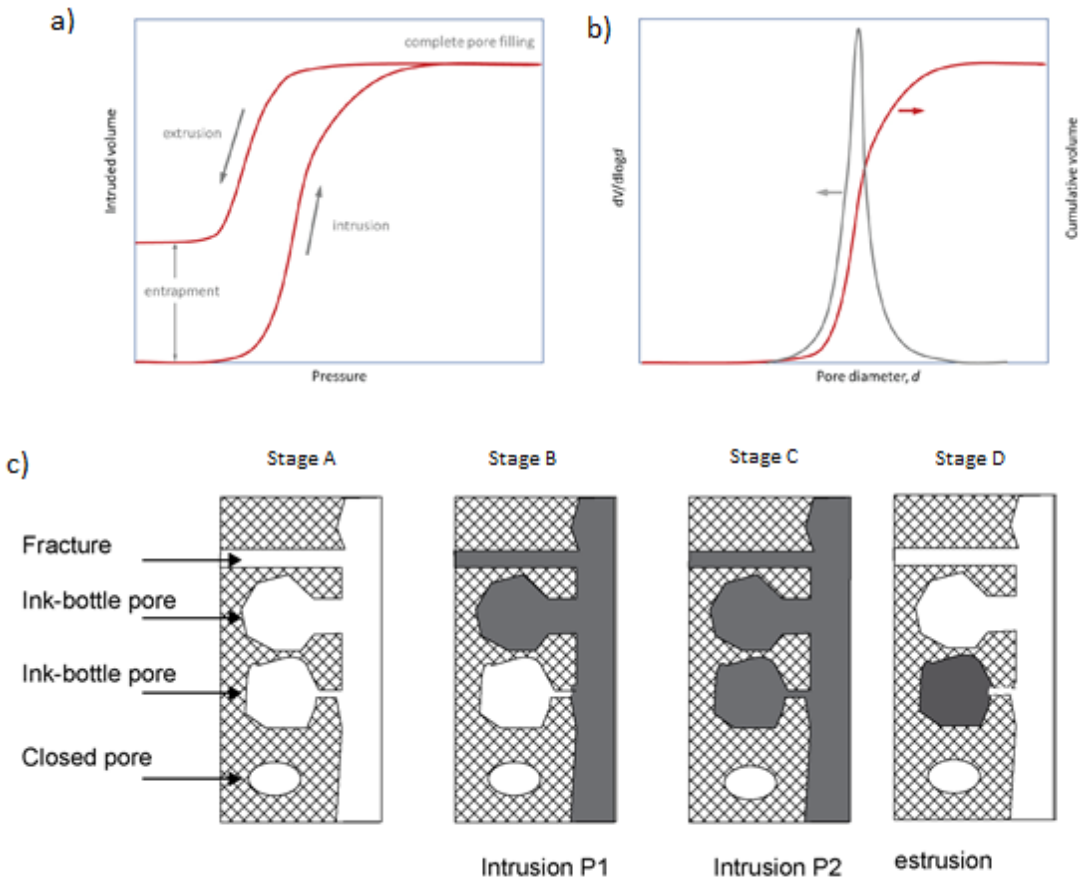

Figure 3.7 Scheme of idealised mercury porosimetry data and idealised pore system. a) The intrusion proceeds from low pressure(left side of the image) to high pressure, followed by extrusion, which occurs when the pressure is decreased.b) Pore size distributions. The maximum in the grey line can be read as representative of the inflection point of the red line. (c) schematic drawings of void spaces in a rock specimen illlustrating mercury entrapment with respect to different arrangements of pore and pore throats (modified from Staněk and Géraud, 2019, used under CC BY 4.0).

Intrusion and extrusion curves frequently present a different path, especially at lower pressure, thus forming hysteresis loops (Giesche, 2006). During the intrusion process, mercury can only access the connected porosity that can be reached by the mercury at a given pressure. This implies that the obtained pore size is representative of the size of entrance of the pore. Using a simple scheme to illustrate this phenomenon (Fig. 3.7 c,

stage A), pore space in a rock is characterized by larger open spaces, referred to as pores or fracture, that are connected by smaller spaces or constrictions referred to as throats (Wardlaw et al., 1987). Under increasing pressure, mercury fill only pore volumes that can be reached at the given pressure, which results in larger pores being 'shielded' from narrower pore throats (Stage B, Fig 3.7a, c) (Giesche, 2006). Therefore, the volume of some larger pores will be evaluated at pressure consistent with smaller pore throat (Stage C, Fig 3.7a, c). The mercury that entered a large pore when it was accessible by a narrow throat remains trapped after the mercury pressure is reduced (Wardlaw & McKellar, 1981). After extrusion, fractures and pores with a high throat to pore size ratio are free of mercury because they do not trap it (stage D in Fig. 3.7a, c). The trapped porosity corresponds to the volume that remains in the specimen at ambient pressure at the completion of the extrusion indicated by pore-throat configurations with a low throat to pore size ratio (Fig. 3.7 a)

Another plot commonly used to represent MIP data is the pore size distribution, which can be represented as cumulative pore volume (percentage of total or volume per unit mass) plotted against the pore diameter (d) or radio, or in the case of this thesis, as the first derivative of the cumulative curve, (dV/dlogd) as a function of the pore diameter (Fig 3.7 b)

4 Deformation microstructures, stress history and fluid pressure variations along BFZ045

4.1 Cyclical deformation behaviour in quartz

There have been several studies that identify quartz micro fabrics indicative of brief co-seismic damage under BDT circumstances, when quartz suffers plastic deformation in the inter-seismic interval.

Experiments of non-steady state behaviour in quartz (Trepmann et al., 2007, Austin and Evans, 2009; Kidder et al. 2016) and the result comparison to natural rock studies (e.g., Kidder et al. 2012, Trepmann et al., 2017) provided several evidence of transient damage.

During the seismic cycle, transient high stress deformation can be followed by recrystallization during viscous relaxation at decreasing stresses (e.g., Trepmann and Stockhert, 2003). When there is a significant stress decrease, the microstructures that can be found include bands of fine new grains (isometric and without CPO) that overprint cracks within quartz grains (Figure 4.1a, Trepmann and Stockhert, 2013) or a partial foam texture (Kidder et al. 2016). When stress relaxation is slower, new grains generate a shape preferred orientation (SPO) and a CPO, that indicate deformation affects also the newly formed grains. (Fig, 4.1b). The deformation of new grains may be the product of a single event in which the stress level after the stress drop was sufficiently high for effective plastic deformation, or it could be the consequence of several subsequent deformation events. (Trepmann et al, 2017)

Quartz microstructures may be utilised to quantitatively measure stress history during transient deformation events (Kidder et al. 2016). More precisely, stress fluctuations during crystal-plastic deformation can be linked to bimodal distributions of recrystallized grain sizes (Fig 4.2a, Kidder et al., 2016). Even if the youngest population of recrystallized grains does not reach steady state, quantifiable information on the stress history may be obtained from the microstructures and grain size. As a result, the two separate populations represent a two-stage deformation history in which a high stress event overprinted a previous lower stress deformation event. (Kidder et al, 2016) The smaller recrystallized grain size provides a reliable constrain on the magnitude of the differential stress during the most recent deformation.

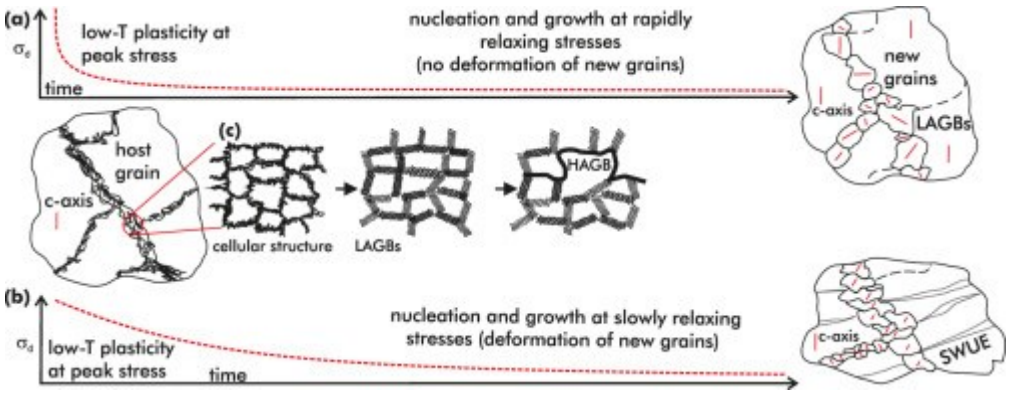

Figure 4.1 Quartz microstructure developed for rapidly relaxing stresses following a high stress deformation event (a) and for slow relaxation rates (b). From Trepmann et al. (2017).

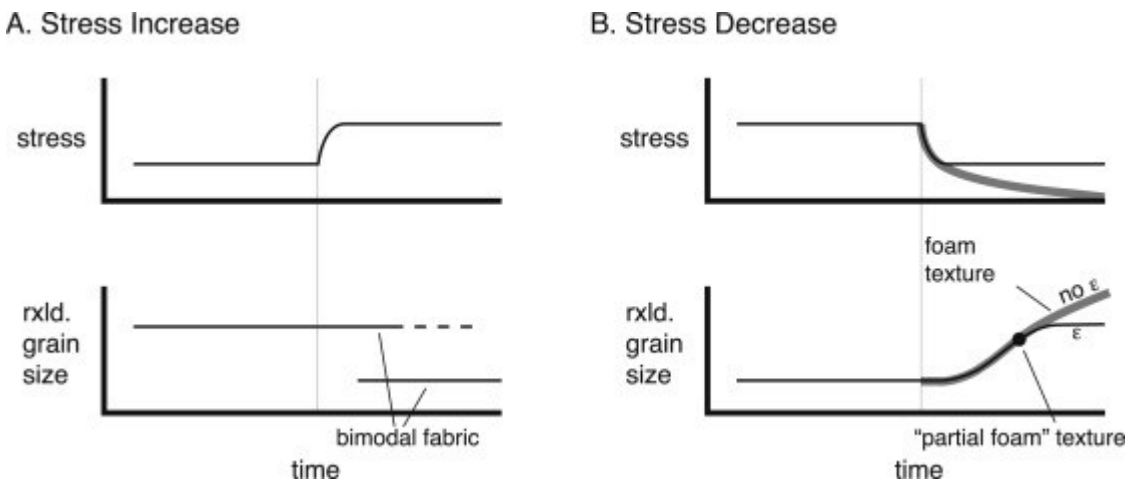

Figure 4.2 Grain size evolution observed in the experiments of Kidder et al (2016) for samples experiencing switches from low to high stress deformation (A) and from high to low stress deformation (B).

Other than stress variation, high pore fluid pressure has a main role in the development of microstructures recording deformation at the BDT. An example is given in Kjøll et al. (2015), where high pore fluid pressure triggered brittle fracturing inside quartz veins that were undergoing ductile deformation. After drop in fluid pressure, the cracks were eventually filled by dynamic recrystallization or neo-crystallization. As a result, there were several instances of viscous-brittle-viscous deformation cycles. Proposed microstructural evidence for fluid driven fracturing are fluid inclusions trails parallel to the intracrystalline bands of recrystallized grains. Fluid inclusion abundance can also provide evidence for brittle co-seismic deformation at depth (Song et al, 2020). Since fluid-filled pores along grain boundaries may also be introduced by creep cavitation during grain boundary sliding (Fusseis et al., 2009; Menegon et al., 2015) or Zener-Stroh cracking during dislocation creep (e.g. Gilgannon et al., 2017), it is important to first determine the quartz deformation mechanisms.

Quartz is ideally suited to investigate the relationships between deformation mechanisms and differential stress, as there exist experimentally calibrated paleopiezometric relationships for quartz that relate the grain size of recrystallized

grains to the flow stress (e.g. Stipp and Tullis 2003; Cross et al., 2017). Recrystallized grain size piezometers relate stresses and recrystallized grain size as follows (Eq. 1):

$$\Delta\sigma = BD^{-x} \qquad Equation\ (4.1)$$

Where Δσ is the differential stress, D the recrystallize grain size, B and X are empirical constant.

Stipp and Tullis (2003) experimentally calibrated a paleopiezometer for quartz, in which the size of dynamically recrystallized grains of a quartzite is a function of differential stresses. The grain size was observed with the use of light- optical microscopy and CIP (Computer Integrated Polarization) microscopy, and the recrystallized grains were distinguished from porphyroclasts manually and on the basis of the bimodal grain size distribution when observed.

Cross et al. 2017 proposed a routine to separate recrystallized and relic (porphyroclasts) grains of quartz, by quantifying the degree of intracrystalline lattice distortion in each grain. Intracrystalline lattice distortion is proportional to dislocation density and can be visualized using grain orientation spread (GOS), which is the average value of the misorientation angle between every pixel in a grain and the mean orientation of that grain. GOS has a positive correlation with differential stresses, reflecting an overall increase in lattice distortion with stress. The average 2-dimensional recrystallized grain size can then be calculated as the root mean square diameter from all measured recrystallized grains (Stipp and Tullis, 2003).

The recalibrated EBSD- based recrystallized paleopiezometer for quartz is the following:

$$D = 10^{(3.91 \pm 0.41)} \cdot \sigma^{(-1.41 \pm 0.21)}$$

4.2 Methods

The study of deformation microstructures was conducted using petrographic and scanning electron microscopy (SEM). SEM and EBSD analysis were performed at the Plymouth University Electron Microscopy Centre using a JEOL 7001 field emission gun SEM (equipped with EBSD and EDS detectors) and a JEOL 6610 with tungsten filament (EBSD detector). Panchromatic CL analysis were conducted at ETH of Zurich, using a FEI Quanta 200 F with a panchromatic camera, in order to observe growth features in quartz and possible evidence of healed cracks (e.g. Mills et al, 2017).

Thin sections used for Electron Backscatter Diffraction (EBSD) analysis were polished with colloidal silica before being carbon coated. Data were acquired on a NordlysNano and a NordlysMax EBSD detector (Oxford Instruments). Working conditions during acquisition of the EBSD patterns were 20 kV, 20 mm working distance, 70° sample tilt and high vacuum. AZtec software was used for pattern indexing on rectangular grids with step size of 0.7 µm, 1 µm and 1.8 µm. EBSD patterns were processed with the Channel 5 software (Oxford Instruments), and noise reduction was performed following the procedure suggested in Bestmann and Prior (2003).

After acquisition, EBSD data was processed with Oxford Instrument CHANNEL 5 software. Raw data firstly underwent noise removal, with the cleaning of poorly indexed points. The routine for each analysis comprised the removal of data point with a mismatching orientation with the surrounding pixels and a different degree of extrapolation of zero solutions, where the orientation of unindexed pixels is extrapolated based on the orientations of the neighbours.

Cleaned EBSD data was used to produce crystallographic orientation maps and grain size distribution maps. Orientation maps and pole figures were used to show the presence of a crystallographic preferred orientation in the samples. Inverse pole figure maps (IPF) are colour-coded to visualise how a specific direction (e.g. one of the axes of the SEM chamber) is oriented with respect to the crystal lattice of the investigated phase. Pole figures (PF) are stereographic projections showing the orientation of specific crystallographic planes and directions of the analysed phase (quartz in this case) with respect to an external reference frame. The choice of crystallographic planes and directions to plot depends on the symmetry of the crystal and on known slip systems. The specimen reference frame of the samples (axes X, Y, Z) investigated here is X parallel to the stretching lineation, Z pole to the mylonitic foliation and Y perpendicular to the XZ plane.

The EBSD data are presented as grain size maps, with a 10° misorientation threshold to define grain boundaries (in black), while low-angle boundaries are defined as having misorientation > 2° and < 10° and are displayed as white or cyan lines. Quartz c-axis orientation is presented as pole figures on equal area, lower hemisphere projections, and one point per grain. The XY plane of the pole figure is parallel to the shear zone foliation, X is parallel to the stretching lineation, and Z is normal to the foliation.

The grain size was measured as the diameter of a circle with equivalent area to the grain. The spread of the internal orientation of each grain was shown as Grain Orientation Spread (GOS) maps and was considered as a measure of the internal strain of the grain. A trade-off curve was used to calculate a threshold GOS value, which separates recrystallized grains from relict grains, following the procedure outlined in Cross et al. (2017). It is known that the GOS method has a slight grain size bias, which results in higher GOS values for larger grains (Cross et al., 2017). However, this bias has no impact on the ability to separate between relict and recrystallized grains where

their size overlaps on the cumulative grain size distribution, and the GOS-based separation is considered robust (Cross et al., 2017).The average recrystallized grain size, calculated as root mean square (RMS), was used to apply the EBSD calibrated recrystallized grain size piezometer for quartz (Cross et al., 2017). Grain reference orientation deviation angle maps (GROD) were used to visualise subgrains only partially outlined by low-angle boundaries and to estimate their size. GROD maps are colour coded to show the angular deviation at each point of a grain from the average orientation of the grain

Major element mineral chemistry of chlorite and white mica was measured with Electron Microprobe Analysis (EMPA), at the Department of Earth Sciences, University of Milan, Italy. Carbon coated thin sections were probed with a JEOL 8200 Super Probe equipped with 5 wavelength-dispersive spectrometer (WDS). Working conditions were set to 15 kV of probe current, 5nA current on sample, 1 μm beam diameter. Natural minerals were used for standardization, measurement times were 30s on peaks and 10s on backgrounds of the X-ray lines.

Pressure was estimated using the Si-in-phengite geobarometer , which require to have stable K-feldspar next to the Phengite (Massonne and Schreyer, 1987). White mica composition was measured for grains parallel to the foliation associated with neoblasts of K-feldspar. Structural formulae were calculated assuming 11 oxygens.

Raman spectroscopy was applied for feldspar and opaque phase identification and for carbonaceous material (CM) characterization. Data acquisition was conducted at the Department of Chemistry, University of Padua (Italy), using a Thermo Scientific DXR MicroRaman spectrometer, equipped with a 532 nm depolarised laser. Raman analysis was also carried out at the Department of Mathematical, Physical and Computer Sciences of the University of Parma (Italy) using a Jobin-Yvon Horiba LabRam

spectrometer equipped with He–Ne laser (emission line 473.1 nm) and motorized XY stage. Spectra were acquired from polished thin section, using a laser power of 5 mW, spectrograph aperture 25 μm pinhole, and 50X or50X low distance objective. The estimate spot size was 1-2 μm in diameter and spectral resolution of 2 to 4.4 cm^{-1}, with acquisition time of 30–90 s. Feldspars composition was classified on the basis of the acquired Raman spectra, as suggested in Freeman et al. (2008), using a comparison with standard Raman spectra from the RRUFF Project database (Lafuente et al. 2015). To assure a good statistical analysis of the CM structural heterogeneity, only samples with > 10 CM spectra were taken in consideration.

Omnic software (Thermo Fisher Scientific) was used for Raman spectrum decomposition, sing the software Lorentian/Gaussian function, following the procedure described in Kouketsu et al. (2014). Peaks with centre in position at~ 1580 cm-1, 1350 cm-1 and 1620 cm-1 were identified respectively as G, D1 and D2. R2 parameter, defined as the ratio between the peaks area D1/(D1+D2+G) was calculated for each measurements.

A linear relationship between temperature and the Raman parameter R2 forms the basis of the CM geothermometer (Beyssac et al., 2002). Temperature can be estimated to ± 50° C in the range 330–650° C. Deformation can affect the internal disorder and underestimate the temperature obtained from the spectra analysis (Kirilova et al., 2017). To consider the possible role of deformation, analysis of CM both in the host rock and along the D4 mylonitic foliation were collected. Care was taken to avoid CM within cracks, and to prevent altered measurement from CM damaged during the thin section polishing, we performed measurements by focusing the laser beam on CM beneath the surface of a transparent adjacent grain as suggested in Beyssac et al. (2002). CM in the host rock was analysed using λ=514 nm, while CM in the mylonite was analysed using λ=532 nm. To avoid error in the temperature estimation we applied two different

geothermometer calibrated for the different laser wavelength used to collect the data: Beyssac et al. (2002) for the λ=514 nm analysis and Aoya et al. (2010) for the λ=532 nm analysis. Although both give similar results, the equation given in Beyssac et al. (2002) for the Raman CM geothermometer is linear whereas that in Aoya et al. (2010) is quadratic.

4.3 Results

4.3.1 BFZ045 fault zone structure

The analysed samples come from two selected sub-horizontal drill cores: (1) a 2 m continuous section along the drill core PH-28 (PH stands for pilot hole), with orientation SE-NW taken at a depth of 433 m, and (2) selected samples of fault rocks from drill core PH-16(Fig. 4.3). Both drill cores intersect the fault BFZ045, which exploits a pre-existing mylonitic fabric. BFZ045 is a sinistral N-S sub-vertical strike slip fault (87/095, dip/dip direction) (Fig. 4.3). Photograph of selected section of the drill core PH-28 are shown in Appendix A.

A narrow (20 cm) cataclastic fault core overprints a banded mylonite in BFZ045. Cataclasite foliation runs parallel to mylonitic foliation. Semi-cohesive fractures (presence of chlorite slickensides and millimetre calcite-filled veins) and thin (1 cm) localised cataclasites in the associated damage zone. Mylonite stretching lineation is characterised by quartz and feldspar rodding and muscovite mineral lineation. The stretching lineation has an average orientation of 10/168 (plunge/trend), which is parallel to the average orientation of the cataclasite slicken lines and fault striations.

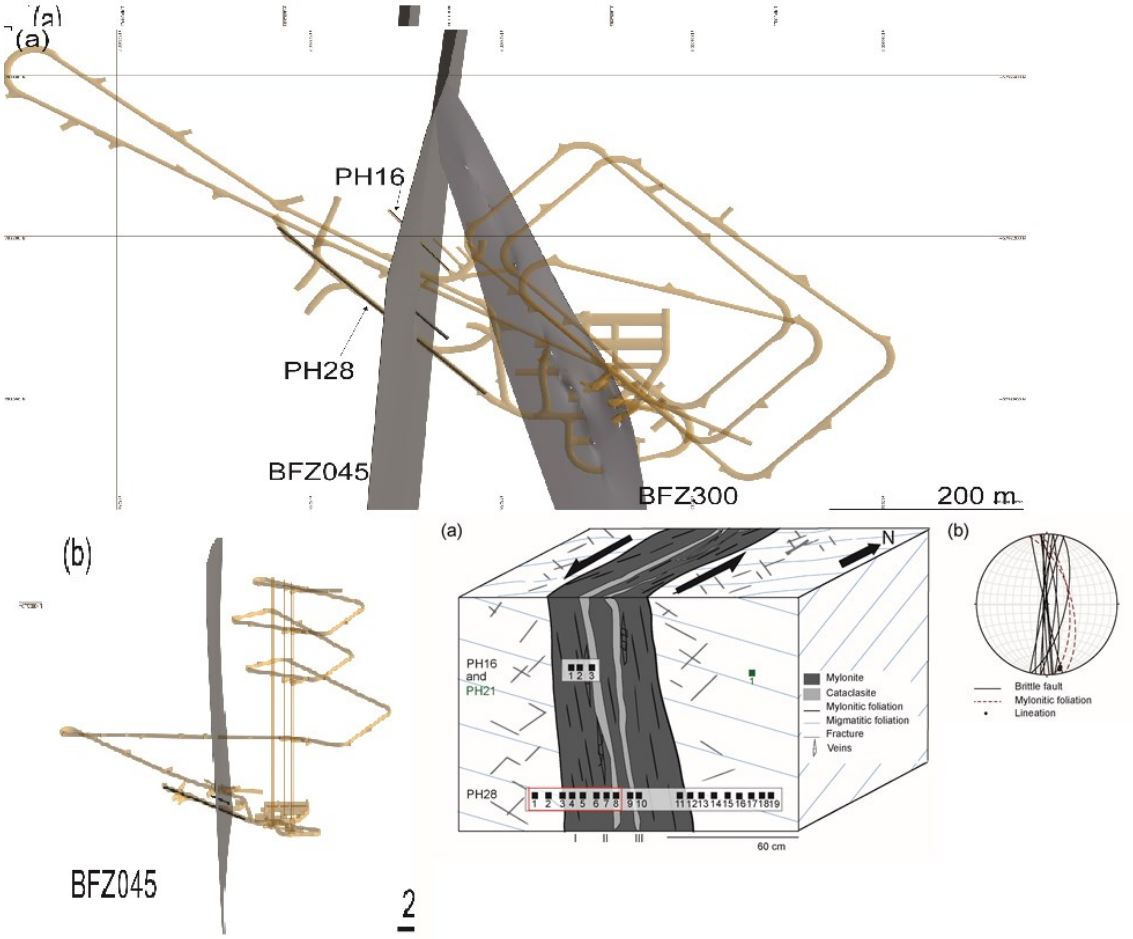

Figure 4.3 BFZ045 fault geometry. a,b 3D representation of BFZ045(grey) intersecting the excavated repository(yellow). Black lines indicate location of drill core used in this study.(c) Schematic representation of fault architecture from core logs, vertical axis not to scale. Grey rectangles locate the studied drill cores PH28 and PH16, black squares show sample location. The red rectangle indicates the samples shown in figure 4. (d) Stereoplot of BFZ045 fault core orientation and mylonitic foliation observed at different drill hole intersection in the Onkalo facility (Aaltonen et al., 2016).

Stepped slickensides indicate a dominant sinistral sense of shear, although striations associated with dextral kinematics have also been observed (Aaltonen et al., 2016; Nordbäck et al., 2018). The host rock and mylonite are covered in a network of veins which are frequently composed of quartz, calcite, and chlorite, in addition to fractures which are also chlorite-filled (Fig 4.3; Aaltonen et al, 2016). The damage zone is located between 0.5 and 1 m from the fault core, and it is characterized by a higher

fracture density that reduces in average fracture spacing from 3 cm to roughly 0.5 cm as one moves closer to the fault core. The brittle core of BFZ045 defined by cohesive cataclasites that overprint the mylonite is referred to as the "fault core" in this context. This implies that both the migmatitic host rock and the BFZ045 mylonite are impacted by the BFZ045 damage zone.

4.4 Petrography

Figure4.4 depicts typical samples of core PH28 from left to right, from the damage zone in the host rock to the fault core. High resolution images of the upper half core are present in Appendix A. The host rock is a veined migmatite with coarse grains (Fig. 4.4, I). The farthest occurrence of chlorite-filled fractures, recognised microscopically as deformation bands coupled with apparent slip, served as a proxy for defining the extent of damage to the host rock. There are a total of 12 fractures longer than 5 cm along the core, with 7 of these being within 10 cm of the fault core (west side of the core). The host rock and mylonite have a sharp contact. The millimetre-spaced mylonitic foliation is defined by a compositional layering of alternating quartzo-feldspathic domains and mica-rich domains (Fig. 4.4, II). Multiple slip surfaces marked by 0.5 – 10 cm thick cataclastic domains overprint the mylonite along the foliation (Fig. 4.4, III). Locally, phyllosilicates and trails of opaque minerals define thin (<1 mm thick) anastomosing foliation planes within the cataclasites, which wrap around sub-angular fragments of the mylonitic precursor. Along a thin (<5 mm thick) slip surface, two pseudotachylyte injection veins intruding the mylonite at a high angle have been observed, which demonstrates the transient seismogenic behaviour of BFZ045. Calcite veins (1-3 mm thick) locally overprint the fault core both at high angle to the foliation and along the slip surfaces.

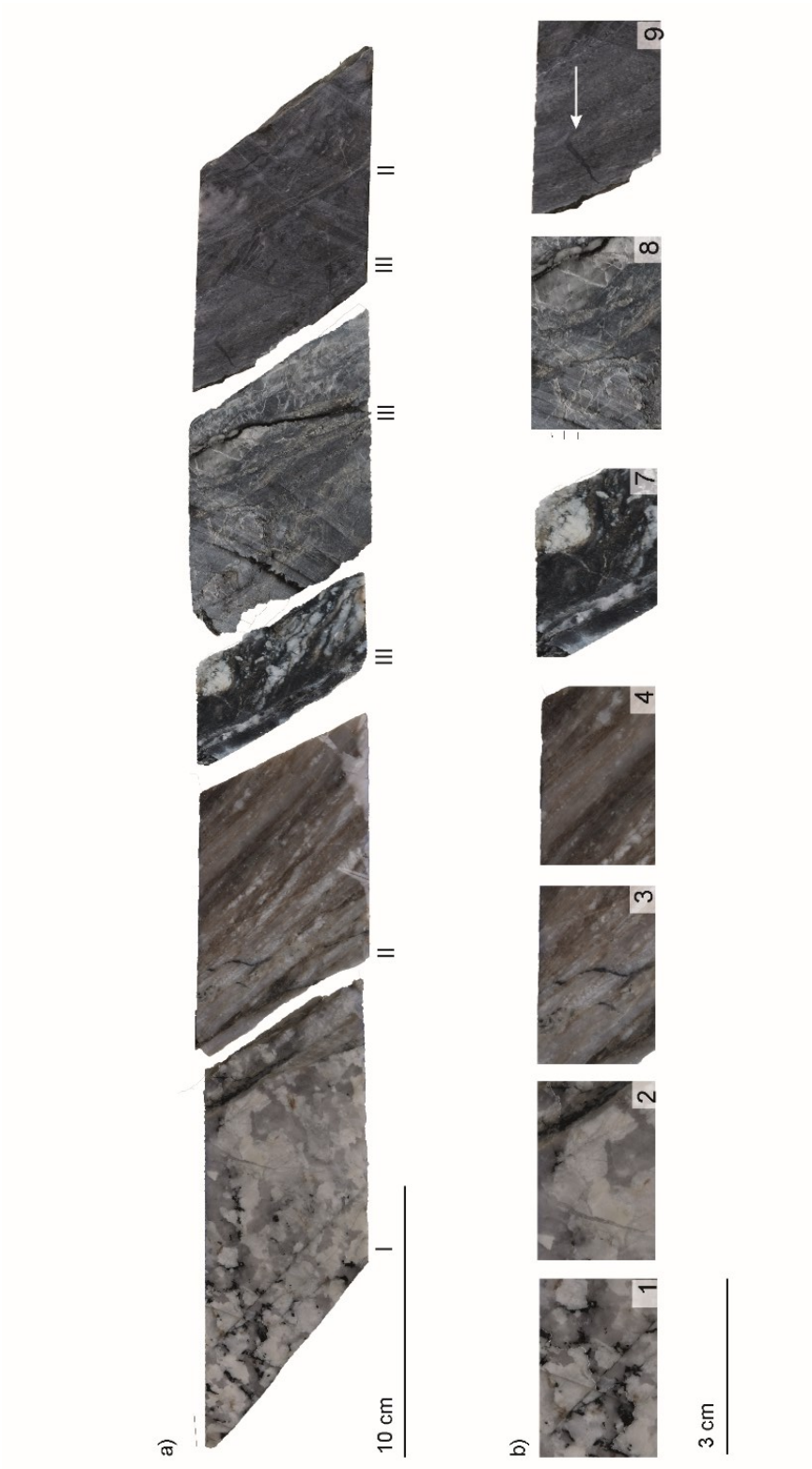

Figure 4.4 Samples from PH28 drill core representative of different domains of the fault: damaged coarse-grained host rock (I), and fault core with mylonite and chlorite rich cataclasites (II-III). B)Rectangle representing the area of petrographic thin sections. White arrow points to pseutotachylyte injection veins.

4.4.1 Host rock

The migmatitic host rock mineral assemblage observed in the PH28 samples consists of 50 % of quartz, 40 % K-feldspar, and plagioclase, and the remaining 10% of white mica, graphite, alteration minerals of plagioclase (sericite) and secondary chlorite, and calcite veins. Coarse-grained (1-2 mm) quartz and feldspars are homogeneously distributed in an equigranular texture and show mostly straight grain boundaries (Fig. 4.5a). K-feldspar occurs as orthoclase, with a well-developed veined perthitic texture. Plagioclase, albitic in composition as determined from Raman analysis, has lamellar twinning, and is commonly altered to sericite. Both types of feldspar locally show bent twin lamellae and undulose extinction. Microfractures in feldspars are preferentially oriented parallel and at low angle (≤ 20°) to the mylonitic foliation. White mica was observed occasionally as millimetric sub-euhedral grains. Quartz displays intracrystalline deformation features such as undulatory extinction, wide extinction bands (WEBs, following the terminology of Derez et al., 2015; Fig. 4.5b), and bulges resulting in sutured grain boundaries (Fig. 4.5c; Stipp and Kunze, 2008). WEBs are locally bounded by fluid inclusion trails with different orientations, which give them a blocky or slightly elongated aspect (Figs. 4.5b-c). Two main sets of intracrystalline fluid inclusion trails are observed, one at a low angle with respect to the mylonitic foliation and the other perpendicular to the foliation. Fine bulges (10-20 μm in size) occur along grain boundaries and intercrystalline fractures (Fig. 4.5b). Quartz grains in the proximity of the mylonite develop intracrystalline bands of recrystallized grains sub-parallel to the foliation, with grain size of ~ 30-60 μm (Fig. 4.5c). Shear bands in the deformed host rock appear as cohesive micro-cataclasites, with fine grained (< 10 μm) chlorite surrounding angular feldspar and quartz clasts.

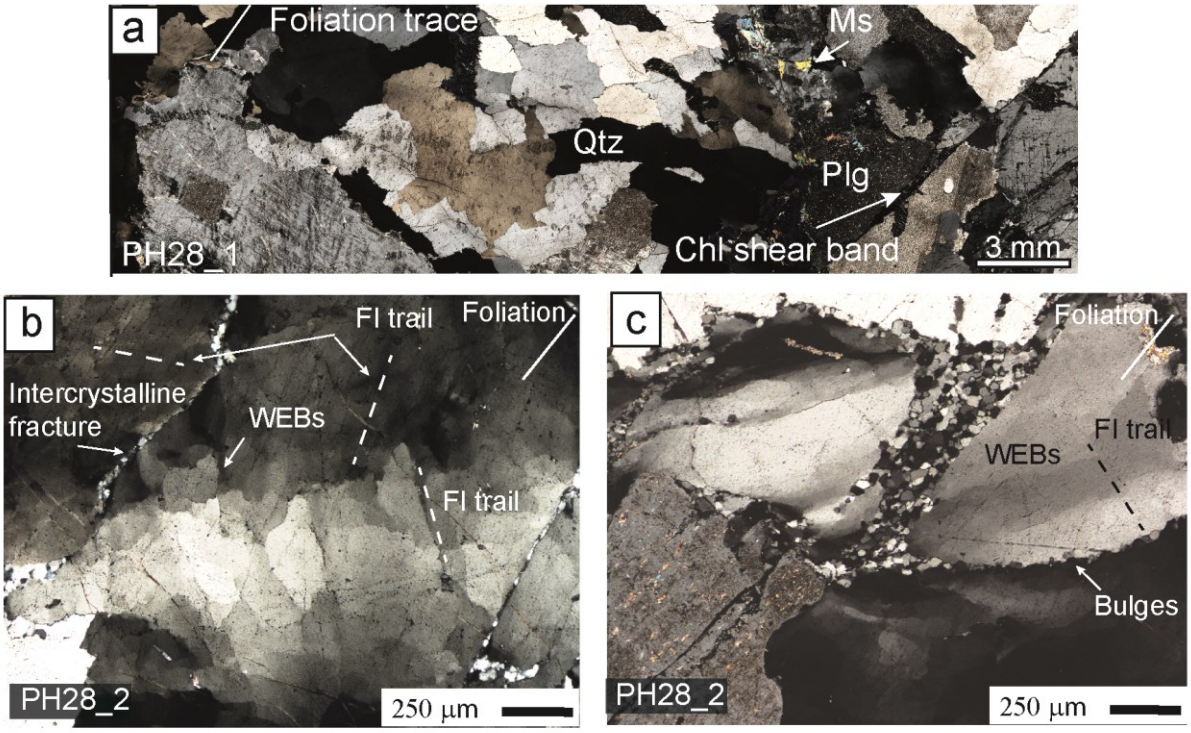

Figure 4.5 Polarized light microscope images of the damaged host rock (a), and representative quartz microstructures (b-c). Cross polarized light. (a) Host rock showing the original magmatic textures and mineral assemblage. White arrow shows a chlorite-rich shear band oriented at a low angle to the mylonitic foliation of BFZ045. (b) Quartz with wide extinction bands (WEBs) and undulatory extinction. WEBs are bounded by sets of fluid inclusions trails (FI trail, dashed lines). Intercrystalline deformation bands and well-developed FI trails developed sub-parallel to the mylonitic foliation. (c) Polygonal recrystallized quartz grains, with small grain size (~20 µm), forming bands oriented sub-parallel to the mylonitic foliation. The white arrow shows sutured grain boundaries between magmatic quartz grains, indicative of bulging. Foliation trace is projected as a white line on to the images from the adjacent foliated host rock.

4.4.2 Mylonite

The relative mineral abundances in the mylonite are slightly different from those in the host rock, and consist of 50% quartz, 20% white mica + chlorite, and 30% K-feldspar + plagioclase. Accessory phases are graphite, rutile, anatase, and apatite, which are typically found associated with chlorite to form black seams. The spaced mylonitic foliation is defined by a compositional layering between alternating millimetre-thick

quartz bands and narrower (0.2 to 1 mm thick) mica- and feldspars-rich bands (Fig. 4.6a). Porphyroclasts of K-feldspar are up to 7 mm in size and show asymmetric pressure shadows filled with chlorite + muscovite ± feldspars (albite and K-feldspar), with a geometry indicative of a sinistral sense of shear. Feldspars in the mylonite present brittle behaviour, with domino-type fragmented porphyroclasts. Neoblasts of K-feldspar are commonly observed in the pressure shadows of porphyroclasts or together with fine-grained white micas along the mylonitic foliation.

Quartz in the mylonite presents various degrees of recrystallization (Figs. 4.6b, c). In zones where ductile deformation is less prominent (e.g., samples PH28_3, PH16_1, Fig. 2), quartz retains a coarser grain size (1-5 mm), and forms slightly asymmetric (sigmoidal-shaped) grains. Internally, the grains display patchy undulatory extinction, well-developed blocky to elongated WEBs (100-300 μm wide), and discrete intracrystalline bands (< 200 μm wide) of bulges and recrystallized grains preferentially oriented sub-parallel to the foliation and at ca. 45° from the foliation, measured anti-clockwise (Fig. 4.6b). The host grains contain small subgrains (< 60 μm), which, towards the boundaries of the host grain, make transition to aggregates of recrystallized grains of size comparable to the subgrains, forming typical core-and-mantle microstructures (Fig. 4.6b).

In zones of complete recrystallization, quartz forms highly elongated polycrystalline ribbons (up to 0.5 – 1 mm thick, and up to 2 cm long) parallel to the foliation (Fig. 4.6c). The recrystallized grains locally define a shape preferred orientation (SPO in Fig. 4.6c) inclined with 10° to 30° with respect to the trace of the foliation, consistently with the bulk sinistral sense of shear.

Adjacent to the cataclastic fault core, ataxial/unitaxial (i.e., with no visible median line; Bons, 2012) quartz veins occur parallel to the mylonitic foliation (and to the layers of

recrystallized quartz) and contain grains elongated normal to the vein boundary (i.e. normal to the foliation; Fig. 4.6d). The vein crystals range in length from 200-400 μm and have a maximum thickness of 150 μm measured parallel to the vein. Quartz in the veins shows undulatory extinction and bulges at the grain boundaries (Fig. 4.6e) indicative of crystal plastic deformation. The recrystallized quartz in the mylonite surrounding the vein has a finer grain size than the one in the mylonite described in Figs. 4.6a-c, which is located farther away from the cataclastic core. Veins of radiate chlorite are observed cutting the mylonitic foliation at a high angle (~60°).

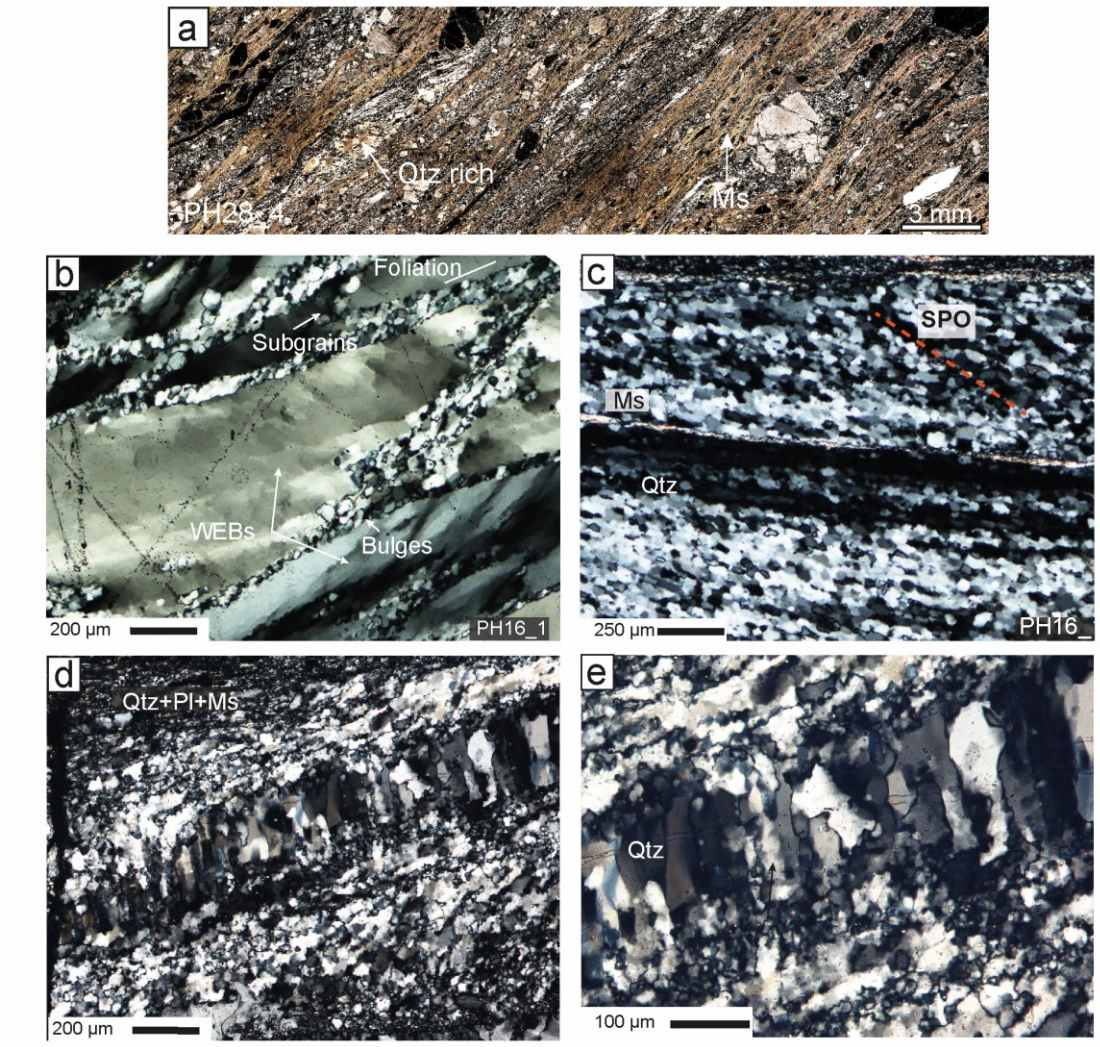

Figure 4.6 Microstructure of the BFZ045 mylonite. Cross-polarized light. (a) The mylonitic foliation is defined by the alternation of quartz-rich and mica-rich bands. Fractured porphyroclasts of feldspars are preferentially located in mica-rich domains. (b) Quartz ribbons in the shear zone boundary are stretched along the foliation and

show typical core-and-mantle microstructure, with recrystallization localized at the grain boundaries. Ribbons contain also well-developed WEBs. (c) Completely recrystallized quartz ribbon. The recrystallized grains show a shape preferred orientation indicating a sinistral sense of shear. Thin muscovite (Ms) layers define the mylonitic foliation, together with the elongated and recrystallized quartz domains. (d) Quartz veins along the foliation, filling a mode I fracture at a distance of ~ 1cm from the cataclasite fault core. Quartz grains elongation in the veins is normal to the vein wall and to the foliation. (e) High magnification view of the quartz vein. Bulges along the grain boundaries, and subgrains within the grains are visible.

4.4.3 Cataclasite

The brittle overprint in BFZ045 occurs mostly as 3 to 10 cm thick protocataclasites, that transition to 0.5 - 2 cm thick cataclasite bands in the fault core. The cataclasite is rich in chlorite and opaque minerals, which occur as fine-grained (2-10 μm) flaky aggregates within the fine grained (< 50 μm) quartz + feldspars + muscovite rich matrix. Locally, the cataclasite matrix contains a foliation defined by aligned phyllosilicates and anastomosing dark seams of opaque minerals. Clasts are predominantly angular fragments of the mylonite, ranging in size from 100 μm to 5 mm, and surrounded by a variable proportion of matrix. Quartz in the protocataclasite occurs in almost entirely recrystallized ribbons with a finer grain size (ca. 10 μm) than the one observed at higher distances from the brittle fault core (Figs. 4.7b-c vs Figs. 4.6b-c). The quartz clasts in the cataclasite (Fig. 4.7c) preserve the deformation and recrystallization microstructures observed in the mylonite near the cataclasite (Fig. 4.7b).

A pseudotachylyte generation surface is observed subparallel to a cataclastic band (Fig. 4.7a) and is identified from characteristic centimetric injection veins, branching in the mylonite at high angle to the foliation. The pseudotachylyte main generation surface is less than 1 mm thick and is parallel to the mylonitic foliation (Figs. 4.7a, d). The matrix of the pseudotachylyte is completely altered to a fine-grained, < 2 μm, chlorite and muscovite rich matrix that surrounds survivor clasts of quartz and rutile (Fig. 4.7d). Chlorite- and quartz aggregates commonly fill fractures within feldspar porphyroclasts

in the mylonite. Similar fractured feldspar porphyroclasts with quartz + chlorite fillings are observed inside slightly rotated clasts of mylonite in the protocataclasite (Fig. 4.7e).

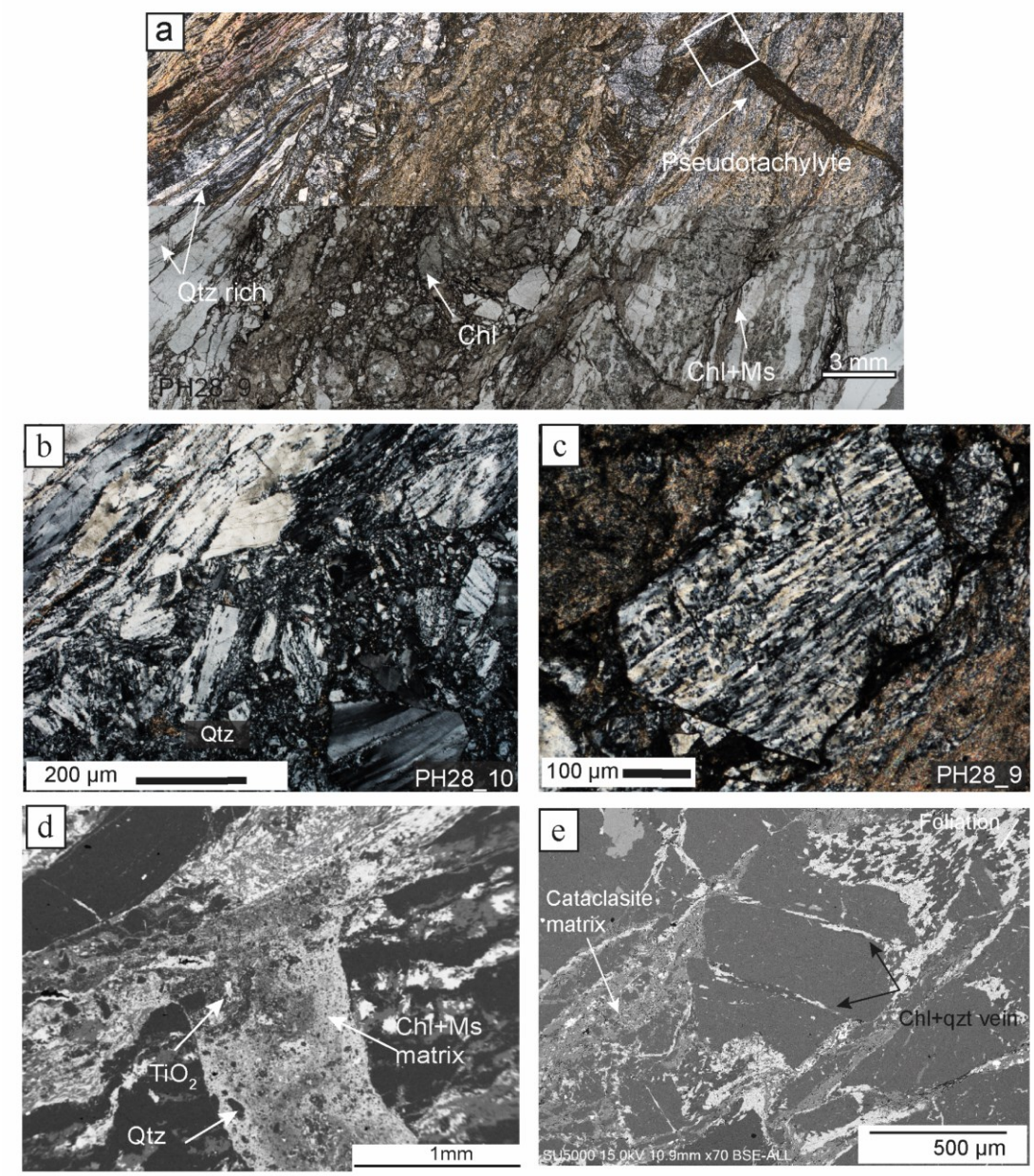

Figure 4.7 Microstructure of the BFZ045 brittle fault core. Cross-polarized light (a-c), plane-polarized light (a), and scanning electron microscope backscatter electron images (SEM-BSE) (d-e). (a) Cataclasite with characteristic pseudotachylyte injection veins (arrow). The cataclasite matrix is enriched in chlorite and Ti-oxides. (b) Contact between the mylonite (upper left corner) and the cataclasite. Quartz forms almost entirely recrystallized polycrystalline ribbons. (c) Detail of a sub-angular polycrystalline clast of quartz in the cataclasite. The trace of the mylonitic foliation is still visible in the clast and is only slightly rotated with respect to the trace of the foliation in the mylonite. The surrounding matrix is a fine mixture of white mica and plagioclase. (d) Pseudotachylyte injection vein. Rounded quartz clast (dark grey) and Ti-oxides (white) are surrounded by a chlorite and mica rich ultrafine-grained matrix. (e) Quartz + chlorite aggregates filling fractures within and strain shadows around

plagioclase porphyroclasts in the mylonite. The clast is slightly rotated within the protocataclasite. The white line in the top right corner indicates the trace of the mylonitic foliation.

4.4.4 Cathodoluminescence overview

Cathodoluminescence of mylonitic quartz-rich layers gave a continuous bright signal, with no clear zoning or differential luminescence (Fig.4.8C). CL images of quartz veins cutting the mylonite also does not show great differences in brightness (fig 4.8D There is no evidence of healed fractures in quartz in the CL images (Fig.4.8).CL images of quartz veins cutting the cataclasite show zoning features in the crystals (Figure 4.8e).

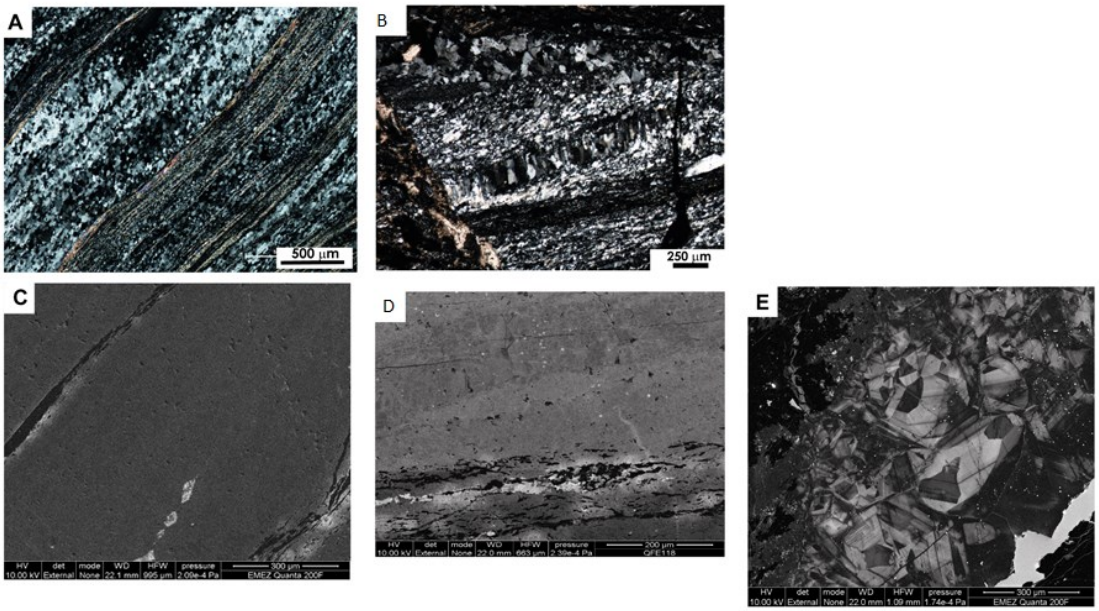

Figure 4.8 Cathodoluminescence images of mylonitic quartz-rich layers.

4.5 EBSD Analysis

4.5.1 Mylonite

EBSD analysis of the mylonite was conducted on sample PH16_1, which is located at the mylonitic shear zone boundary at a distance of 4 cm from the brittle fault core. EBSD maps were acquired from intracrystalline bands of recrystallized grains within an elongated mm- sized quartz grain (Fig. 4.9a), and from a highly recrystallized quartz layer along the mylonitic foliation (Fig. 4.10a).

The recrystallized grain size within the intracrystalline bands ranges from 5 to 60 μm (Fig. 4.9b, c,). The Grain Orientation Spread (GOS) within the recrystallized bands varies between 0° and 8.4°, with a threshold value of 1° between the recrystallized grains and the relict grains when analysing the trade-off curve proposed by Cross et al. (2017). The average grain size of recrystallized grains (GOS < 1°) is 16 ± 7 μm whereas relict grains (GOS > 1°) have an average grain size of 25 ± 9 μm. Relict grains contain subgrains of an average size of 17 ± 7 μm (Fig. 4.9f). Similarly recrystallized grains in Fig. 4.10 have an average grain size of recrystallized grains of 12 ± 3 μm whereas relict grains 26 ± 4 μm.

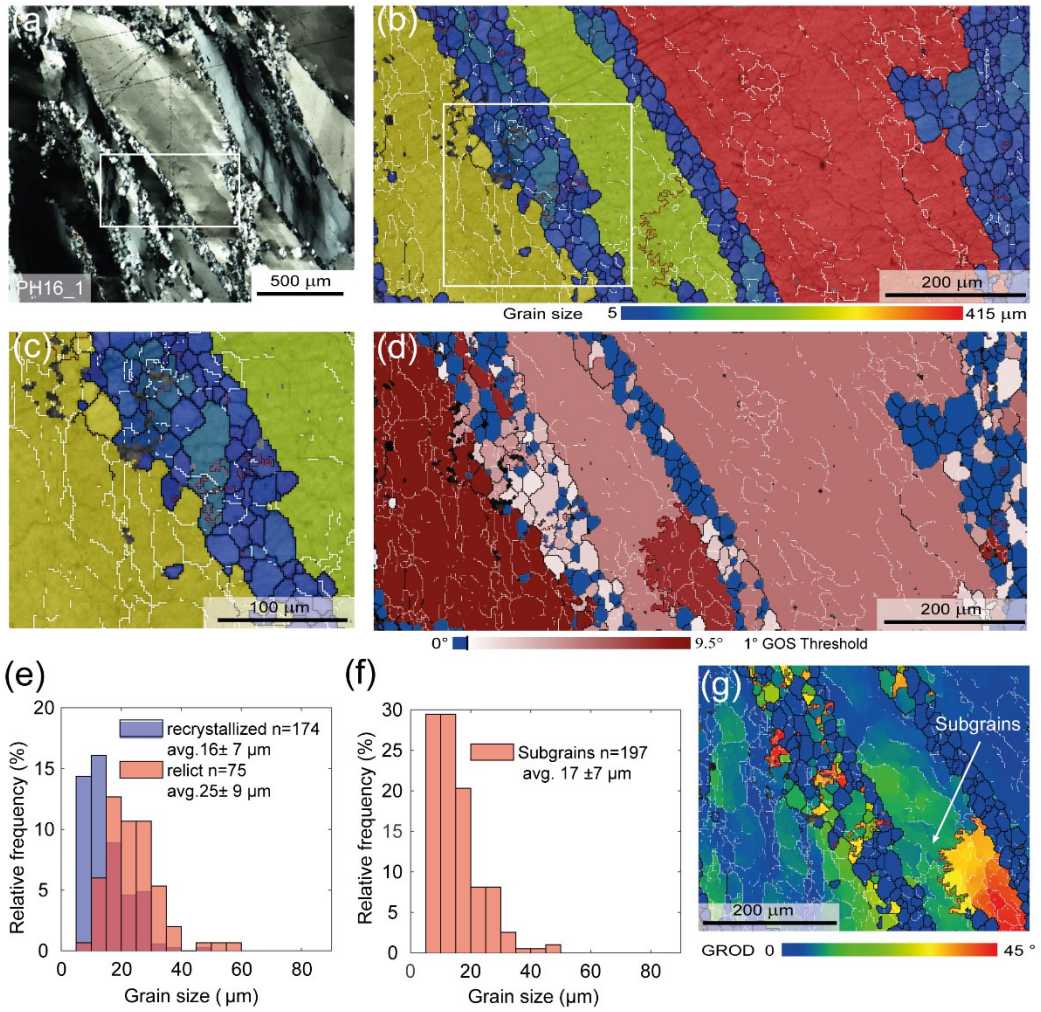

Figure 4.9 *EBSD data of quartz from the mylonitic fault core. In all the EBSD maps, black lines correspond to high-angle boundaries (misorientation > 10°), white lines to low-angle boundaries (misorientation between 2° and 10°), and red lines to Dauphiné twin boundaries (misorientation of 60° around the c-axis). (a) Quartz ribbons and intracrystalline bands of recrystallized grains. Cross polarized light. The box locates the EBSD map shown in (b-d, g). (b-c) Grain size map (diameter of the equivalent circle, µm), the higher magnification in (c) highlights the presence of subgrains in the large relict quartz grains and in the recrystallized grains. (d) Grain orientation spread (GOS) for each grain, coloured relative to the GOS threshold (black line) between recrystallized (blue) and relict (red) grains. (e) Histogram of grains size distribution of grains in the intercrystalline bands. (f) Histogram of subgrains size distribution of subgrains in the relict quartz from the intercrystalline bands (light red in (d)). (g) Grain Orientation Distribution maps (GROD) was used to estimate visually the subgrains size in the quartz ribbon*

Quartz grain hosting the intracrystalline band shows subgrains of 25-50 μm in size, which is comparable to the size of the coarser recrystallized grains observed in the intracrystalline bands (Fig. 4.9c). The size of the subgrains in the host quartz was estimated visually with the aid of Grain Relative Orientation Distribution maps (GROD, Fig. 4.9g).

In the recrystallized quartz layer (Fig. 4.10a), quartz grain shape ranges from equant to elongate parallel to the foliation, with grain size ranging from 5 to 87 μm (Figs. 4.10b, c). GOS analysis identified a threshold value of 1.56° to separate recrystallized- and relict grains (Fig. 4. 10d). Average grain size of the recrystallized grains is 18 ± 8 μm, while relict grains have an average size of 28 ± 11 μm (Fig. 4.10e).

The relict grains contain subgrains of an average size of 17 ± 7 μm (Figs. 4.10c, f). The crystallographic preferred orientation (CPO) of the c-axis of the relict grains and recrystallized grains forms a single girdle consistently inclined with the sinistral sense of shear of the sample (Fig. 4.10g). The EBSD-calibrated recrystallized grain size piezometer for quartz of Cross et al. (2017) was used to estimate the differential stresses during plastic flow in the mylonite. The estimated differential stress is 73-80 MPa for the average recrystallized grain size of 16-18 μm.

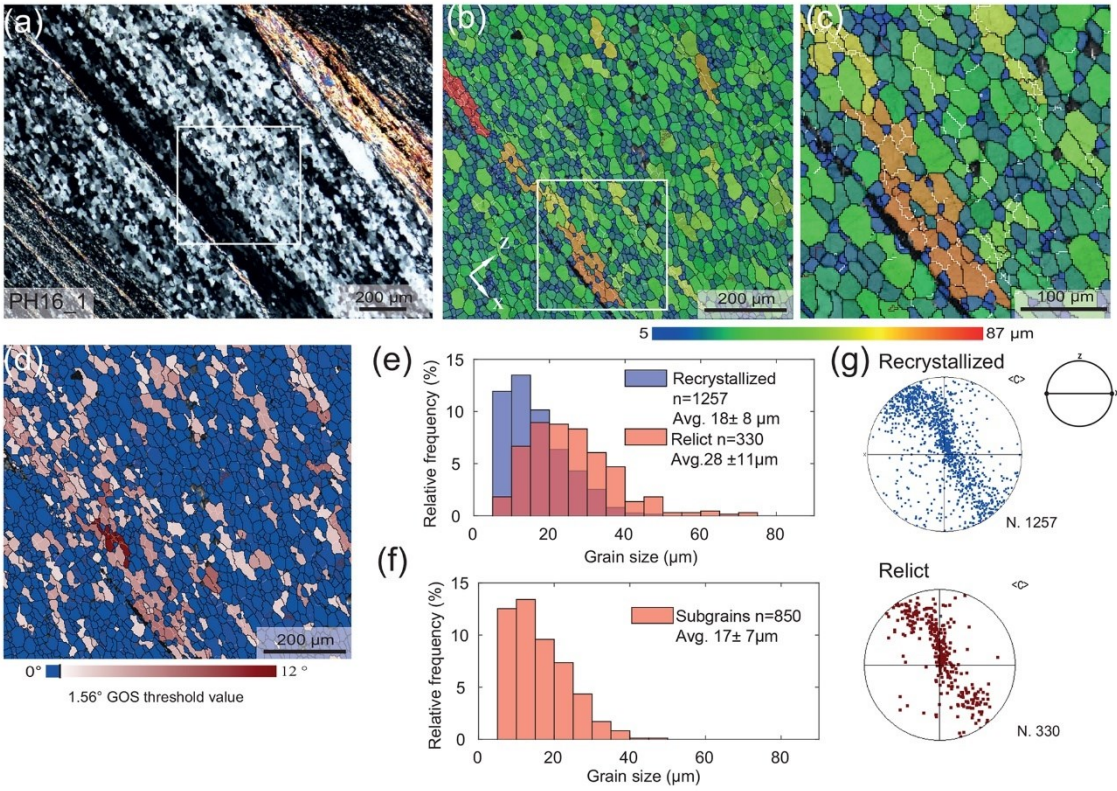

Figure 4.10 *EBSD data of quartz from a recrystallized ribbon in the mylonite. (a) Polycrystalline ribbons of recrystallized quartz grains elongated parallel to the mylonitic foliation (Fig. 5b). Cross-polarized light is used. The box indicates the EBSD maps shown in (b)–(d). Colour coding of the boundaries like in Fig. 6. (b, c) Grain size map (diameter of the equivalent circle in micrometres, µm) and detail (c) showing that the larger grains contain subgrains of the same size as the surrounding finer grains. (d) GOS map showing that the GOS values are mostly under the threshold, indicative of high degree of recrystallization. (e) Histogram of the grain size distribution for recrystallized and relict grains. (f) Histogram of the subgrain size distribution in the relict quartz grains identified in (d) and (e). (g) Pole figure of the c-axis orientation of recrystallized and relict grains, colour coded like the GOS map in (d) (equal area, lower-hemisphere projection).*

4.5.2 Veins parallel to the mylonitic foliation

The quartz vein parallel to the foliation shown in Fig. 4.6 (d,e) was analysed to identify possible evidence of crystal-plastic deformation and dynamic recrystallization. Grain shape varies from fibrous with elongation perpendicular to the vein wall, to more equant/less elongate. Grain boundaries of vein crystals are straight to lobate, the latter most commonly observed in association with fine recrystallized grains and bulges (< 15 μm in size) (Figs. 4.11 b, c). Irrespective of their shape, most of the grains contain low-angle boundaries and Dauphiné twins. The low-angle boundaries are typically arranged to define polygonal to slightly elongated domains of ~10 μm in size, comparable to that of the surrounding recrystallized grains in the mylonite (Fig 4.11c). Quartz in the mylonite flanking the vein shows fine grain size (< 20 μm), with only a small fraction of coarser grains (30-60 μm). GOS analysis indicates that dynamic recrystallization is pervasive. The mean recrystallized grain size is 10 ± 3 μm, and the relict average grain size is 20 ± 9 μm, with a GOS threshold value of 1.94° (Figs. 4.11d, e). Selected relict grains (size > 40 μm) in the mylonite contain subgrains with size between 5 to 25 μm range (Fig. 4.11f). Finer grains observed within the vein also present a GOS value below the threshold, which suggests they represent the recrystallized fraction in the quartz vein (Figs. 4.11c, f). In the vein quartz, GOS analysis indicates that the average subgrain size is 24 ± 7 μm, although the largest fraction of subgrains is smaller than 15 μm, i.e., similar in size to the recrystallized grains in the flanking mylonite and in the vein itself. The c-axis CPO of the recrystallized grains in the mylonite forms a single girdle synthetically inclined with the sinistral sense of shear (Fig. 4.11h). The c-axis CPO of recrystallized grains in the veins overlaps with the one of the relict grains (Fig.

4.11i). The differential stress estimated from the average recrystallized grain size in the mylonite (10 µm) is 106 MPa.

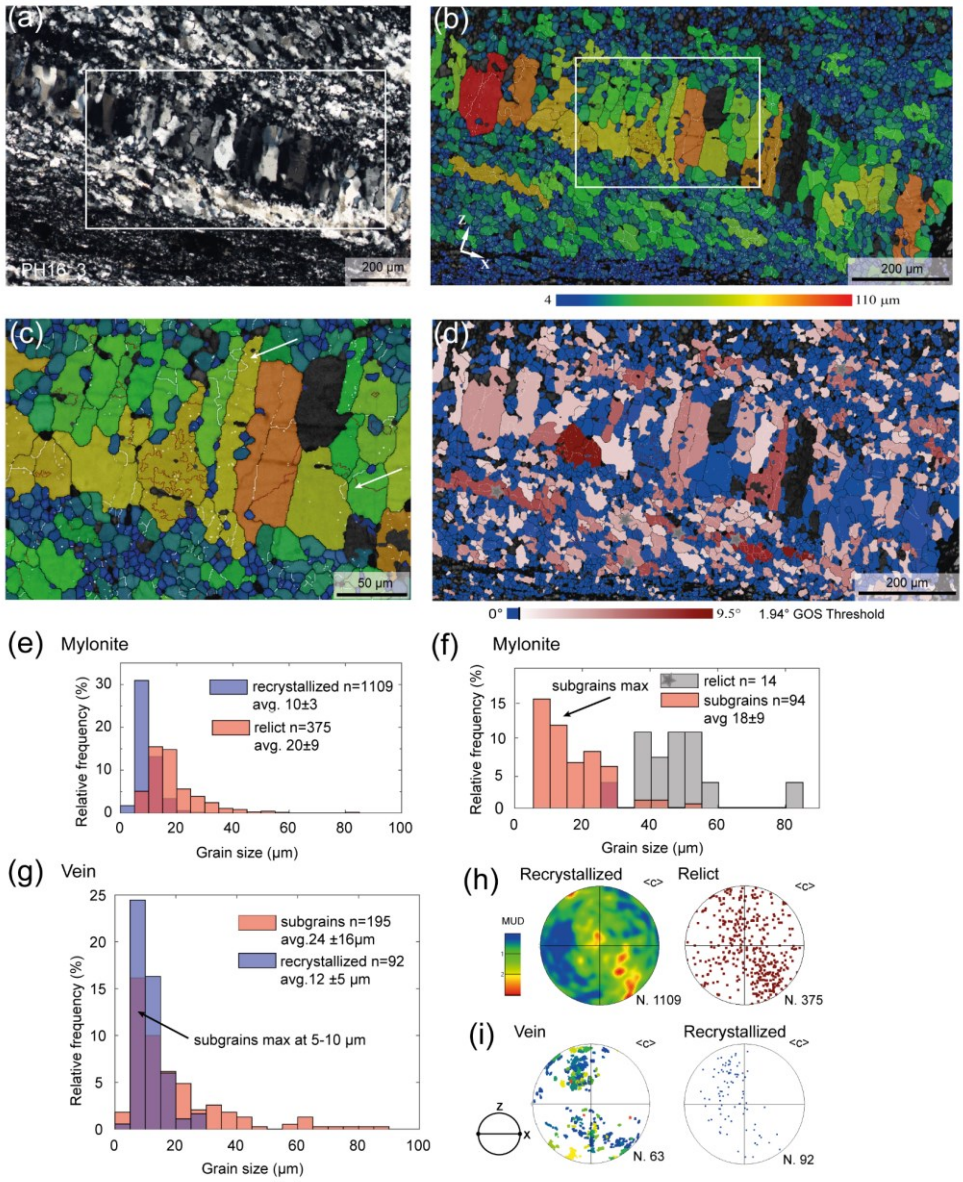

Figure 4.11 EBSD data of quartz from a foliation-parallel vein in the mylonite near the contact to the cataclasite. Colour coding of the boundaries like in Figure 4.9. (a) Quartz vein along the foliation. Quartz in the mylonite show a strong SPO consistent with the sinistral sense of shear of BFZ045. Cross polarized light. (b) Grain size map (diameter of the equivalent circle, µm. (c) Details of previous maps. Bulges and subgrains (white arrows) of comparable size of the bulges are evident within the vein quartz. (d) GOS map of quartz in the vein and of the surrounding mylonite. The GOS threshold value of 1.94° separates relict grains (red) from recrystallized grains (blue). Grey stars indicate relict grains plotted in (f) for subgrain size estimates. (e) Histogram of the grain size distribution in the mylonite, with relict and recrystallized grains separated with the GOS method. (f) Histogram of the subgrain size distribution (red) in

relict quartz of the mylonite (grey). (g) Histogram of the recrystallized grain size (red) and subgrains size (blue) distribution in the vein. (h-i) Pole figures of the c-axis orientation of the recrystallized and relic quartz in the mylonite (h) and in the veins (i). Equal area, lower hemisphere projection.

4.5.3 Cataclasite

We analysed a largely recrystallized quartz clast in the cataclasite from sample PH28_10 (Fig. 4.12a). The selected clast is rotated of less than 10° with respect to the adjacent mylonitic foliation. Quartz grain size in the clast ranges from 4 to 60 μm. The coarser grains are elongated parallel to the foliation, show bulges and fine recrystallized grains at their boundaries, and contain a high density of low-angle boundaries (Fig. 4.12b). The low-angle boundaries define small polygonal domains of a size comparable to the one of the recrystallized grains found at the grain boundaries (Fig. 4.12c). The GOS map in figure 9d identifies two grain size distributions, separated by a GOS threshold value of 3.23°. The recrystallized grains (average grain size: 8 ± 4 μm) form equigranular aggregates at the boundaries of the coarser (average grain size: 17 ± 10 μm) elongated relict grains. The c-axis CPO of the recrystallized grains and of the relict grains is the same, showing two maxima at an intermediate position between the centre of the pole figure and its periphery, and consistently inclined with the sinistral sense of shear of the sample (Fig. 4.12f). The differential stress estimated from the average recrystallized grain size in the clast (8 μm) is 123 MPa. Although the map has been acquired from a clast, these microstructures and recrystallized grain size are similar to those of the mylonite in the immediate vicinity (< 2 cm) of the brittle fault core.

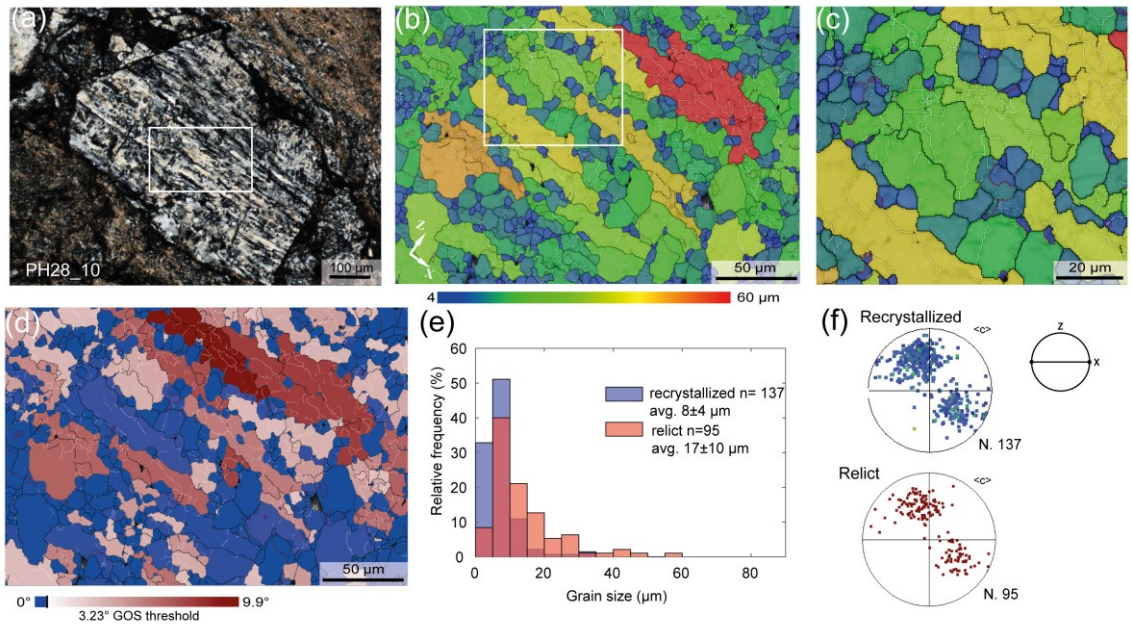

Figure 4.12 EBSD data of quartz from a clast in the cataclasite. Colour coding of the boundaries like in Figure 6. (a) The analysed quartz clast (Fig. 5f). The white rectangle locates the EBSD map shown in (b-d). (b-c) Grain size map (diameter of the equivalent circle, µm). The map highlights the presence of subgrains in the coarser elongated quartz grains with size comparable to the surrounding finer quartz. (d) GOS map. (e) Histogram of the grain size distribution of the recrystallized (blue) and relict (red) grains. (f) Pole figure of the c-axis orientation of recrystallized and relict grains. Equal area, lower hemisphere projection, color coded as GOS map.

4.6 Mineral chemistry, Raman spectroscopy, and pressure-temperature (P-T) conditions of deformation

Using Raman spectroscopy of carbonaceous material (RSCM), chlorite thermometry, and phengite barometry, P-T conditions of mylonitic deformation were calculated. Carbonaceous material was found in the host rock as grains and aggregates ranging in size from 50 to 200 μm (sample PH21 1, Fig. 4.13a) and as smaller grains (20-50 μm) in the mylonitic foliation (sample PH16 1-2, Fig. 4.13b), along chlorite and muscovite rich layers. A maximum temperature of 530° C ± 50° C for the carbonaceous material in the host rock (Fig. 4.14 a) (using the thermometer calibration for a laser wavelength of 514 nm, Beyssac et al. 2002), and a lower T of 440° C ± 50° C for the mylonite was obtained (Aoya et al., 2010, using the thermometer calibration for a laser wavelength of 532 nm; Fig. 4.14a).

The pressure during mylonitization was estimated using the Si-in-phengite geobarometer (Massonne and Schreyer, 1987). Representative compositions of white mica are listed in Table 1. White mica composition was measured for grains parallel to the foliation associated with neoblasts of K-feldspar, as the application of the Si-in-phengite geobarometer requires stability of K-feldspar (Figs. 4.13c, d). Structural formulae were calculated assuming 11 oxygens. The range of Si a.p.f.u. in the probed white mica grains is 3.12 –3.16. This compositional range indicates a pressure of 2-4 kbar for the mylonitization (Fig. 4.14b), considering the average temperature of 440° C derived for the mylonite with the graphite thermometry.

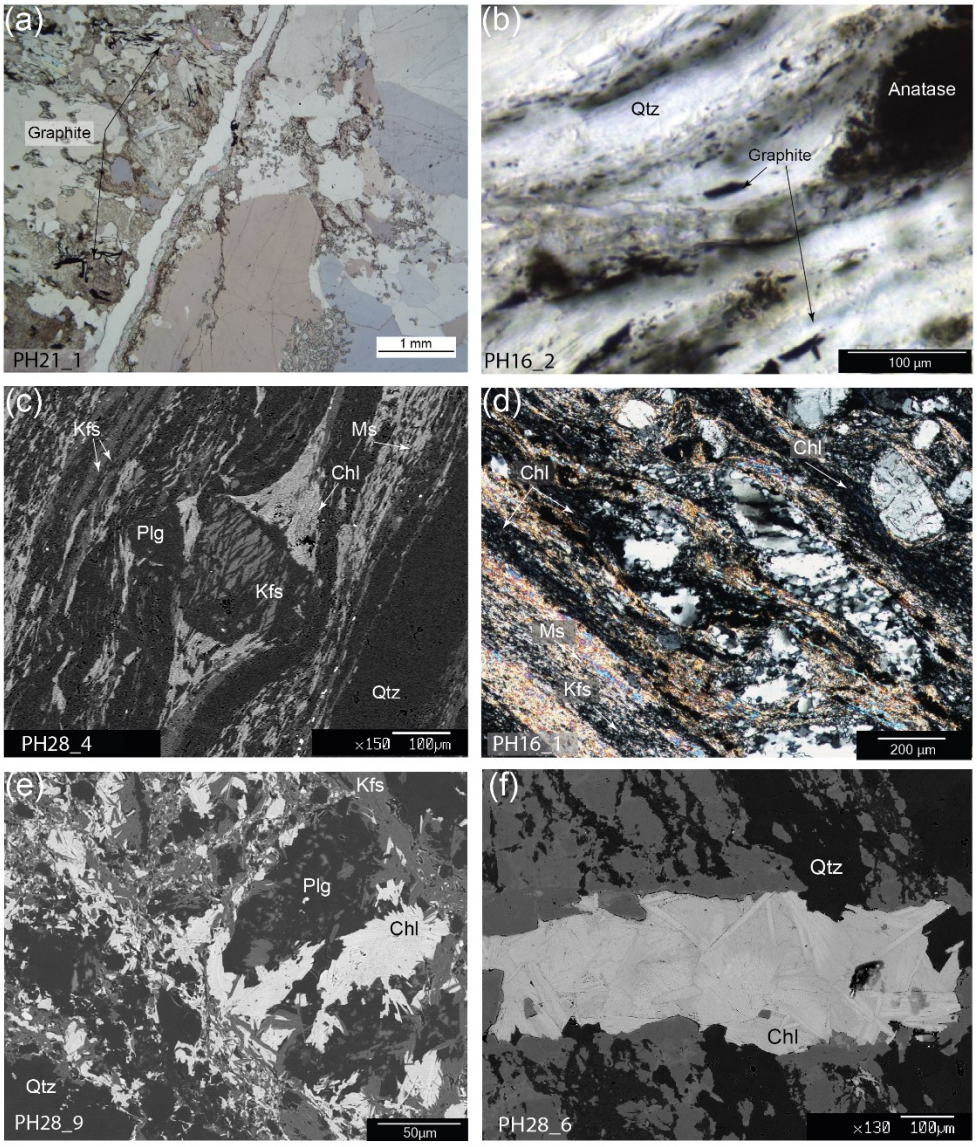

Figure 4.13 Light microscopy and SEM backscattered electron (BSE) images of characteristic microstructural domains and mineral assemblages used for geothermobarometry estimates. (a) Graphite flakes in association with radiate chlorite in the host rock. Plane-polarized light is used. (b) Detail of graphite grains along the mylonitic foliation of BFZ045. Plane-polarized light is used. (c) Chlorite in pressure shadows around a K-feldspar porphyroclast in the mylonite. White mica and a fine-grained recrystallized K-feldspar assemblage is common along the foliation. (d) Light microscope image of a microstructure similar to (c) (cross-polarized light). (e–f) SEM BSE images of radiate chlorite used for chlorite thermometry in the cataclasite matrix (e) and in a vein cutting the mylonitic foliation (f). The trace of the mylonitic foliation in (f) is oriented ca. NW–SE.

.

Chlorite composition was determined for i) chlorite grains intergrown with quartz and muscovite in the strain shadows around feldspar porphyroclasts in the mylonite (Fig.

4.13c, d), ii) chlorites flakes aggregate in the cataclasite quartz matrix (Fig. 4.13e), and iii) radiate chlorites filling veins at high angle to the mylonitic foliation (Fig. 4.13f).

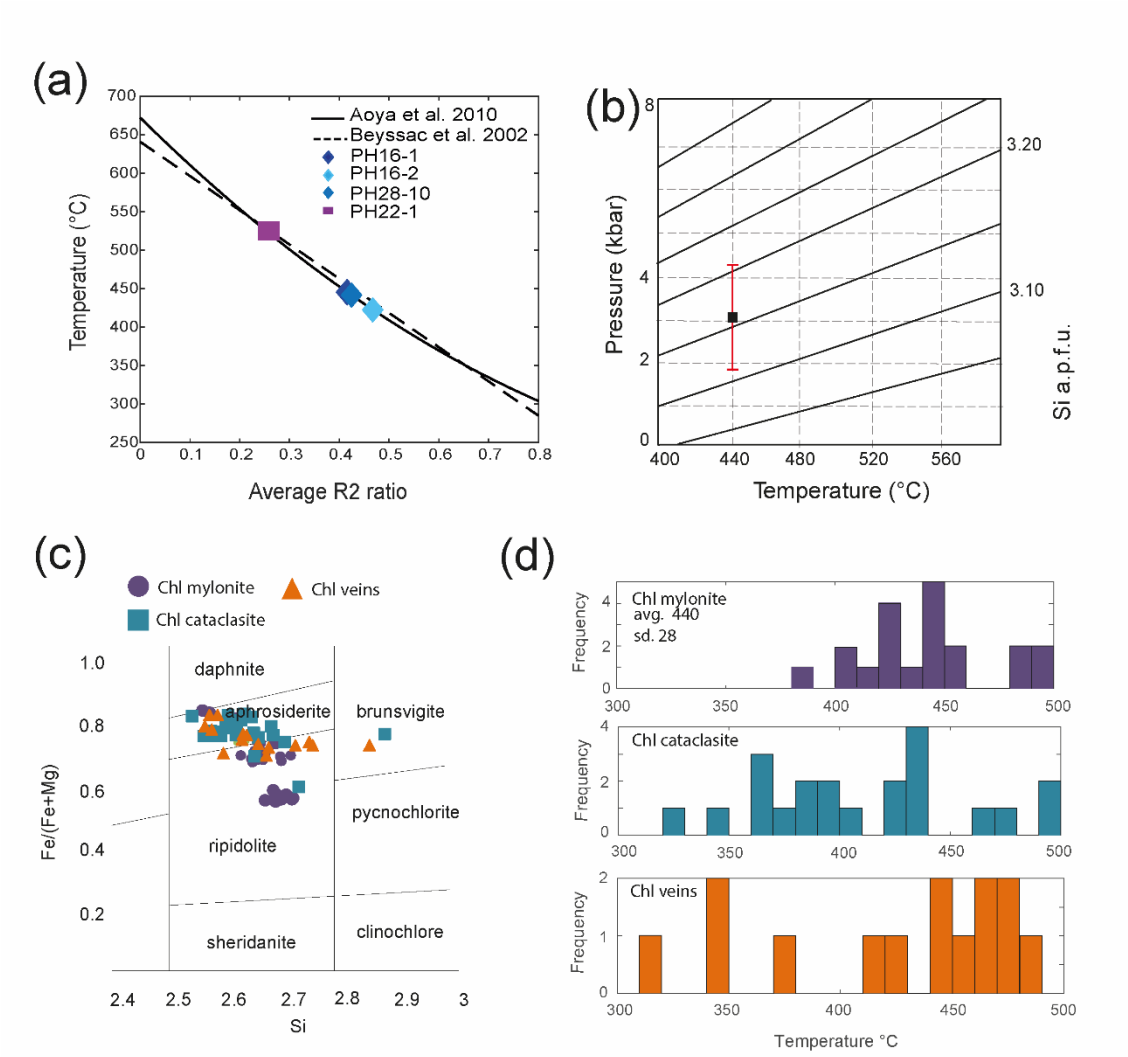

Figure 4.14 Results of P-T estimates. (a) Carbonaceous material Raman geothermometer. Average R2 ratio (refer to text for explanation) for graphite rich mylonitic and host rock samples was measured to derive a T estimate using the method of Beyssac et al. (2002) and Aoya et al. (2010). (b) Estimated P of mylonitization using the Si-in-phengite barometer (Massonne and Schreyer, 1987) for the average T of 440° C obtained with the carbonaceous material Raman thermometry. Red line show the total spread of the Si values obtained. Black square show the average result. (c) Chlorite compositional diagram based on Hey (1954). (d) Chlorite formation temperature estimated for mylonitic foliation, veins and cataclasite using the method of Lanari et al. (2014).

Chlorites along the mylonitic foliation have Si content (~2.60 - 2.70 apfu), Al between 2.74-2.88 apfu, and are moderately Fe-rich with a XFe (XFe=Fe/(Fe+Mg)) between

0.62 and 0.82. Chlorites in the mylonitic sample from PH_16 have a more narrow range of XFe, between 0.57 and 0.73. In the cataclasite chlorites Si content range between 2.53-2.772 apfu, and Al have a wider range of 2.61-2.94 apfu. The cataclastic chlorite is richer in Fe compared to the mylonite, with a XFe range between 0.71-0.85. The radial chlorite filling the veins cutting the mylonite has Si content between 2.51 and 2.780 apfu, Al between 2.74 and 3.00 apfu, and XFe vary between 0.69 and 0.81. In general, BFZ045 chlorites have an aphrosiderite-ripidolite composition and the microprobe results show that the composition of distinct chlorite generations is similar (Fig. 4.14c). The CHL(2) semi-empirical thermometer of Lanari et al. (2014) was applied to each EMPA analysis of chlorite with Si < 3 apfu and (Na + K + Ca) < 0.1apfu. FeO was used as Fe total, and aH2O = 1 and aSiO2 = 1 were assumed. The estimated temperature for the mylonite ranges from ~380° C to 500° C (limit of the used thermometer) for an assumed P of 3.5 kbar (Fig. 4.14d), with a temperature variation of 10° C every 0.5 kbar increment. Temperatures estimated for the cataclasite matrix and for the radiated chlorite in the veins have a larger range (~300-500° C, Fig 4.14d). Compositions yielding T lower than 400° C are more frequent, especially in the cataclasite, however no clear relationship could be discerned between temperature and microstructural position of the chlorites.

Sample name	PH28_7a	PH28_7b-1	PH28_5a	PH28_5b-1	PH28_5c	PH28_5d	PH28_9e	PH28_10-6
N. measurament	n=5	n=5	n=15	n=18	n=12	n=16	n=18	n=10
Chemical composition (wt%)								
SiO2	48.280	48.080	48.210	48.410	48.330	48.770	47.970	47.660
TiO2	0.093	0.098	0.124	0.099	0.104	0.074	0.043	0.136
Al2O3	33.910	33.900	33.860	34.520	34.590	34.680	35.690	34.910
Cr2O3	0.011	0.000	0.000	0.017	0.000	0.000	0.037	0.000
Fe2O3	0.000	0.000	0.000	0.000	0.000	0.000	0.000	
FeO	2.540	2.430	2.710	2.080	2.060	1.940	3.010	2.730
MnO	0.060	0.001	0.052	0.000	0.000	0.005	0.078	0.028
MgO	1.563	1.383	1.446	1.411	1.384	1.360	0.546	1.415
CaO	0.017	0.005	0.000	0.032	0.010	0.033	0.015	0.054
Na2O	0.091	0.136	0.132	0.163	0.138	0.116	0.126	0.201
K2O	11.080	11.120	11.090	11.180	11.030	11.230	9.430	10.690
NiO	0.000	0.036	0.006	0.000	0.000	0.013	0.000	0.036
Total	97.645	97.189	97.630	97.912	97.646	98.221	96.944	97.859
Structural formula on the basis of 11 O								
SiO2	3.15	3.16	3.15	3.15	3.15	3.16	3.13	3.11
TiO2	0.00	0.00	0.01	0.00	0.01	0.00	0.00	0.01
Al2O3	2.61	2.62	2.61	2.65	2.65	2.65	2.74	2.68
Cr2O3	0.00	0.00	0.00	0.00	0.00	0.00	0.00	0.00
Fe2O3	0.00	0.00	0.00	0.00	0.00	0.00	0.00	0.00
FeO	0.14	0.13	0.15	0.11	0.11	0.11	0.16	0.15
MnO	0.00	0.00	0.00	0.00	0.00	0.00	0.00	0.00
MgO	0.15	0.14	0.14	0.14	0.13	0.13	0.05	0.14
CaO	0.00	0.00	0.00	0.00	0.00	0.00	0.00	0.00
Na2O	0.01	0.02	0.02	0.02	0.02	0.01	0.02	0.03
K2O	0.92	0.93	0.93	0.93	0.92	0.93	0.78	0.89
NiO	0.00	0.00	0.00	0.00	0.00	0.00	0.00	0.00
H2O	0.00	0.00	0.00	0.00	0.00	0.00	0.00	0.00

Table 4-1Representative compositions of muscovite from the BFZ045 mylonite

Fault rock	Mylonite				Cataclasite				Veins			
Sample name	PH16-2_2	PH16-2_5	PH28-10_3	PH28-10_15	PH28-9_5	PH28-9_7	PH28-9_10	PH28-9_19	PH28-6_6	PH28-6_9	PH28-6_11	PH28-6_13
Chemical composition (wt%)												
SiO2	25.040	25.820	24.790	24.790	23.600	23.800	23.290	24.170	25.470	23.930	23.290	24.070
TiO2	0.034	0.034	0.078	0.060	0.031	0.115	0.050	0.010	0.059	0.049	0.004	0.000
Al2O3	21.600	22.290	21.890	22.140	22.150	22.420	22.440	21.990	20.620	21.860	22.690	22.120
FeO	28.700	29.930	35.830	34.600	38.530	39.650	39.150	34.360	37.260	37.940	39.670	37.650
MnO	0.173	0.349	0.918	0.858	0.846	0.810	0.793	0.675	1.201	0.596	0.937	1.430
MgO	12.010	11.740	7.570	8.430	4.810	3.780	3.900	7.730	6.980	5.810	3.910	5.730
CaO	0.047	0.061	0.121	0.056	0.008	0.001	0.003	0.000	0.021	0.006	0.005	0.044
Na2O	0.014	0.055	0.010	0.000	0.000	0.046	0.036	0.011	0.000	0.000	0.015	0.000
K2O	0.064	0.047	0.020	0.040	0.021	0.000	0.080	0.087	0.008	0.000	0.005	0.008
Total	87.682	90.364	91.236	90.973	90.049	90.655	89.742	89.033	91.620	90.190	90.525	91.081
Structural formulae on the basis of 14 O												
Si	2.687	2.695	2.658	2.647	2.610	2.624	2.595	2.641	2.741	2.628	2.577	2.621
Ti	0.003	0.003	0.006	0.005	0.003	0.010	0.004	0.001	0.005	0.004	0.000	0.000
Al	2.731	2.742	2.766	2.786	2.887	2.913	2.947	2.832	2.615	2.829	2.959	2.839
Fe(3+)	0.000	0.000	0.000	0.000	0.000	0.000	0.000	0.000	0.000	0.000	0.000	0.000
Fe(2+)	2.575	2.613	3.213	3.089	3.563	3.656	3.648	3.140	3.353	3.485	3.671	3.429
Mn	0.016	0.031	0.083	0.078	0.079	0.076	0.075	0.063	0.110	0.055	0.088	0.132
Mg	1.921	1.827	1.210	1.342	0.793	0.621	0.648	1.259	1.120	0.951	0.645	0.930
Ca	0.005	0.007	0.014	0.006	0.001	0.000	0.000	0.000	0.003	0.001	0.001	0.005
Na	0.003	0.011	0.002	0.000	0.000	0.010	0.008	0.002	0.000	0.000	0.003	0.000
K	0.009	0.006	0.003	0.005	0.003	0.000	0.011	0.012	0.001	0.000	0.001	0.001
XFe= Fe/(Fe+Mg)	0.57	0.59	0.73	0.70	0.82	0.85	0.85	0.71	0.75	0.79	0.85	0.79

Table 4-2 Representative compositions of chlorite from different domains of BFZ045

4.7 Discussion

Our observations constrain the details of the structure and the deformation history of BFZ045. In particular, the microstructures of fault rocks indicate a sequence of deformation events where ductile deformation (mylonitization) was punctuated by brittle deformation (veining), and eventually culminated in the formation of the brittle, cataclastic fault core. We interpret this sequence to result from the evolving stress history and possible fluid pressure variations during the overall ductile-to-brittle deformation history of the strike-slip BFZ045 fault.

4.7.1 The sequence of deformation events in BFZ045: ductile-brittle deformation history

Our microstructural observations are consistent with the general conclusion that brittle deformation along BFZ045 exploited a ductile (mylonitic) precursor (Nordbäck and Mattila al., 2018; Skyttä and Torvela, 2018). Veins, cataclasites and pseudotachylytes are localised along the mylonitic fabric of BFZ045, and only minor evidence of brittle deformation (mostly in the form of fractures filled by chlorite) is present outside of the mylonitic fault core (Figs. 4.3a, 4.5a). The first stage of deformation of BFZ045 is represented by the development of a localised N-S trending mylonitic foliation (Figs. 4.3, 4.5a-c). Mylonitic creep was punctuated by transient brittle events, with the opening of extensional fractures along the mylonitic foliation filled by quartz veins (Figs. 4.5 d, e). Veining was again followed by mylonitic deformation, as indicated by dislocation creep and dynamic recrystallization microstructures of quartz in the veins. Mylonite and veins were then overprinted by brittle deformation that formed cm- thick cataclasites (Figs. 4.5a-c) and a < 0.5 cm thick pseudotachylyte (Fig. 4.6 d) that,

together, form the brittle fault core of BFZ045. Cataclasites and pseudotachylytes were not overprinted by mylonitic creep, which might indicate that they formed under condition favourable to predominantly brittle deformation along BFZ045.

The observed parallelism between stretching lineation in the mylonite and chlorite slicken lines in the cataclasites suggest that the ductile-brittle deformation history of BFZ045 occurred under a prolonged strike-slip regime with sinistral kinematics (Figs. 4.3b,c). This conclusion is consistent with the model of the brittle evolution of SW Finland proposed by Mattila and Viola (2014), which attributes the sinistral kinematics of NNW-SSE trending subvertical faults to the ductile-brittle transition stage of the basement at 1.75 Ga (Stage 1 of deformation in Mattila and Viola, 2014). BFZ045 experienced later reactivations during the prolonged brittle history of the SW Finland basement, as indicated by calcite veins cutting the brittle fault core and by (rare) slicken lines with dextral kinematics observed in the underground exposures (Aaltonen et al. 2016). Local dextral kinematics along BFZ045 is potentially consistent with the Stage 2 of deformation of Mattila and Viola (2014) at 1.7-1.6 Ga. These later features, however, are not discussed further in this paper as they are subordinate to and did not obliterate the earlier history.

4.7.2 Deformation mechanisms and stress history during mylonitic creep of BFZ045

Microstructural observations show that ductile deformation of the mylonite BFZ045 was accommodated in quartz by dislocation creep, while feldspars experienced dominantly brittle behaviour with only limited neo crystallization in pressure shadows (Figs. 4.10c). Given the lack of crystal plastic deformation and recovery features in the interior of feldspar porphyroclasts, we interpret the neo crystallization in pressure

shadows as a possible indication of dissolution-precipitation, which has been commonly reported in feldspars deforming at mid-crustal conditions (Fitz Gerald and Stünitz 1993; Menegon et al. 2008; Eberlei et al., 2014; Torgersen et al., 2015; Giuntoli et al., 2018; Hentschel et al., 2019).

Quartz recrystallization microstructures (bulges at grain boundaries and within intracrystalline bands, and core and mantle microstructures with subgrains of comparable size to that of the recrystallized grains; Figs. 4.4, 4.5) suggest that bulging and subgrain rotation were the dominant recrystallization mechanisms (Hirth and Tullis, 1992; Stipp and Kunze, 2008). The average recrystallized grain size of quartz ranges between 8 and 18 μm, which falls within the < 40 μm size value representative of bulging as dominant recrystallization mechanism (defined as slow grain boundary migration coupled to localised subgrain rotation at the mantle of the host grain (Stipp et al., 2010). In all the studied samples, GOS analysis distinguished two quartz grain size populations, in which the coarser (relict) grain size contains subgrains of size comparable to the average size of the finer recrystallized grains (Figs. 4.7-4.9). The CPO of relict and recrystallized grains is the same, and this is consistent with the host-controlled development of a CPO during subgrain rotation recrystallization (e.g., Stünitz et al. 2003).

A key observation in the BFZ045 mylonite is the decrease in recrystallized grain size of quartz from the shear zone boundary (16-18 μm) towards the centre (8-12 μm; Fig.4.7-4.9). The coarser (16-18 μm) grain size is the most representative of the partially- (Fig. 4.7) and of the nearly completely (Fig. 4.8) recrystallized quartz ribbons in the BFZ045 mylonite at distances ≥ 4 cm from the brittle fault core, and it also occurs as relict grain size in quartz clasts embedded in the cataclasite, where it is overprinted by the finer (8-12 μm) recrystallized grains (Fig. 4.10). We interpret this overprint and the overall decrease in recrystallized grain size to reflect a progressive increase in stress and strain

rate towards the shear zone centre during mylonitic creep (Kidder et al. 2016). Throughout the samples the CPO of recrystallized quartz is consistently inclined with a sinistral sense of shear (Fig. 4.9-4.12); this is interpreted as evidence that they developed under constant kinematic conditions in BFZ045.

Relict quartz grains of 25-28 µm in size are associated with the coarser (16-18 µm) grain size (Figs. 4.10-4.11), and un-recrystallized portions of quartz contain subgrains of similar size (≥ 25 µm, Figs. 4.10b-d). We consider that the 25-28 µm grain size population might represent an early, dynamic recrystallization event within BFZ045, which was later overprinted by recrystallization occurring under progressively increasing differential stress.

Deformation and stress history of BFZ045 can be summarised in various stages. After the regional metamorphic peak and migmatite formation (i.e. 660-700° C, 3.7-4.2 kbar; Tuisku and Kärki, 2010), the basement of Olkiluoto was affected by different stages of ductile deformation (D2-D4, Aaltonen et al., 2010) under a metamorphic retrograde path toward greenschist facies conditions. The progressive change in P-T condition was favourable to the mobilization and subsequent recrystallization of carbonaceous material (e.g. Kirillova et al., 2017). We thus interpret the estimated metamorphic temperature of 530° C ± 50° C in the host rock as the temperature of remobilization of carbonaceous material during retrograde metamorphism that culminated in the D4 deformation stage. During the final stage of D4 a localised N-S trending mylonitic foliation developed in the migmatites (Fig. 4.15a). Mylonitic creep took place under differential stresses increasing from ~ 54 to ~ 80 MPa, as determined from the recrystallized grain size of 16-18 µm overprinting grains of 25-28 µm. Foliation-parallel quartz veins crystallized transiently along the mylonitic foliation (Fig. 4.15b) and were overprinted by crystal plastic deformation and dynamic recrystallization under progressively higher stress (80-120 MPa, Figs. 4.11, 4.15c) during strain localisation

towards the centre of the shear zone. We are aware of the uncertainties and limitations of the palaeopiezometric calibrations, and our estimated flow stresses must be taken with care. However, the similarity between subgrain- and grain size, as well as the consistent sinistral asymmetry of the quartz c-axis CPO of relict and recrystallized grains in all the maps support that dynamic recrystallization occurred during the sinistral strike-slip movement of BFZ045 under progressively increasing differential stresses.

We estimate that mylonitization of BFZ045 (Fig. 4.15a-c) occurred at ~450° C and 3.5 kbar, consistent with the retrograde greenschist facies conditions attributed to the final stages of D4 deformation in the SW Finland basement at 1.81-1.77 Ga (Lahtinen et al., 2005; Mänttäri et al., 2010; Skyttä and Torvela, 2018). Considering an average crustal density of 2.7 g/cm3, the depth of mylonitic deformation and of transient veining in BFZ045 corresponds to approximately 13 km.

The mylonite and quartz veins were eventually overprinted by more pervasive brittle deformation that formed chlorite veins, cm-thick cataclasites and a < 0.5 cm thick pseudotachylyte that, together, form the brittle fault core of BFZ045 (Fig. 4.15 d). We attempted to estimate the temperature of chlorite veins cutting the mylonitic foliation and of chlorite in the cataclastic matrix (Fig. 4.11), but we obtained a wide temperature range of ~300-500° C that is unable to constrain the precise T of the final brittle deformation event(s). Although the conditions of formation of cataclasites and pseudotachylytes cannot be tightly constrained, it is interesting to note that the T estimates from the chlorite in the veins are generally higher than 400° C. This suggests that chlorite veining occurred early in the deformation history of BFZ045 (i.e. at T ≥ 400° C) under overall ductile conditions, as also supported by the precipitation of chlorite + quartz aggregates in microveins and in strain shadows (Fig. 4.5e). This is consistent with the results of Marchesini et al. (2019), who estimated a temperature of at

least 350° C for the early stages of deformation and emplacement of quartz-chlorite veins along the dextral fault zone BFZ300 (conjugate to BFZ045).

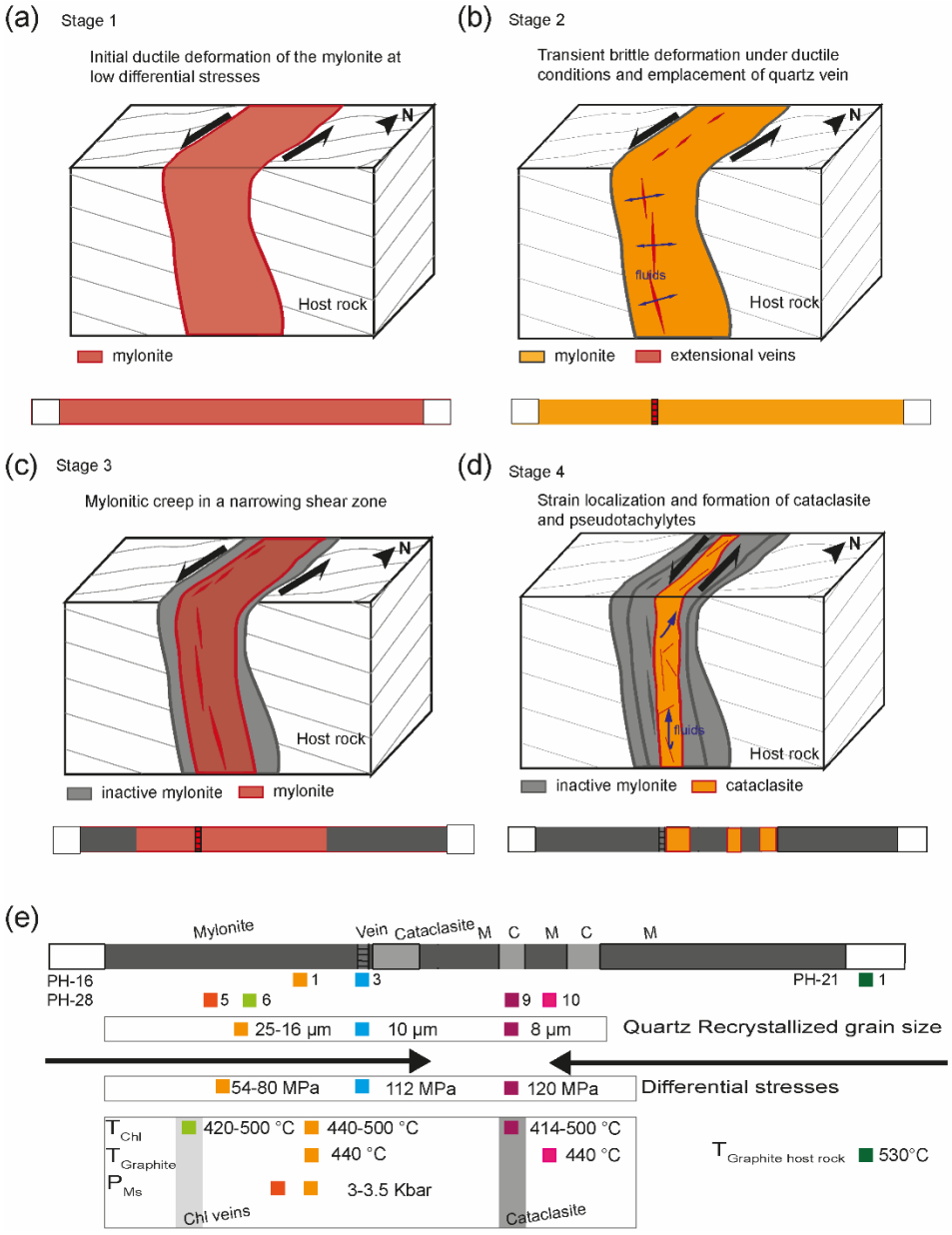

Figure 4.15 Schematic representation of the microstructural evolution of BFZ045. (a–d) Grey lines: traces of metamorphic foliation in the host rock. In the schematic fault scheme evolution, red displays the active deformation process, grey represents the inactive deformation processes, and orange suggests a transition in the deformation. (a) The development of mylonite was punctuated by the emplacement of quartz vein (b). (c) Ductile deformation localized toward the centre of the mylonitic fault core in an overall narrowing shear zone, and it was followed by formation of cataclasite, chlorite veins, and pseudotachylyte (d). (e) Schematic summary of the quartz recrystallized grain size, differential stresses, and P –T conditions of deformation for BFZ045 derived in the present study, in relation to the fault core geometry.

4.7.3 Conceptual model of the fault slip behaviour of BFZ045 at the base of the seismogenic zone

Using a λ-σ failure mode diagram (Cox, 2010), we propose a conceptual model of the structural evolution of BFZ045 (Fig.4.16). Strain rates during mylonitc creep were estimated using the dislocation creep flow laws of quartz of Hirth et al. (2001). Parameters and assumptions used for the calculation of the strain rates and of the λ-σ failure envelopes are listed in Table 3.

Parameter	Value	Reference/source	Notes
vertical stress σ2	350 MPa	P estimate	lithostatic load during deformation for Andersonian type fault in a strike-slip regime
strain rate	stage 1 (50MPa) 4.3×10^{-13} s^{-1} stage 3 (80MPa) 1.1×10^{-12} s^{-1} stage 3 (120 MPa) 6.9×10^{-12} s^{-1}	Hirth et al. (2001) Wither's fugacity calculator (Pitzer and Sterner, 1994)	$\dot{\varepsilon} = A\sigma^n f_{H2O}^m \exp(-Q/RT)$ A an empirical constant, σ the differential stress, n the stress exponent, f_{H2O} the water fugacity (calculated at 350 MPa using Wither's fugacity calculator), m the water fugacity exponent, Q the activation energy, R the gas constant, and T the temperature
fluid pressure conditions	> 210 MPa	Marchesini et al. (2019)	
friction coefficient (μ)	0.6	Sibson (1985)	common value for granitoids
cohesive strength	26 MPa	Aaltonen et al.(2010)	data from tensile strength measurements of granitic gneisses
tensile strength	13 MPa	Aaltonen et al.(2010)	

Table 4-3 Parameters used for λ -σ failure mode diagrams

According to the failure envelope, differential stresses < 80 MPa are necessary for extensional- and hybrid fractures to occur. In our model, this stage of fault evolution is represented by the ~ 54 MPa creep recorded by quartz grain- and subgrain size of 25-28 μm (Figs. 4.7b-d). The failure envelope also shows that extensional failure and vein formation required transient high fluid pressure reaching lithostatic values (λ = 1; Fig. 4.16b, stage 2). Although the overall geometric stress conditions during ductile deformation of BFZ045 are expected to generate en-echelon vein systems oblique to the mylonitic foliation, the foliation-parallel veins are consistent with mode I opening mode due to hydrofracturing. A regional rotation of the stress field appears unlikely, given the

constant orientation of the stretching lineation and slickenlines in the core samples, and the consistent asymmetry of the pre- and post-vein quartz c-axis CPO (Figs. 4.7-4.9). Thus, a transient reorientation of the stress field in the fault zone must be invoked to explain the switch from viscous creep to mode I fracturing along the mylonite foliation.

Following veining, there was a drop in fluid pressure (e.g., Sibson, 1989, 1993; Cox 1995) and a return to mylonitic creep under increasingly greater stress and strain rate conditions (Fig. 4.16c, stage 3). The failure mode diagram shows that for pore fluid pressure factors greater than 0.8, these increased stresses are likely to result in brittle shear failure mode of the fault. The cataclasite and pseudotachylytes in the brittle fault core are most likely the result of BFZ045 deformation under increasing differential loads and fluid pressure throughout the BDTZ. The time span between high strain rate mylonitic creep and the creation of the brittle fault core, however, is unclear, as are the precise P-T conditions of cataclasites and pseudotachylytes. As a result, the stage 3 model remains rather speculative.

The rise in stress towards the shear zone centre (Fig. 4.16c) may represent the rheological development of a narrower shear zone with exhumation under progressively decreasing T from the ductile to the brittle crust (e.g., Kohlstedt et al., 1995; Behr and Platt, 2011). External stress loading from seismic faulting in the underlying upper crust might also be responsible (e.g., Küster and Stöckhert, 1998; Treppman and Stöckhert, 2003; Treppman et al., 2017; Treppman and Seybold, 2019). Both hypotheses are equally valid in explaining the data and are not mutually exclusive. Due to the constraints of our P-T estimations, is not possible to differentiate between the two choices. The presence of pseudotachylytes along the BFZ045 fault core, on the other hand, suggests that the fault was capable of producing earthquakes, and the seismogenic behaviour of other faults in the Olkiluoto basement has previously been examined

(Marchesini et al., 2019 and references therein). This shows that transitory seismic stress may have caused the localised rise in creep rate during BFZ045 mylonitization.

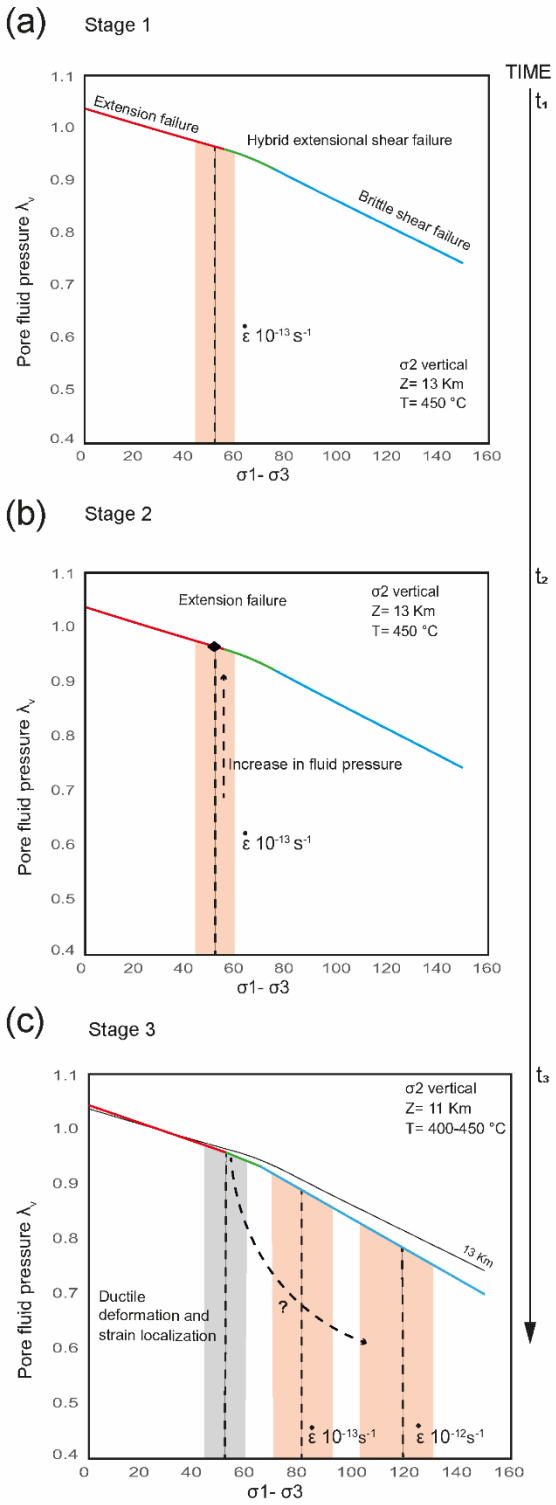

Figure 4.16 Conceptual model of the temporal and mechanical evolution of the BFZ045 fault zone (see text for more details). BFZ045 was characterized by (a) the development of mylonite creeping at ca. 10–13 s−1, followed by (b) a transient increase in fluid

pressure responsible for the emplacement of quartz veins. Ductile deformation then continued under increasing differential stress and strain rates (c).

4.8 Conclusions

This study shows that deformation microstructures can be used to evaluate the stress history of a shear zone deforming across the brittle-ductile transition in the continental crust, and to reconstruct the cyclical brittle-ductile deformation history of fault zones. The fault zone BFZ045 exploited a mylonitic precursor in the Paleoproterozoic basement in SW Finland and records transient brittle deformation in the form of syn-kinematic quartz veins emplaced during ongoing mylonitic creep at ~ 450° C and 3.5 kbar, in response to transiently high fluid pressure. Mylonitic deformation continued after vein emplacement, as evidenced by the dynamic recrystallization of the vein quartz. Mylonitic creep occurred under progressively increasing differential stress towards the shear zone centre in an overall narrowing shear zone. Mylonitic deformation at the shear zone centre records peak stress conditions of around 120 MPa and was followed by brittle deformation that generated cataclasites and minor pseudotachylytes in the fault core.

The constraints derived from microstructural analysis shaped the proposed conceptual model of the evolution of BFZ045 slip behaviour, which highlights the significant role of transiently sub-lithostatic fluid pressure in triggering vein emplacement during ongoing mylonitic deformation, as well as of the progressive increase in stress and strain rate during viscous creep towards peak conditions reached at the BDTZ in the Fennoscandian Shield. This study shows that microstructural studies leading to the acquisition of independent constraints offer the potential to reconstruct in detail the evolutionary history of fault zones that experienced a transition in deformation mode at

the BDTZ. In addition to deriving a conceptual model of varying fault slip behaviours at the BDTZ, the methods and the results of this work complement and expand thorough site characterization studies of deep geological disposal facilities.

5 Micro-porosity characterization and distribution across BFZ045 fault rocks

5.1 Introduction

Investigating the distribution and origin of porosity in exhumed shear zones and faults is critical to understand the interaction between fluid migration and rock deformation. In fault rocks, porosity variation is closely tied to the mechanics, structure, and development of the fault (Gratier and Gueydan, 2007; Faulkner et al., 2010). Fracturing in crystalline rocks can enhance permeability and, as a result, affects rates of fluid propagation (e.g. Caine et al., 1996; Micklethwaite and Cox, 2004). Presence of chemically active fluids within the fracture network can decrease the porosity by mineral precipitation (Sibson, 1987; Nishimoto & Yoshida, 2010). Moreover, pressure solution processes and gouge compaction in brittle faults result in porosity reductions (Renard et al., 2000). Porosity reduction related, for example, to pressure solution can lead to an increase of pore fluid pressures within fault cores (Gratier et al., 2003). Variation of fluid pressure can prompt brittle failure under ductile condition, consequently promoting cyclicity in the fault deformation behaviour (Sibson, 1990).

Extensive literature exists on porosity-forming mechanisms in different fault rock types and in conjunction with different mineral reactions, (e.g. Tullborg and Larson, 2006; Voorn et al., 2015; Staněk and Géraud, 2019; Wirth et al., 2022) especially in natural shear zones (Géraud et al., 1995; Mancktelow et al., 1998) and under different experimental conditions (e.g. Violay et al., 2017; Xing et al., 2018). Model of permeability distribution, with the related porosity, for fault zones and fractures have

been proposed taking into consideration different conductive and sealing structures (Caine et al., 1996; Evans et al., 1997; Wilson et al., 2003; Mitchell & Faulkner,2009;Faulkner et al., 2010, 2011). This chapter focuses on existing research on porosity distribution, evolution, and relative deformation mechanisms in crystalline rocks presenting a ductile precursor overprinted by brittle deformation.

Porosity distribution has been described for the Alpine Fault in New Zealand, and in particular for its fault-rock assemblage formed at the brittle ductile transition (Kirilova et al., 2020). Low porosity values for the fault core are interpreted as indicative of porosity reduction due to the interplay of pressure solution processes and mineral precipitation (Kirilova et al., 2020).

A useful approach to determine relationship between deformation evolution of a fault zone, fluid flow and its bulk porosity is the study of hydrothermal systems developed along exhumed fault network (e.g., Egli et al., 2018). Presence of ductile precursor and the ductile strain intensity are observed to be key factor in the evolution of matrix porosity and subsequent localization of brittle fracture network (Egli et al., 2018).

Porosity observed in deformed crustal rocks is often related to different porosity generating processes such as dilatancy at grain boundaries, micro-cracking, and hydraulic fracturing (Oliver 1996; Billi et al., 2013). Under ductile deformation porosity could be produced by creep cavitation in rocks deforming by grain size sensitive creep (Fusseis et al., 2009; Gilgannon et al., 2017). In metamorphic environments other mechanisms could develop porosity even in the absence of deformation, in particular mineral dehydration reactions (Hövelmann et al., 2010; Plümper et al., 2017) and replacement reactions, where pores are generated due to volume differences between precipitated and dissolved minerals (e.g., Engvik et al., 2008).

In Olkiluoto, several studies have been conducted to characterize the permeability and retention properties of the host rocks, for which porosity measurement are necessary. Those studies applied different methods to characterize porosity, pore structure and other physical properties of Olkiluoto host rock. Porosity estimates for the host rock were derived with the 14C-labelled methyl methacrylate (MMA) method, which generates 2D porosity maps (e.g. Hellmuth et al. 1993, 1994, 1999; Siitari-Kauppi et al. 2010; Voutilainen et al. 2012; Kuva et al. 2012), Ar-gas pycnometry (Kuva et al, 2015, 2018) and X-ray tomography (Voutilainen et al. 2012; Kuva et al. 2012).

Host rock porosity is commonly presented for the two main lithologies pegmatitic granite (PGR) and veined gneiss (VGN) either as ranges 0.44–0.63 % (PGR) and 0.19–2.9 % (VGN) (e.g., Kuva et al. 2015), or as median values 0.38% for PGR and 0.43 for VGN (e.g. Jacobsson et al., 2016). Median porosity estimates for the drill core ONK-PH28 is 0.40%, with a sample variation from 0.1% to 0.91%, with VGN presenting the smallest range of 0.2-0.6% (Tiensuu et al., 2017). In general porosity is higher for altered rocks, reaching max values of 6.8% and decreases with depth of the sample origin in the ONKALO^{TM} tunnel. (Öhman et al., 2009). For both lithologies pores consist mostly of micrometer scale fissure, observed both internally and cutting the grains (Kuva et al.,2018, Ikonen et al., 2015, Sammalj ̈arvi et al., 2017).

This study aims to complement and expand the existing work with a detailed analysis of porosity characterizing a section of BFZ045 fault zone. Pore volumes and pore sizes were obtained using a combination of micro-Computed tomography (μ-CT) datasets, He-pycnometry and mercury intrusion porosimetry measurements; pore type classification was conducted using μ-CT and scanning electron microscopy images.

The application of multiple methods to characterize rock porosity, pore morphology and pore size distribution is a well-established practice (e.g., Halisch et al., 2016; Zhang et al., 2018), since each method provides information for a specific pore size range

(Anoviz and Cole, 2015). Moreover, none of the methods delivers the absolute value for the investigated parameters, be it pore size, porosity or surface area (Rouquerol et al. (1994). It is appropriate to address the limitations in the methods applied to the study and critically evaluate their validity prior to interpretation (Tullborg and Larson, 2006).

5.2 Material

All samples were obtained from the 100.42–100.71 m section of the PH28 drill-core, 28 cm long and with diameter of 5 cm (Fig. 5.1 a). This drill core section encompasses the transition from the proximal damage zone to the brittle fault core of BFZ045. It includes a mylonite in contact with a chlorite-rich cataclasite and a damage zone occurring in the coarse-grained host rock that is characterised by networks of chlorite veins (Figs. 5.1 a,b). It was cut in half parallel to the mylonitic stretching lineation (and to the chlorite slickenlines of the same orientation), and samples representative of the fault rocks were collected from the upper half-core (Fig. 5.1b).

Eight cylindrical samples (~1 cm of diameter and up to 2.3 cm in length) were drilled to perform micro computed tomography (μ-CT) at the University of Edinburgh (previously discussed in Chapter 3 and 4). To preserve as much material as possible, the remaining half-core was sub-sampled into rectangular prisms with ~ 1 x 1 cm base and variable length, whose corners were smoothed to approach a cylindrical shape. Sub-sampling of the core was carried out at the University of Plymouth.

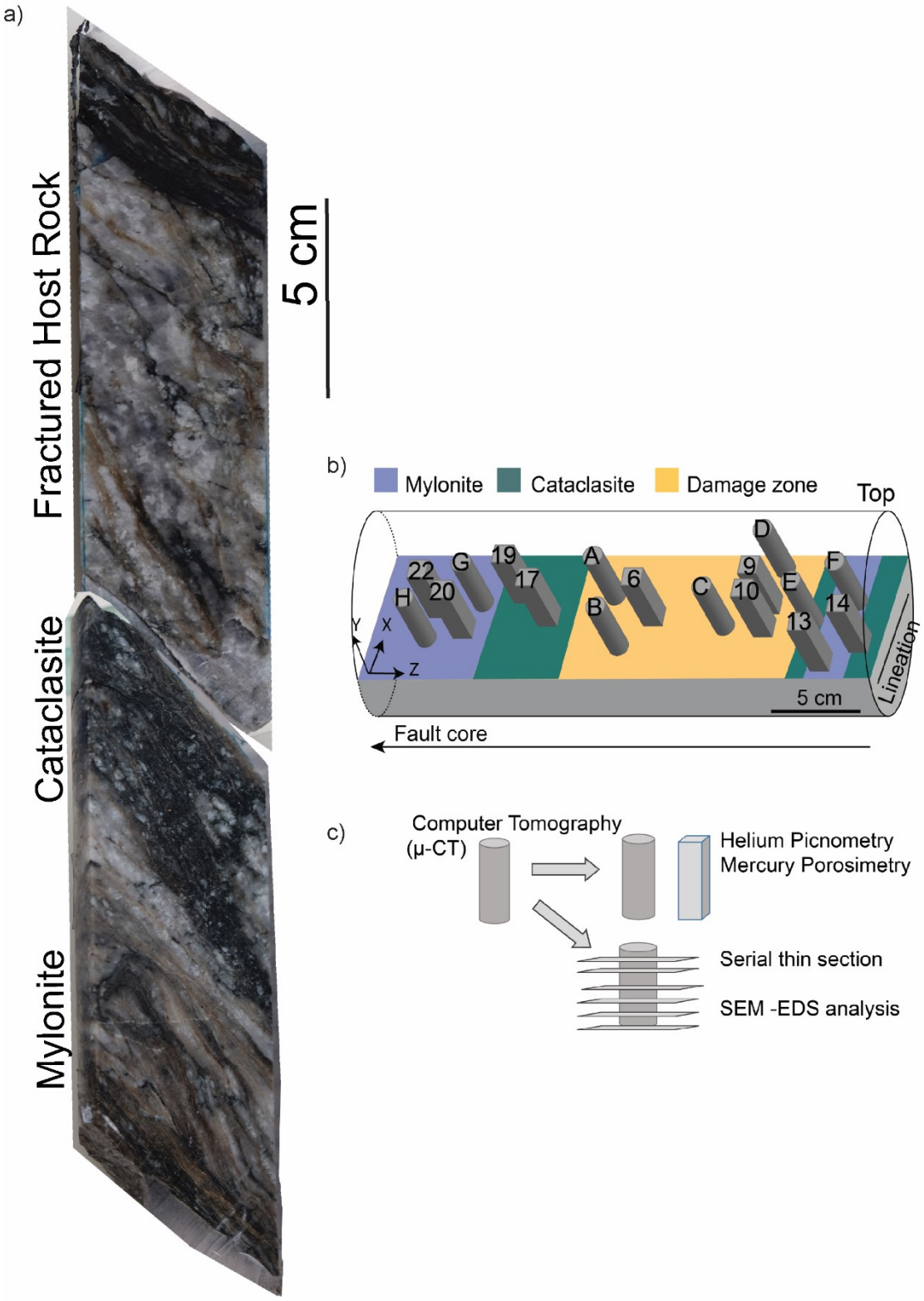

Figure 5.1 Schematic of sample preparation. A) Photograph of PH 28 upper half-core selected section, cut parallel to lineation. b) Schematic representation of faults domains based on macroscopic and thin section observations, illustrated on the lower half of the scheme. Grey 3D shapes in the upper half of the scheme illustrates sample and name location on the PH28 drill-core that can be related to c) sample treatment. Cylindrical samples obtained for µ-CT where used for either MIP analysis or serial thin sectioning. Prism samples were only investigated with MIP and He-pycnometry

Based on tomographic observations, three cylinders (A, D, G in Fig. 5.1 b) were selected for Helium (He) pycnometry and Mercury Intrusion Porosimetry (MIP), while the remaining cylindrical samples (B, C, E, F, H in Fig. 5.1b) where put into resin and cut into six serial thin sections, with a spacing of ~3 mm between each section. Polished thin sections were analysed using petrographic microscope and SEM in backscattered electron (BSE) mode in order to ascertain the textural position of pores and microstructures, and with Energy Dispersive X-Ray Spectroscopy (EDS) to identify the main mineral phases. (Fig 5.1 c). Nine prisms samples, of which at least two representative for each fault rocks, were also chosen for He pycnometry and MIP (Fig. 5.1 c).

5.3 Methods

5.3.1 Definition of measured porosity

In geology the term porosity is defined as the fraction of the volume of the void over the total volume. However, the definition and quantification of a 'void,' can have different meanings when related to different methods. It is necessary therefore to specify the definition of the used terms, to ease the reading. This chapter uses the definition of porosity, volumes and density provided in Webb (2001), briefly summarised here.

Pores can be divided in open and closed (cavities with or without access to an external surface). Most methods measure the open (or effective, interconnected) porosity and infer the closed porosity from volume or density differences in the sample (Anovitz and Cole, 2015). In this thesis, effective porosity (φ_e) is expressed as the percentage of the ratio between the volume of interconnected voids (V_e) and the bulk volume (V_b) of the sample. The bulk porosity (φ_b) is calculated as the volume of all the pores (V_p) normalized to the bulk volume of the sample, and does not differentiate between closed and open pores. Skeletal volume (V_s) is the sum of the volumes of the solid material in the sample and the volume of closed pores within the sample. Bulk and skeletal density are calculated from the sample mass divided by the respective volume.

5.3.2 Micro Computed Tomography (μ-CT)

Acquisition and reconstruction of the μ-CT dataset was performed by Dr. Ian Butler, at the Experimental X-ray Microtomography Laboratory at the School of GeoSciences, University of Edinburgh UK. Each sample was scanned with the same settings: 120kV peak energy, 10 W target power loading and 2000 projections, each with a 2s exposure time. After acquisition, tomographic slice reconstruction was performed using Octopus™ software. Digital image processing, data analysis and visualisation of 3D data was performed using dedicated workstations running Avizo™ software at the University of Edinburgh.

5.3.2.1 Digital Image Processing

Digital image processing was conducted using the software AvizoFire v.8.1 and Image J (Schindelin et al., 2012).

First the upper and lower reconstructed dataset were merged using the Image registration wizard function in AvizoFire v.8.1, to obtain an aligned stack of images. The stack was saved as sequence of images in .tiff files format (Fig 5.2a), and opened in Image J, where the contrast in the images was enhanced to facilitate the segmentation of the different mineral phases, and subsequently saved in Bitmap format (.bmp) to preserve the new contrast. Data were then filtered using an *Anisotropic Diffusion Filter 2D* to reduce image noise (Tschumperle and Deriche, 2005; Schlüter et al., 2014) (Fig 5.2b). This filter is a common non-linear deionising filter implemented in ImageJ (Perona and Malik, 1990), which smooths the image gradually, through a diffusion process, while preserving the edges. The diffusion stop criterion is set up manually by choosing the parameters a1, a2 and number of iterations. The parameters were chosen

following in the approach of Macente (2017): 20 iterations, and a1 and a2 set up to 0.7 and 0.5 respectively.

Segmentation of the chlorite veins network was performed using the ***Trainable Weka Segmentation*** Plugin (Arganda-Carreras et al., 2017) in the Image J/Fiji software. For most sample up to five classes (phases) were manually selected, colour coded in base of the different grey values selected for each class (Table 5.1; 5.2c). Training of the classifier was performed using 50 images from sample A manually labelled. After several attempts Gaussian blur, Sobel filter, Difference of Gaussians and Mean were selected for the training of a fast random forest classifier (Supek 2008). Based on the trained classifier, image representing probability maps where obtained, where the grey value for each pixel represents the probability of belonging to a specific class. Black indicates 0% and white 100% probability of belonging to a determined class (Fig 5.2c). The resulting hyper stack of images was saved as .tiff files and images were re grouped based on the corresponding class.

Class 1	Dark grey	Quartz/ Plagioclase
Class 2	Light grey	Chlorites
Class 3	Mid grey	K-feldspar/white micas
Class 4	White	Oxides
Class 5	Black	Pores

Table 5-1 Manually selected classes, characteristic grey values, and possible mineral component used for algorithm training in WEKA 2D.

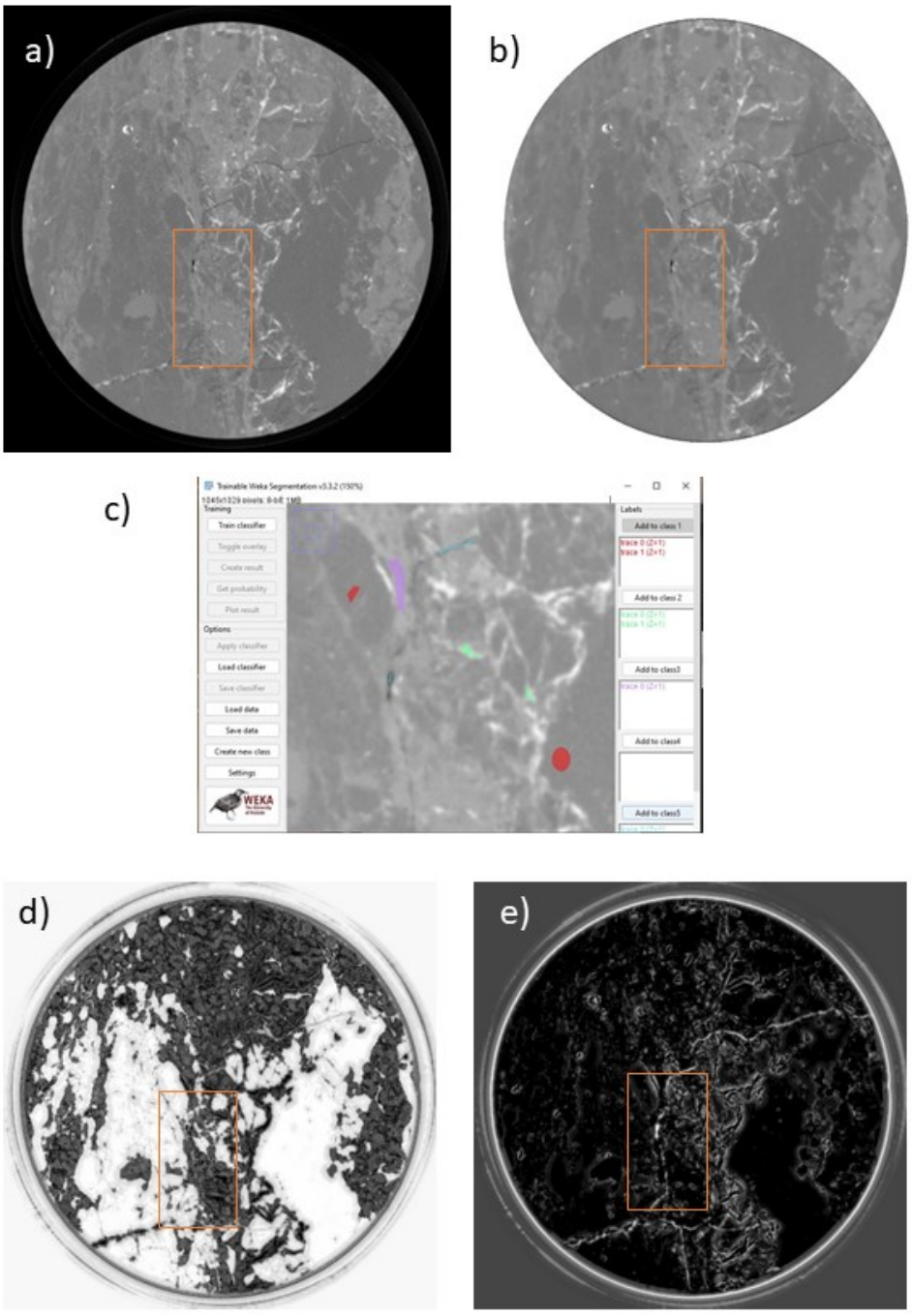

Figure 5.2 Visual representation of the workflow followed in Image J to segment each orthoslices from the 3D dataset. a) original image, b) image filtered with Anisotropic Diffusion 2D. c) WEKA 2D plugin interface. Colour areas represent user selected area for each class. Examples of probability maps obtained for d) dark grey values (quartz-albite class 1) and black values (porosity class 5).

Probability maps stacks were imported in Avizo 8 separately for each class. Using the *Edit new Label field* operation, only results with a 95% or higher probability were selected and transformed into a binary image. To discard small objects due to image processing and separate larger object the morphological operation *Opening* was applied, selecting a Cubic configuration, a 6 neighbourhood (which defines cluster if connected at least by a face) with half kernel size of 3px. Lastly, the object present on the binary images were identified using the *Labelling* operator. *Labelling* operator identifies connected aggregates of voxels in the segmented data. Like with the *Opening* operator, the degree of connectivity depends on the chosen neighbourhood: 6 (defines face-connected clusters) was applied for every class except for class5, representative of porosity segmented data, for which 26, that defines either a face, a side or a vertex in common, was selected. The resulting images present labels identified by different colours, which can repeat within the same dataset, as there is a limited number of colours in the map. *Label analysis* operator was used to characterise and quantify pore shapes. Pore size was obtained as the equivalent spherical diameter (EqD) (eq.5.1) for each pore.

$$EqD = \sqrt[3]{\frac{6 \times Volume}{\pi}} \qquad Equation\ (5.1)$$

Micro computed tomography images were used to quantify the pore volume and the porosity of the samples. The resolved pore volume is function of the spatial resolution of the µ-CT, which for this study is 20 µm voxel size. Estimates of porosity volumes from micro-CT depend on the segmentation strategy, which may vary from user to user. Estimated porosity values differ up to 20 % depending on the applied segmentation

procedure and noise level of the images (see Kirilova et al., 2020). Uncertainty of the porosity measurement can be obtained by comparing the results of μCT and helium porosimetry measurements (Jaques et al., 2021).

5.3.3 Microscopy

Five cylindrical samples (Fig 5.1) used for μ-CT were then polished into thin sections that could be used for further analyses using light microscopy and Scanning Electron Microscopy (SEM). SEM was used to obtain backscatter electron images (BSE) of the textural position of porosity, and to identify mineral phases and their distribution using energy dispersive spectroscopy (EDS). SEM data acquisition were conducted at the Plymouth Electron Microscopy Center using a JEOL 6610 SEM with tungsten filament equipped with an Oxford Instrument X-Max 80 EDS SDD detector, and at the Department of Geosciences of the University Oslo using a Hitachi SU5000 FEG-SEM equipped with Dual Bruker Quantax XFlash 30 EDS SDD detectors.

5.3.4 Helium Pycnometry

Helium pycnometry was used to measure the effective porosity (φ_e), the throat size distribution and the skeletal density (ρ_s) of the samples. Diameter and length of the samples were measured using a digital calliper with an estimated accuracy of 0.1 mm. Before the analysis, the samples were oven-dried for 24 hours at 50 °C, to eliminate possible surface humidity left during sample preparation. The samples were then weighed with accuracy of 0.001 gr.

Helium pycnometry analyses were conducted at the University of Plymouth, with a Thermo Fisher Pycnomatic ATC, a fully-automatic gas displacement pycnometer. For

each sample, a minimum of 3 to a maximum of 10 measurements have been recorded, each with standard deviation lower than 0.050 %. The atmospheric stabilization time was set at 600 second. The measured volume of the sample was recorded together with the calculated average density.

Effective porosity was calculated from the ratio of accessible volume and bulk volume of the sample. As Helium pycnometry measures the solid volume of the sample, accessible volume was determined from the volumetric difference between bulk and solid sample volume, which is dependent on the density used, which in this case was of 2.8 g/cm^3, typical for granite.

5.3.5 Mercury Intrusion Porosimetry

Mercury Intrusion Porosimetry (MIP) was used to obtain effective pore volume and pore throat size distribution. Mercury porosimetry measurements were conducted using a PASCAL 140/440 instrument from Thermo Fisher, characterized from a pressure range between 0.015 and 400 MPa. This pressure range equate to a pore throat radius between 100 μm to 3 nm. Pressure increase was set to 13 MPa/min. All the mercury intrusion curves were corrected by subtracting the result of a blank experiment. A blank experiment is a test conducted with the same pressure setting but without a sample in the sample chamber.

Pore volume was obtained by the cumulative intruded mercury volume in the samples, from intrusion curves plotted as a function of the cumulative pore volume (mm^3) against the pore throat diameter (micron). The diameter of the intruded pore at an applied pressure P was calculated by the Washburn equation:

$$d_{pore} = \frac{-4\gamma \cos\theta}{P} \qquad Equation\ (5.2)$$

With a value of 140° for the contact angle (θ) between the solid and the mercury and a value of 0.48 Nm^{-1} for the surface tension (γ)(Washburn, 1921). Those contact angle and surface tension values are commonly used for measurement at room temperature (25 °C; Giesche, 2006).

Pore throat size distribution curves, obtained from first derivative of the intrusion curves, are plotted in the form of pore volume in the vertical axis vs pore throat diameter in the horizontal axis.

5.4 Porosity Analysis

5.4.1 Porosity types

3D images from μ-CT scan were used to differentiate between two types of porosity: (i) fracture and (ii) matrix porosity (Fig 5.3). Micro fractures are mostly observed in samples from the damage zone (Sample B, Fig 5.3 a-b). Larger open fractures could be originated from sample preparation. Given the uncertain origin of fracture cutting through whole sample (Fig 5.3b), their volume was not quantified for μ-CT porosity estimates. Matrix porosity in μ-CT images could only be further differentiated into apparently isolated pores (Sample C, Fig 5.3c), or more clustered pores, but pores network was not possible to visualize. In the mylonite samples porosity is observed clustered inside plagioclase porphyroclasts (Fig 5.3 d), while in cataclasite samples porosity is more homogenously distributed (fig 5.3 e). BSE images of the serial thin sections were used to better differentiate the types of matrix porosity based on their textural position and dominant mineralogy (for each rock type).

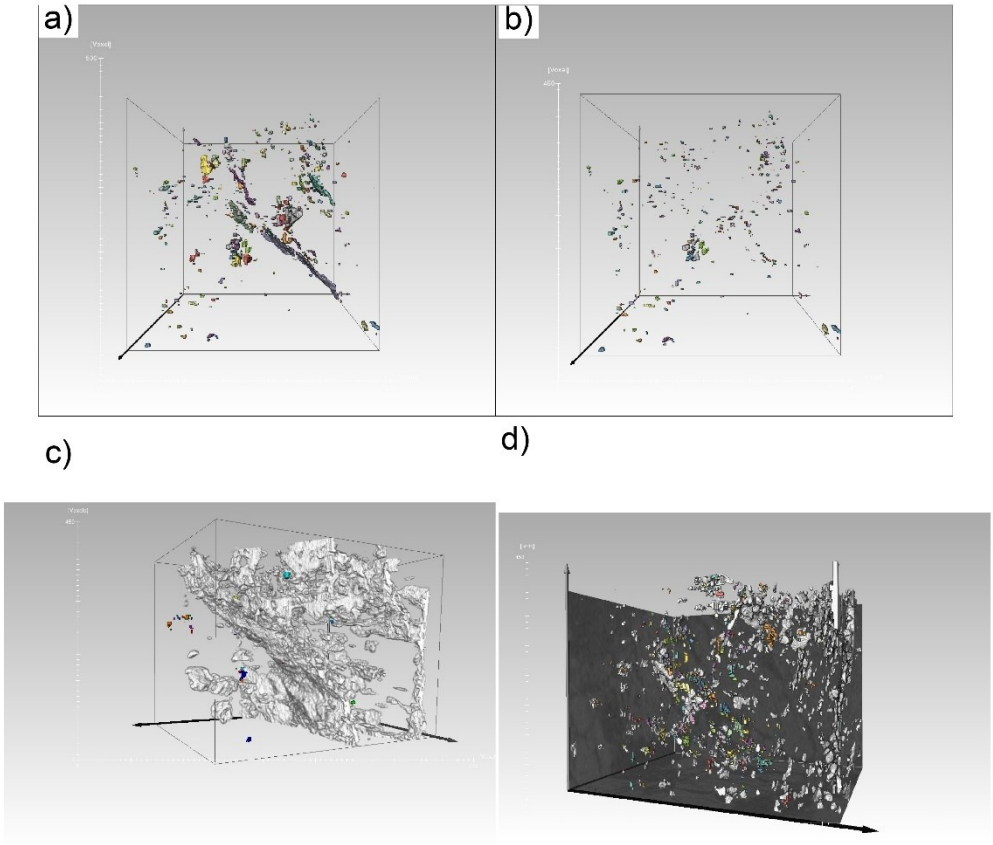

Figure 5.3 3D images (400x300x300 voxel) illustrating pore distribution in a-c)damage zone (sample B, C) and d) cataclasite (sample E). a) highlight total porosity comprised of fracture and isolated pores and b) shows only pore with volume smaller than 50 Voxels. c) overview of isolated and small clustered pores in the damage zone. Light grey volume is representative of chlorites. d) distribution of pores/ microfractures and chlorites along cataclastic band in sample E.

The mylonitic samples (F, G, H in Fig.5.1b) show intragranular porosity commonly related to feldspar porphyroclasts (Fig.5.4 a), and at the grain boundaries of recrystallized quartz (Fig. 5.4 b).

In the cataclasite, clusters of pores are preferentially observed in feldspar clasts (Fig. 5.4 c-d) and characterize the quartz-chlorite phase boundaries in the veins (Fig. 5.4d-e). In the veins recrystallized quartz shows grain boundaries pitting (Fig 5.4 f).

In the damage zone, porosity is concentrated inside perhtitic K-feldspars where it locally defines healed micro-fractures (Fig 5.4g), and plagioclase (Fig 5.4 h).

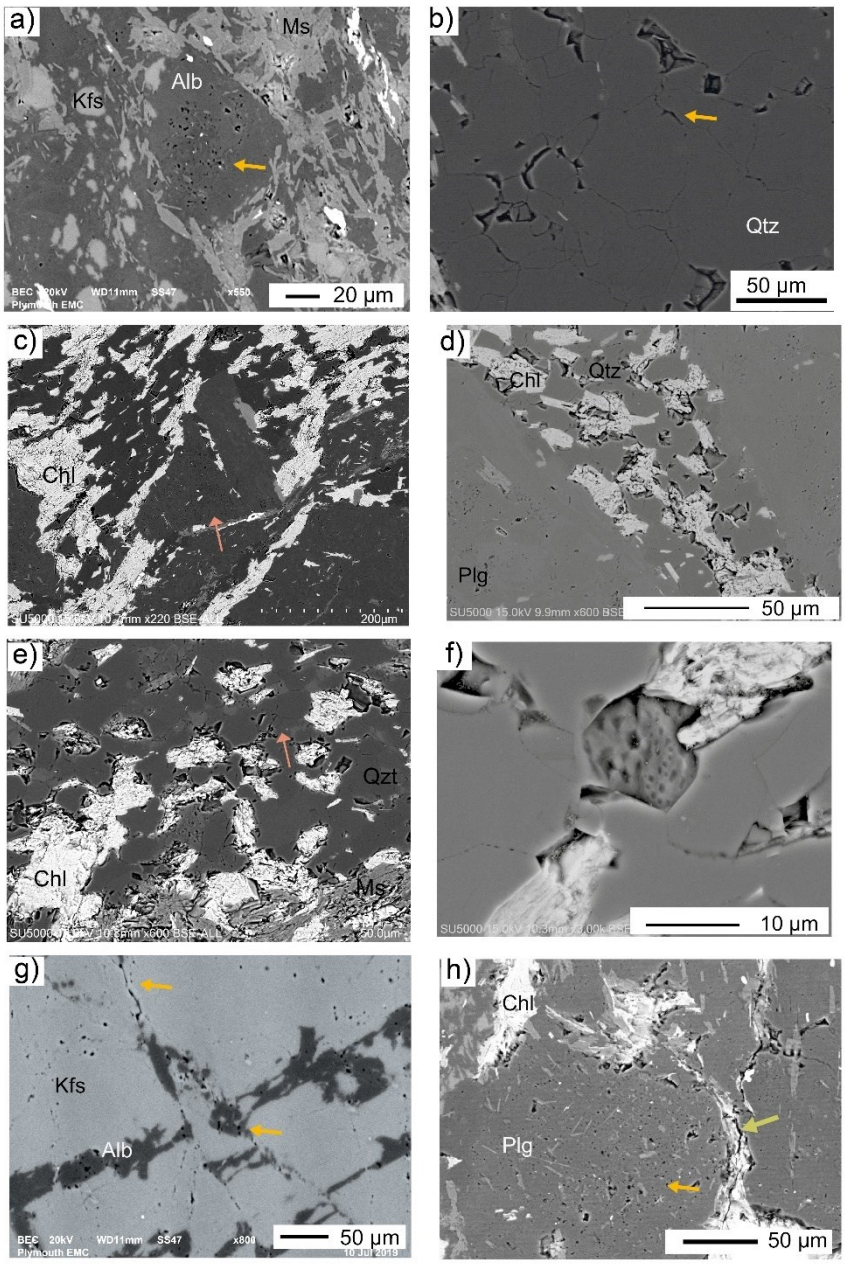

Figure 5.4 SEM images representative of the pores type. a) 'Clustered' porosity in albite porphyroclasts in the mylonite (sample H). b) Detail of pores along grain boundaries of recrystallized quartz in the mylonite. Yellow arrow indicate void located at the grain boundaries (sample F). c) Porous feldspar clast wrapped by a network of quartz-chlorite veins in the cataclasite. d) Porosity in quartz-chlorite veins and surrounding albite (sample PH28-22) e) Detail of pores in ductile deformed quartz along a band in the cataclasite. Yellow arrow indicate void located at the grain boundaries. (sample F) f) Detail of pitted grain boundaries of quartz inside of quartz chlorite veins (d) in the cataclasite, (Sample TS_23) g) Porosity inside perhtitic K-feldspar, orientation of pores indicate microfractures.(Sample C) H) porosity in plagioclase(Orange arrow) and surrounding microfractures (green arrow) in a cataclastic bands of the damage zone(sample A).

5.4.2 Pore size distribution

The distribution of the pore sizes is an important component in describing and quantifying the overall porosity of a sample. This study combines qualitative 2D analysis of pore size from SEM images with quantitative 3D analysis of pore body size and pore throat size from µ-CT and MIP (Fig. 5.5 and 5.6 respectively). For the mylonite, visual inspection of BSE images suggests a distribution of pores mainly in the range of 1-40 µm; smaller pores (<1 µm size) can be related to grain boundary porosity in quartz while larger pores (2-20 µm range) are commonly associated with feldspars porosity, prevalently as internal grain porosity (Fig 5.4 a)

Pore equivalent diameters observed at the µ-CT range between 20 to 200 µm, with median diameter 32-39 µm (Fig. 5.5, sample F-H). MIP curves for mylonitic samples show low volumes of intruded mercury (< 2 mm^3), and most of the intrusion occurs at pore throat diameters between 2 and 20 µm (Fig. 5.6a).

Pores observed in BSE images of cataclasite have a wider range, with sizes varying from 2 to 100 µm. Lowest pore size is observed along quartz grain boundaries inside the veins (<1 µm, Fig 5.4d-e). Porosity associated with feldspar is in the 5– 20 µm range (5.4c), while larger pores are locally associate with microfractures along the cataclastic matrix (Fig 5.4x). This heterogeneity is also observed in pore equivalent diameters measured with µ-CT, for pore size ranging between 20-300 µm (Fig. 5.5). MIP curves for cataclasite samples shows the highest volume of intruded mercury, though still overall low (< 4 mm^3), with most of the intrusion occurring at pore throat diameters between 3-10 µm (Fig. 5.6b).

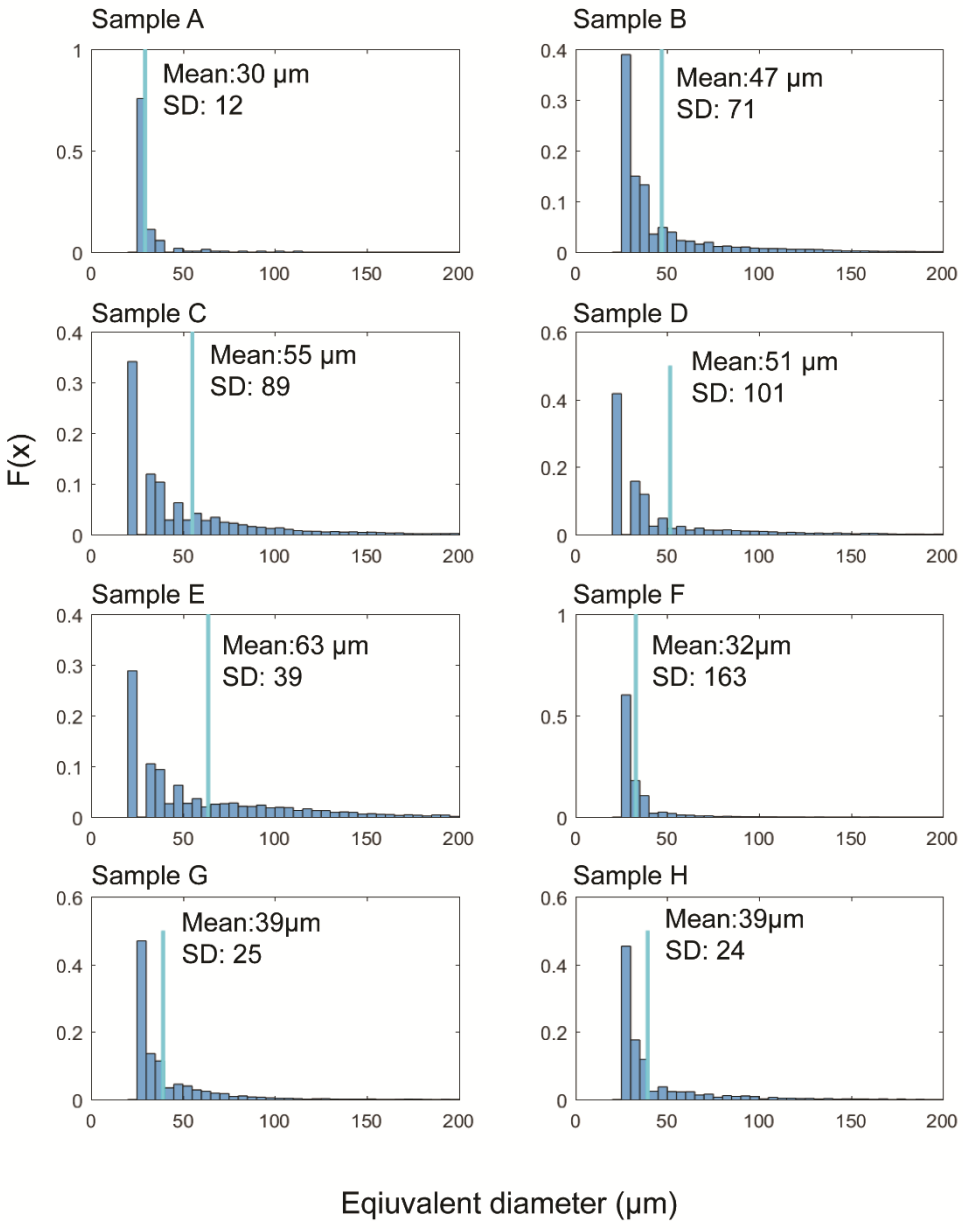

Figure 5.5 Pore size distribution histograms obtained from µ-CT analysis. Bin size 10 µm, threshold of measurements for equivalent diameter is 20 µm.

Pore size observed in BSE images of the host rock in the damage zone is related to K-feldspar, with mean pore size < 10 µm. The mean pore equivalent diameter for the damage zone is between 30-55 µm from µ-CT measurements (Fig 5.5). Mercury porosimetry intrusion curves for the fractured host rock samples shows a volume of intruded mercury between 0.6 and 2.5 mm^3, with pore throat diameters between 4 and 16 µm (Fig. 5.6c).

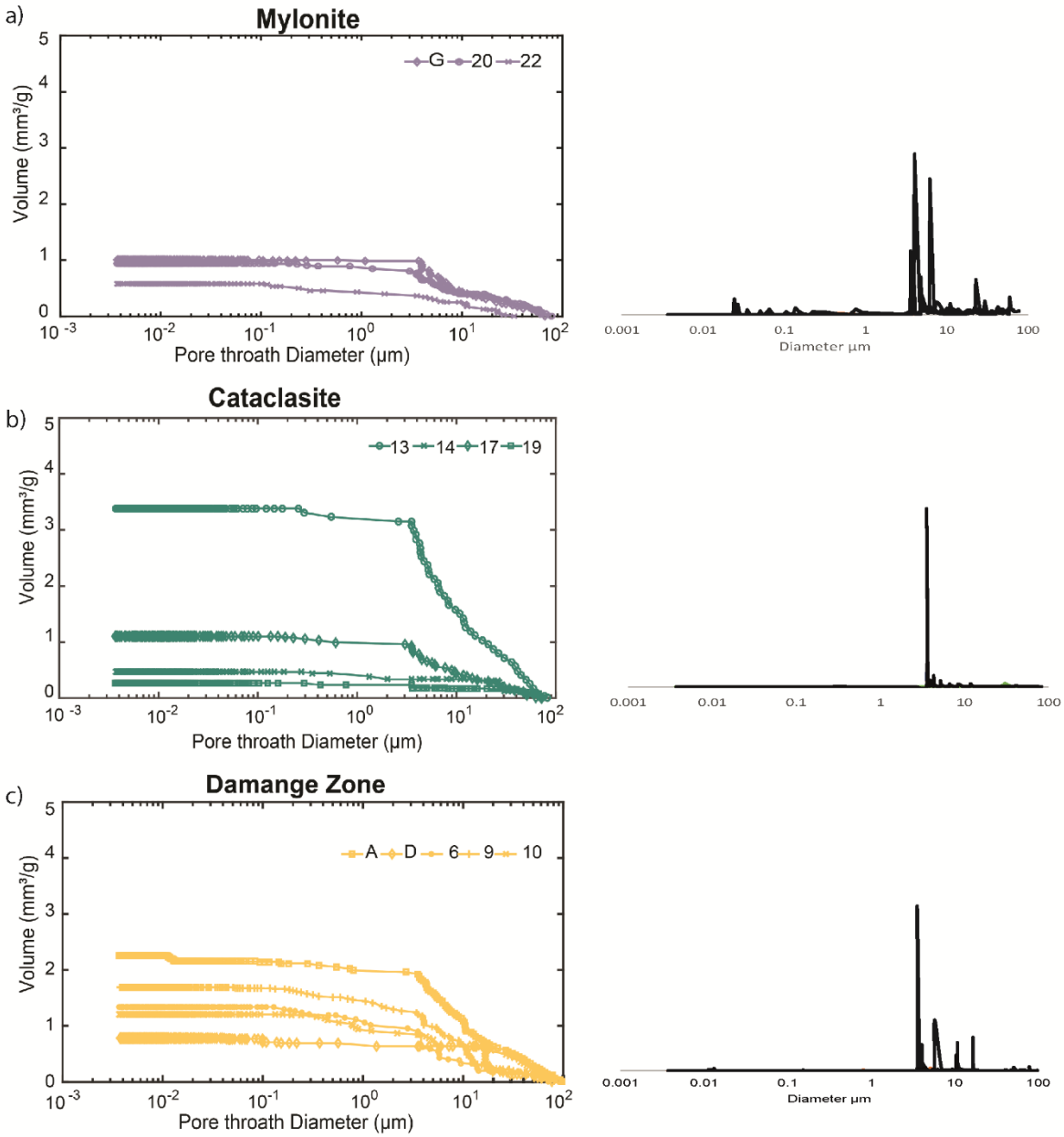

Figure 5.6 Intrusion and extrusion data from MIP and pore size distribution of intrusion data for Mylonite (a) cataclasite (b) and damage zone (c). The differential intrusion vs pore size graphs reflect the amount of pore space for a given pore throat diameter. The higher spikes indicate pore sizes that contribute the most to the overall porosity.

The total volume of fractures and pores larger than 20 µm was determined through 3D image analysis of µ-CT data of 8 samples. The measured volume was divided for the known volume of the sample to obtain a total porosity estimate for each sample, without differentiation between open and closed porosity. Table 5.2 shows the porosity obtained

for each sample. Porosity values for the mylonite are up to 0.1%. Sample E (Fig. 5.1b) is the only representative sample for the cataclasite, with a total porosity of 1%. The porosity of the damage zone range between 0.3- 0.9%.

He-pycnometry measurements determine pore volume and densities of the samples, and accessible pore volume of the sample was measured with MIP. Density and volume measurement are shown in Table 5.3. The obtained skeletal density ranges between 2.65 g/cm^3 to 2.83 g/cm^3, with no clear distinction between rock types. Porosity was calculated from He-pycnometry and MIP intrusion curves and is presented in Table 5.4. Mylonite has the lowest values of porosity, 0.10-0.14% for MIP and 1.1-1.6% for He-pycnometry.

Cataclasite containing quartz-chlorite veins shows the broadest range in porosity and the highest values, 0.05-0.72% for MIP. He-pycnometry measurements for the cataclasite do not show a similar variation, with values in the 1.4-3.8% range. The fractured host rock shows porosity between 0.06-0.20% (MIP), similar to the mylonite values, while He-pycnometry yields higher porosity values between 2.1- 6.1%.

Overall MIP and He-pycnometry measured low porosity values <0.8% and <7% respectively.

Sample Name	A	B	C	D	E	F	G	H
Rock type	dz	dz	dz	dz	cat	myl	myl	myl
Porosity φ	0.7%	0.5%	0.3%	0.9%	1%	0.09%	0.1%	0.1%

Table 5-2 Porosity estimates for μ-CT samples divided in Damage zone (dz),cataclasite(cat) and mylonite(myl).

	Sample	Mass (g)	Bulk Volume (cm^3)	Bulk Density (g/cm^3)	Skeletal Volume (cm^3)	Skeletal Density (g/cm^3)
Damage zone	A	3.2368	1.206	2.684	1.1939	2.711
	D	1.8663	0.716	2.607	0.6730	2.773
	6	1.7742	0.686	2.586	0.654	2.712
	9	3.4517	1.315	2.625	1.2569	2.746
	10	3.1363	1.206	2.601	1.1807	2.656
Mylonite/ Cataclasite contact	13	1.275	0.475	2.684	0.4656	2.738
	14	1.7854	0.653	2.732	0.6376	2.800
	17	3.2672	1.219	2.680	1.1736	2.784
	19	1.4564	0.522	2.790	0.5142	2.832
Mylonite	G	2.4153	0.882	2.738	0.8726	2.767
	20	2.4644	0.883	2.791	0.8713	2.828
	22	2.5013	0.930	2.690	0.9160	2.730

Table 5-3 Sample measurements and He-pycnometry measured volume and density

Damage zone

Sample	A	D	6	9	10	Mean Porosity	Median
φ_e He %	4.1	6.1	4.7	4.4	2.1	4.2±0.6	4.4
φ_e MIP %	0.19	0.12	0.06	0.13	0.10	0.12±0.02	0.12

Cataclasite

Sample	13	14	17	19	Mean Porosity	
φ_e He %	2.1	2.4	3.8	1.4	2.4±0.5	2.25
φ_e MIP %	0.72	0.07	0.09	0.05	0.23±0.16	0.08

Mylonite

Sample	G	20	22	Mean Porosity	
φ_e He %	1.1	1.3	1.6	1.3±0.14	1.3
φ_e MIP %	0.14	0.11	0.06	0.10±0.02	0.11

Table 5-4Measured effective porosity values of different rock type based on r He-pycnometry and MIP.

5.5 Discussion

5.5.1 Multi-method porosity estimations

Figure 5.7 shows the porosity results presented in table 5.1 and 5.3. First, it is evident that there is a substantial difference between the porosity values determined by He-Pycnometry and those determined by MIP and µ-CT.

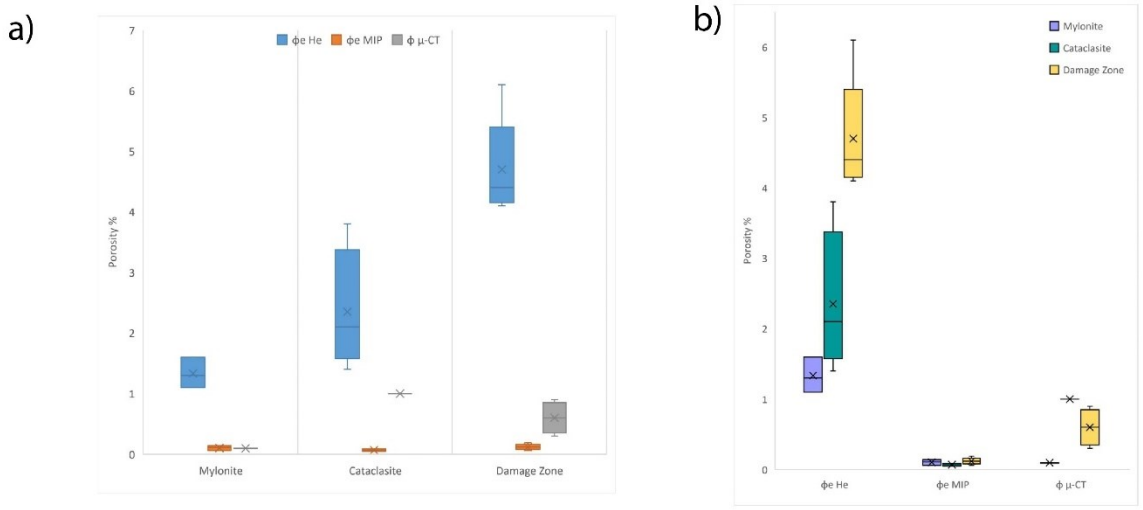

Figure 5.7 BOX plot graph summarizing the porosity values. a) porosity results are grouped for each rock type, and colours differentiate the used methods. b) grouped box plot represent results for each method and singular box plot showing results for the rock type. Spacing in the vertical axis was increased to let see the lower boxes, this introduces an exaggeration to the box plot with higher ranges (e.g. He pycnometry results). X point represent mean porosity values, while line represent the median value

He pycnometry not only has higher porosity values compared to the other methods, but also presents a wider range of porosities for each rock type. MIP and µ-CT values tend to vary less, especially when considering median porosities values. Higher effective porosity values derived from He pycnometry are due to the small size of Helium kinetic diameter, which permits to investigate a greater percentage of connected porosity. In low permeability rocks it has been shown that He pycnometry produce an overestimation (Anovitz and Cole, 2015).

The contribution of pores with diameters smaller than 3 nm, which is not taken into consideration during MIP measurements, may cause an underestimating of the porosity volume determined by MIP. Intrusion curves (Fig 5.6) however reach a plateau for pore size smaller than 1 μm, indicating that pore connectivity is controlled from pore larger than the nm scale limit.

Moreover, another limitation of MIP is that the measured intruded volume of mercury is controlled by the throat size of the pores, and not by the inner pore size.

The use of the Washburn equation to obtain the pore throat size induces an approximation since pores are assumed to have a cylindrical geometry (Giesche et al, 2006). The approach follows the connectivity model (Salmas et al., 2001) that states that for a pore to be filled with mercury a continuous path of mercury leading to that pore is required. In the case of a large pore connected by smaller pores, such pathway cannot be filled unless the pressure is sufficient to permit the entrance of mercury through the smallest entrance to that pore (known as Ink Bottle theory Giesche et al, 2006). Hysteresis between intrusion and extrusion curves (Fig 5.6) indicates that most pores trap mercury during the extrusion process, which is indicative of a high ratio between pore throats and pore size (Giesche et al, 2006).

The presence of larger pores and fractures is shown from μ-CT data (Fig 5.3), which show only pores with a volume bigger than the voxel size (20 μm). The calculated μ-CT porosity has been deemed representative of only a fraction of the total porosity, as μ-CT pore volume consists of open and closed pores. To be cautious the porosities obtained with He pycnometry have been considered as maximum value of porosity.

Median porosities values for the mylonite are the lowest for each method (Fig. 5.7), and for MIP and μ-CT are lower than the median values for host rock 0.4%. The highest estimation (1.3 % median porosity for He pycnometry) falls still in the range of host rock porosities (Kuva et al., 2015). In samples from the cataclasite and damage zone,

median porosities from µ-CT have higher values than MIP. MIP median porosities values (0.08 % for cataclasite and 0.12% for the damage zone) are lower than the median porosity for the host rocks (0.4%). Similarly to the mylonite, He pycnometry results in higher porosities estimate, whose median values (2.25% for cataclasite and 4.4% for the damage zone) are higher than the median porosity of the host rock, while still comparable with porosities values (up to 6.8%) of altered samples described for the host rocks (Öhman et al., 2009). Alteration of the samples have been only locally observed and is localized in plagioclase (see chapter 3 and 4) therefore these differences are interpreted as indicative of presence of microfractures and larger pores (Fig 5.3). The possible origin of such fine porosity is discussed in the next section.

5.5.2 Microstructural control on porosity variation in BFZ045 fault rocks

The observed porosity of the BFZ045 samples can be explained for each fault rock type based on its composition and microstructural characteristics. It needs to be kept in mind, however, that the observed porosity is the result of a complex history of deformation. As previously discussed, the lowest porosity estimates are from the mylonite, where pores are observed inside feldspar porphyroclasts and at the grain boundaries of quartz (Fig. 5.4). Porosity in K-feldspar related to the formation of albite lamellae is commonly observed in granitic rocks in nature (e.g., Worden et al, 1990; Walker et al. 1995; Plümper and Putnis, 2009; Hentschel et al., 2019) and experiments (Norberg et al., 2011). Cuspate boundaries of albite at the interface of K-feldspar porphyroclasts suggest dissolution-precipitation (Norberg et al., 2011), while albite grains along fractures within K-feldspar might be indicative of neo crystallization in the presence of a fluid phase (Fig. 5.4) (Stünitz and Gerald, 1993; Eberlei et al, 2014). Porosity in

porphyroclasts could be also related to process of albitization of plagioclase trough interface-coupled dissolution–precipitation mechanism (Hövelmann et al., 2010; Plümper et al., 2017; Giuntoli et al., 2018).

In the mylonite of interest is the porosity observed on BSE images located at the grain boundaries of recrystallized quartz (Fig 5.4b), with pores diameter rarely larger than 2 microns. As discussed in Chapter 4, quartz in the mylonite recrystallized via subgrain rotation recrystallization. It has been demonstrated that monomineralic recrystallized aggregates can produce creep cavities due to a combination of Zener-Stroh cracking and viscous grain boundary sliding (Gilgannon et al., 2017, 2020), possibly coupled to dissolution (Mancktelow, 1998). In line with these studies, we infer that the creep cavities at the quartz grain boundaries emerge with subgrain rotation recrystallization in the presence of grain boundary fluids.

Low porosity values of the mylonite are consistent with an overall viscous deformation regime, where viscous compaction and flow are generally not associated with significant dilatant deformation (Connolly, 2010), unless deformation mechanisms are capable of generating and maintaining a dynamic porosity and permeability (creep cavitation model presented in Fusseis et al., 2009; Menegon et al., 2015). Pore formation by creep cavitation generates porosity that varies dynamically as function of strain gradient and nucleation by precipitation of new grains from a fluid phase (Fusseis et al., 2009; Précigout et al, 2022).

Similarly, to what has been discussed in chapter 4, BFZ045 microstructures indicate that an undergoing ductile deformation was punctuated by brittle events in the form of cataclastic deformation and veining. Therefore, porosity values obtained for cataclasite samples are interpreted as a result of multiple mechanism of porosity formation, and could be affected by the inherited porosity from the hosting mylonite.

Through the formation of fractures, brittle deformation enhances porosity (Marone et al., 1990), consequently influencing permeability (Sibson, 1990). Sealing mechanism leading to porosity decrease over time can be related to in situ dissolution-precipitation processes, such as pressure-solution processes (Renard et al., 2000; Faulkner, 2010) or mineral precipitation from an external fluid (Giger et al., 2007).

In the veins of the cataclasite pores at the recrystallized quartz grain boundaries, small chlorites at the triple point of quartz grains and the pitted quartz surfaces (Fig 5.4) suggest that creep cavitation was an active mechanism following the veins emplacement (Gilgannon et al., 2020), as concluded for the mylonite.

In the damage zone, most of the pores are observed in perhtitic K-feldspar along healed microfractures, possibly representative of fluid inclusion planes, and at the core of plagioclase/albite (Fig. 5.4), suggesting that porosity observed in the damage zone is at least partly inherited from the host rock. Mineral inclusions observed in the plagioclase (Fig 5.4h) could be used as indicator of variation in porosity occurring during plagioclase replacement reactions (Plümper & Putnis, 2009; Plümper et al., 2017; Putnis, 2015).

Macro-fractures are what influences more the porosity estimates from the host rock (see section 5.4.1). Origin of those fractures could be related to partial precipitation of minerals in veins, or most probably are due to sample preparation, and will be discussed in chapter 6.

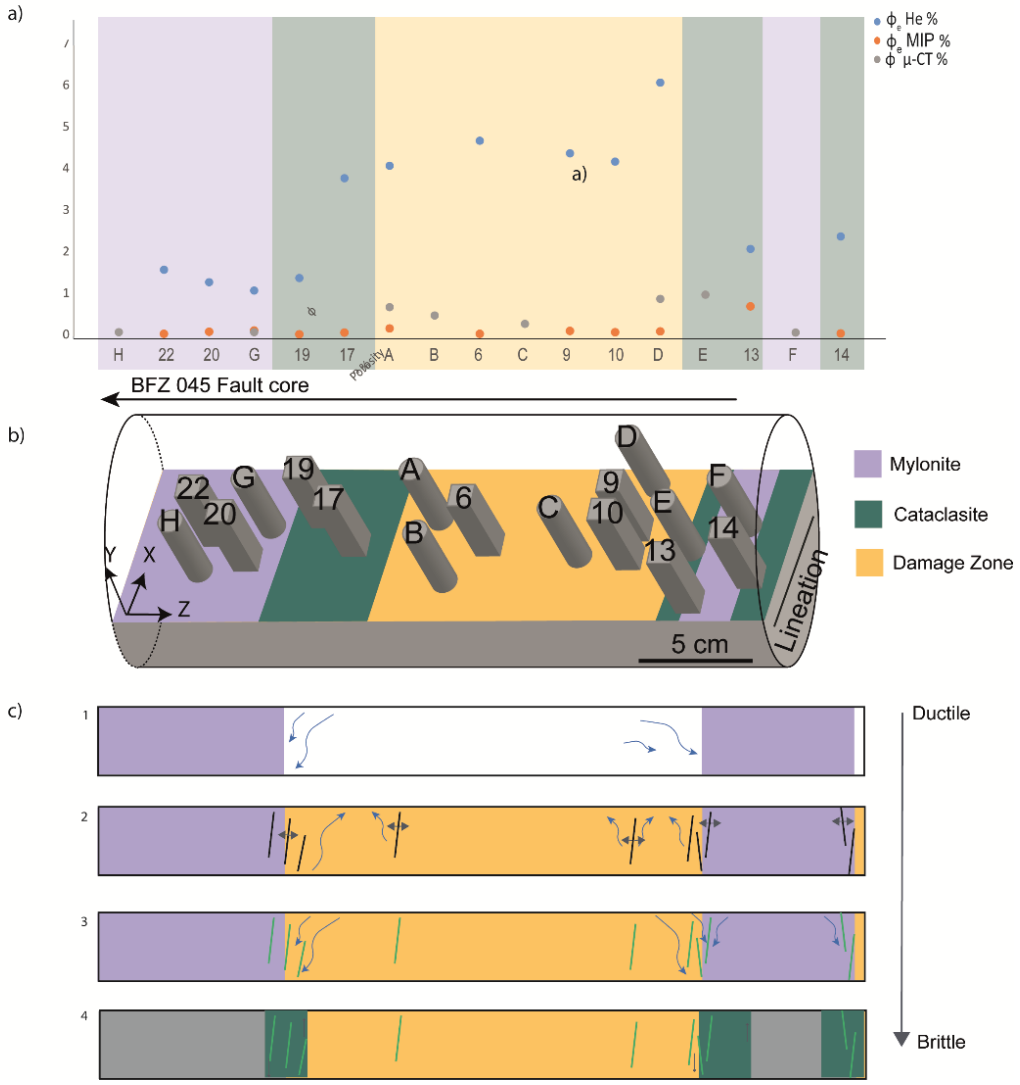

Figure 5.8 Visual representation of porosity data and deformation mechanism distributed along the PH28 drill core. a) Porosity distribution along sample section. b) Schematic representation of faults domains based on macroscopic and thin section observations, illustrated on the lower half of the scheme. c) Visual representation of porosity generating mechanism active during Bfz045 evolution.

Geometry of the selected drill core section is representative at a smaller scale of the geometry of BFZ045, with mylonitic ductile precursor overprinted by brittle deformation. Distribution of the porosity along the core samples shows an increase of values from the mylonite towards the damage zone (Fig 5.8a). Studies shows that brittle fault core have higher porosity than surrounding rocks, due to effect of high strain and repeated fracturing (Faulkner et al., 2010; Egli et al., 2018). Low porosities along fault

core have been interpreted as the result of effective porosity reduction mechanism via efficient crack healing and sealing (Kirilova et al., 2020).

The estimated porosities for BFZ045 are the result of multiple processes that took place during the fault evolution. Porosity in the host rock has been described in relation to dissolution–precipitation mechanism and alteration (Kuva at al., 2018; Öhman et al., 2009). Strain variations and recrystallization mechanism in the mylonite can be linked to pore formation by creep cavitation and dissolution-precipitation (Fusseis et al., 2009; Precigout et al, 2019) leading to a dynamic porosity evolution under ductile conditions. Changes in porosity can affect the permeability of the surrounding rocks, potentially leading to local fluid overpressure (Cox, 2010; Kjøll et al., 2015) (Fig 5.8 b). Increase in pore fluid pressure can results in (hydro) fracturing with consequent release of pore pressure and short-term permeability enhancement, even under ductile conditions. Presence of veins can be used as evidence of such temporary permeability (Gomila et al., 2016, 2019). Subsequent mineral precipitation decreases the porosity, and can introduce weaker phases, such as phyllosilicates (Niemeijer and Spiers, 2005). Interplay of pore formation and reduction under ductile condition can affect the overall behaviour of the fault during time and could act as localization mechanism not only for fluid, but also for development of brittle structures, such as the cataclasite in BFZ045. This is consistent with the model of fault-zone evolution derived in Chapter 4, which indicates that quartz-rich veins formed transiently during ongoing mylonitization as a consequence of oscillating fluid pressure conditions. Marchesini et al. (2019) proposed the same cyclical fault-slip behaviour, largely steered by fluctuations in the fluid pressure, for the conjugate BFZ300 fault.

5.6 Conclusion

Porosity and pore size were estimated for different structural domain of a core section representative of the BFZ045 fault geometry. Multimethod approach was helpful to investigate pores at different scales and interpret volumetric measurements obtained from He pycnometry and MIP in relationship to microstructural observation from SEM images and 3D porosity distribution from µ-CT data. Pores have been observed along grain boundaries in recrystallized quartz in mylonite and cataclasite, as intra-granular porosity in feldspar and locally as microfractures. Overall, the samples present low porosity values, with median porosity values range from 0.08 to 4.4%. Estimated pore size varied from 1 to 100 µm, with pore throat diameters, representative of pore connectivity, mostly observed for values in range between 2-20 µm. Porosity formation and reduction mechanism have been proposed for different rock type. Under ductile conditions, interplay between creep cavitation, mineral replacement reactions and mineral precipitation from fluid is deemed responsible of dynamic changes in the porosity, which coupled with fluid overpressure drive the occurrence of brittle events. It is suggested that evolution of porosity is strictly related to deformation events previously described in the thesis, and overall is an important factor for BFZ045 fault evolution.

6 Spatial distribution of Chlorite filled fracture along BFZ045

6.1 Introduction

Fault zones and their fracture network play an important role in the migration of fluids through the continental crust (Sibson, 1992; Cox et al., 2002; Mizoguchi et al., 2008).

A fracture network can be described as a system of fractures that developed in time within the same rock volume and could consist of multiple fracture sets (Peacock et al., 2016). Fracture sets are generally grouped by their geometry, type or mineral fill, which can, in turn, be used to distinguish between structural events within the evolution of a fracture network.

Evidence of paleo- fluid flow through a fracture network is commonly associated with veins, dilatation sites in which mineral aggregates precipitate from a fluid (Bons et al., 2012). Analysis of shape, orientation and interconnection of fractures can be used to assess stress field, deformation kinematics, fluid pressures, and fracture mechanisms (Oliver and Bons, 2001; Peacock and Sanderson, 2018; Cox 1999; Cox et al. 2001; Sibson 1996; Smith 1997). Internal microstructures and composition of veins are useful to infer both mechanical (Bons 2000: Urai et al. 1991: Koehn et al., 2001,) and chemical (Fisher et al., 1995; Schulz et al., 2002; Barker et al., 2009) processes of vein formation and their relation (e.g., Elburg et al., 2002, Barker et al., 2006,).

The development of vein in a rock mass can influence the strength and the subsequent deformation of the host rock. Moreover, heterogeneities in the host rock, such as anisotropy, play a significant role in influencing the orientation and propagation of veins (Platt and Vissers, 1980; White et al., 1980). A possible mechanism of vein

emplacement requires pre-existing anisotropies, such as fractures, favourably oriented, which are reactivated after fluid pressure exceeds the normal stresses acting on the fracture wall. If the condition of cyclic increase of fluid pressure is considered, fractures opening along such pre-existing anisotropies could occur also under ductile conditions, with a mechanism known as fault-valve action (Sibson et al., 1988; Sibson, 1992, 1996, 2000; Cox et al., 2001). The flow of fluid into the open fractures could lead to an 'instantaneous' drop in fluid pressure, responsible for mineral precipitation and vein formation (Cox et al., 1991, 2001; Cox, 1995). The deposited vein materials would seal the fracture, returning the system for the next cycle of deformation. Repeated cycles of fluid pressure build-up, rupture, fluid flow and vein formation would then generate a veins network in host rocks (Blenkinsop et al., 2020; Belgrano et al., 2016;).

In Olkiluoto, vertical N-S to NNE-SSW trending faults represent the earliest brittle structures (Stage I, Fault system I fig 5.1) identified from inversion of fault slip data and cross cutting relationship (Mattila and Viola; 2014). Those vertical strike-slip faults are approximately parallel to ductile precursors (D1-D4), high-grade ductile shear structures (Skyttä and Torvela, 2018) that formed along the limbs of F4 folds towards the end of D4 (ca.1.81 Ga ago, Aaltonen et al., 2016). Short fault segments, most-likely controlled by these ductile precursors, evolved into more continuous faults, through linkage of secondary fractures (Skyttä and Torvela, 2018). The brittle structures developed at the transition from an overall ductile to brittle regime, occurring ca. 1.79–1.75 Ga ago (Torvela et al., 2008; Aaltonen et al., 2016), and were later reactivated at ca 1.3–1.2 Ga (Nordbäck et al. 2022). As previously discussed, (Chapter 4 of this thesis, Prando et al. 2020), BFZ045 is a sinistral strike slip fault, associated to Fault system I with an average orientation of 87/095 (dip/dip direction) with the presence of a mylonitic precursor (Fig 6.1). Similarly, to other faults of the same system synthetic R and antithetic R' shears are present in the damage zone (Fig 6.1 a, Nordbäck et al. 2022).

The fault core is characterized by the presence of quartz veins, and the most common minerals observed lining fractures are smectite, chlorite and illite (Aaltonen et al., 2016, Nordbäck et al. 2022). Quartz veins (parallel to the foliation), chlorite veins and chlorite-rich cataclasites have been interpreted as a primary indicator of brittle deformation along drill cores intersecting BFZ045 (Prando et al. 2020).

This chapter approach the analysis of chlorite-filled orientation and their distribution along the fault, in a tentative to discern possible relationships with the ductile precursor.

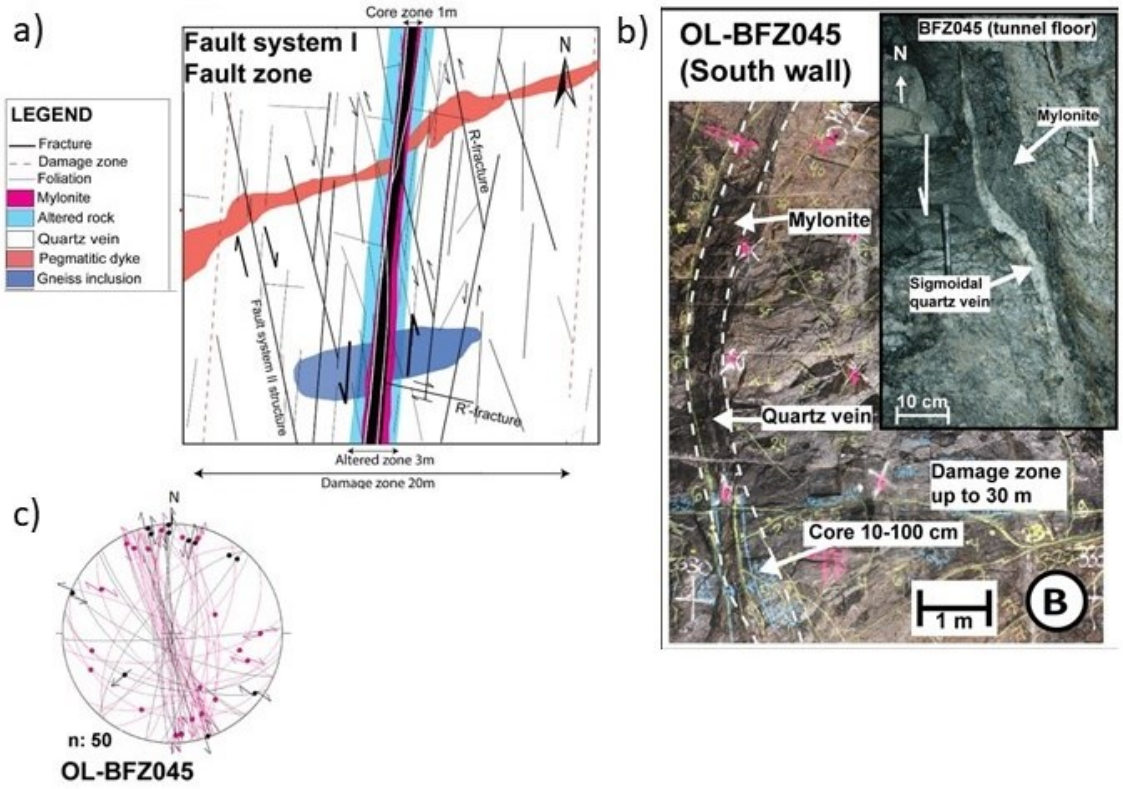

Figure 6.1 A) Schematic map of a Fault system I fault zone. b) photographs of BFZ045 from the tunnels of ONKALOTM. Yellow lines on tunnel walls are paint marks from tunnel mapping. C) BFZ045 kinematic fault data (lower-hemisphere Schmidt projection, black great circles: fault cores, pink great circles: fault damage zone) (modified from Nordbäck et al. 2022, used under CC.BY 4.0)

6.2 Materials and Methods

Samples discussed in this chapter are eight cylinders from the upper half-core of drill core PH28 , of ca.1 cm in diameter and up to 2.3 cm in length (samples A-H), collected orthogonally, in respect of the cut surface parallel to the stretching lineation (Fig. 6.2a).

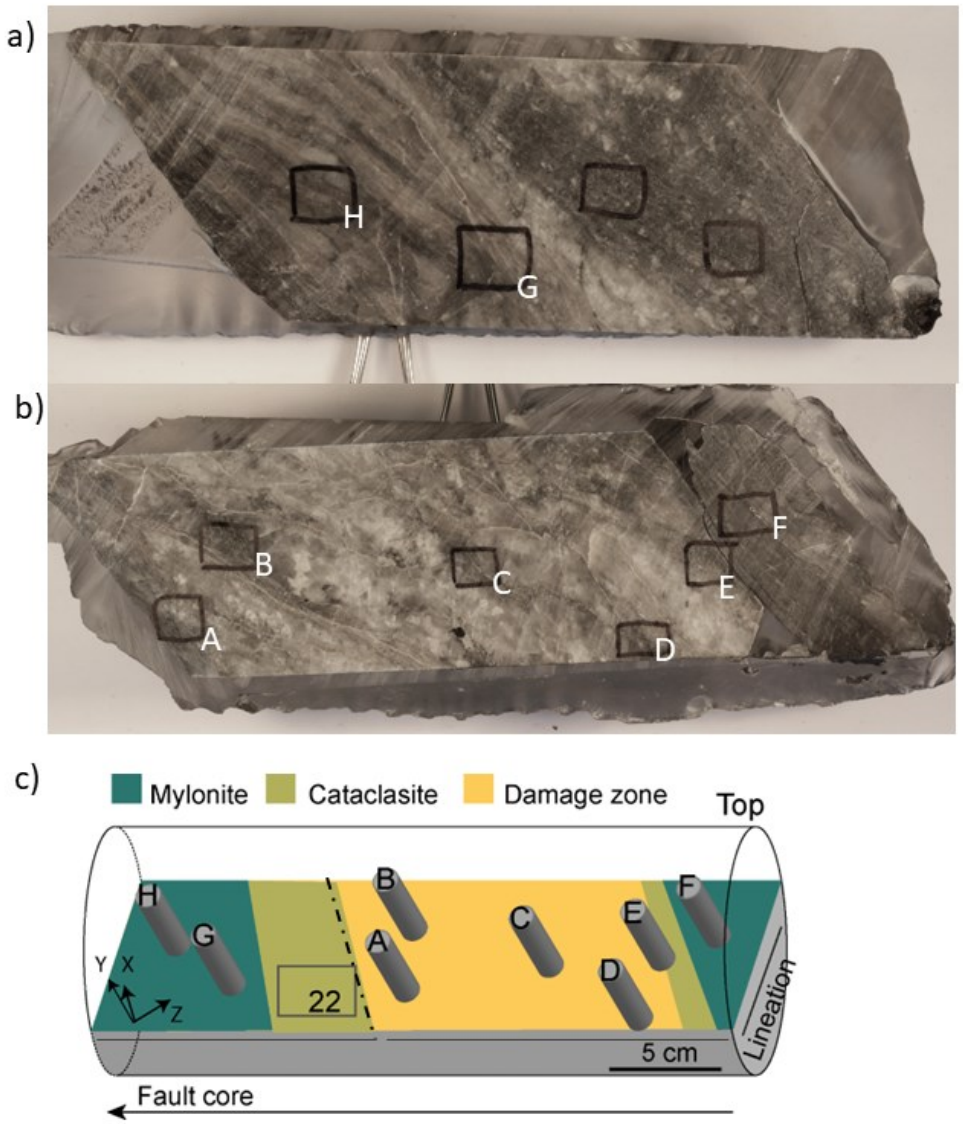

Figure 6.2 a,b) Photograph of PH28 upper half-core selected section, cut parallel to lineation. Black squares indicate samples position. c) Schematic representation of fault domains based on macroscopic and thin section observations, illustrated on the lower half of the scheme. Grey 3D shapes in the upper half of the scheme illustrates sample and name location on the PH28 drill-core. X and Y define the foliation plane. Z is the pole of the foliation plane.

The mini cores have been used for micro-computed tomography (µ-CT) data acquisition. After image processing of µ-CT dataset, five cores (B, C, E, F, H in Fig. 6.2 b) were put into resin and cut into six serial thin sections, with a spacing of ca. 3 mm between each section. The remaining cores have been utilized for MIP analysis (see previous chapter). A thin section (PH28_22) from the drill core PH28 was also obtained to investigate the chlorite-rich cataclasite. Polished thin sections were analysed using petrographic microscope and SEM in backscattered electron (BSE) mode in order to investigate vein microstructures, and Energy Dispersive X-Ray Spectroscopy (EDS) was used to identify the main mineral phases.

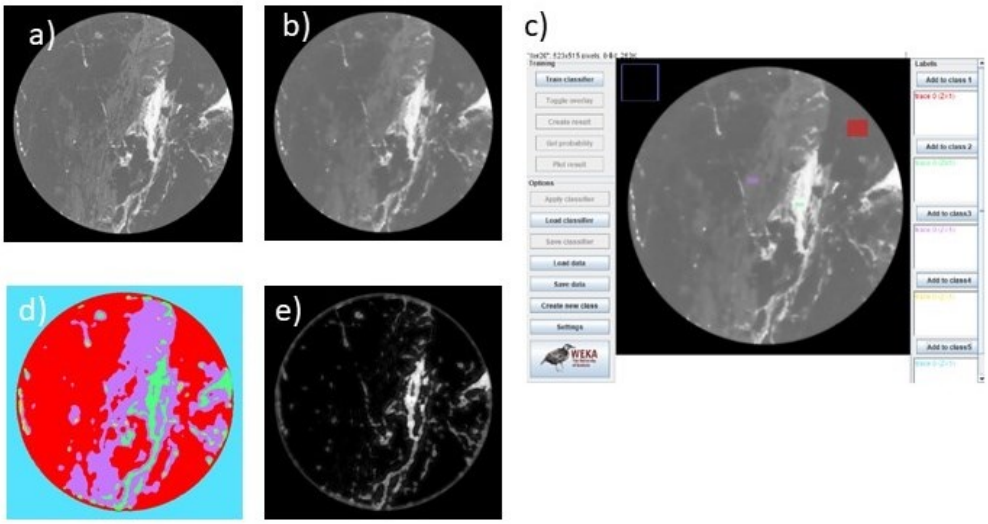

Figure 6.3 Visual representation of the workflow followed in Image J to segment each orthoslice from the 3D dataset. a) original image, b) image filtered with Anisotropic Diffusion 2D. c) WEKA 2D plugin interface. Rectangles represent user selected area for each class. d) Result of WEKA 2D algorithm training for segmentation, different colors represent the selected class e) example of probability maps obtained for class 2/ chlorite (represented in green in figure d)

The image acquisition settings and segmentation process for µ -CT images have been previously described in section 5.2 of this thesis. The µ -CT images have been re-oriented with the Avizo™ software, rotating the images to have the previously

annotated foliation trace in the samples parallel to the x-axis of software reference system, and the vertical axis of the sample parallel to the z-axis of the software. Segmentation of chlorite used as proxy for sealed fracture identification on µ-CT dataset is summarized in figure 6.3.

Separation of intersecting chlorite fractures through the segmentation process was not sufficient to properly separate the 3D volumes to be used for orientation analysis. The segmented dataset was therefore used for visualization purposes. Orientation analysis of the chlorite-lined fracture was then conducted on orthoslices (2D images) parallel to the xy plane of the Avizo™ software.

6.2.1 Image Analysis

Measurements of vein orientations were conducted on ImageJ/Fiji software. Table 6.1 reports the selected slice numbers for each sample, corresponding to a slice interval of 50. Due to the geometry of the samples not being perfectly cylindrical, upper and lower slices were not considered for the measurements. For each image, using Adobe Illustrator, veins were manually traced as line segments along the vein lengths (the procedure applied is common to digital analysis of fracture sets from a variety of other imaging methods e.g. Healy et al., 2017). Vein apertures were measured perpendicular to the vein walls (average width values are used for each vein length segment).

Angles and lengths of the traced segments were obtained using the *analyse particle* operator in Image/J. Results were saved as .csv file and plotted as equal-area rose plots using MATLAB software. Cumulative orientations of the line traces are represented with half circles (0°-180°) rose plots, separated into 10° bins, plotting length-weighted frequency (where the frequency was scaled to the fracture length) and aperture-

weighted frequency (where the frequency was scaled to the average fracture width). The orientation of each segmented vein is directly referenced against the trace of the foliation plane, which was set parallel to the vertical axis of the slices image in each case.

Sample name	Structural domain	Number of slices	First analyzed slice	Last analyzed slice	Number of slices
A	Damage zone	1665	175	1025	18
B	Damage zone	1885	500	1350	16
C	Damage zone	2099	110	1710	33
D	Damage zone	1452	108	402	7
E	Damage zone/ cataclasite	2088	50	1250	25
F	Mylonite	2012	400	1300	19
G	Mylonite	1396	200	1050	18
H	Mylonite	2286	200	2000	37

Table 6-1 Summary of trace orientation analysis samples

6.3 Results

6.3.1 Mylonite (Samples G-H)

Chlorite mostly occurs along the foliation in the mica-rich layers, either with grains elongated along the foliation (Fig. 6.4a) within pressure shadows of feldspar porphyroclasts, or with a radial to massive texture in combination with oxides and apatite (Fig. 6.4 b).

Fractures, lined with chlorite, are mostly observed in feldspar rich layers as hybrid extensional fracture (ModeII/III+Mode I), with chlorites stretched along fractures in between domino type porphyroclasts (Fig 6.4 c). Locally they present as shear fractures (Mode II/III) with fine-grained mineral habit parallel to the shear direction and forming conjugate set (Fig 6.4 d). Veins non-parallel to the foliation have similar orientation to sinistral shear fractures and are mostly hybrid veins,

Quartz-chlorite fractures are preserved along foliation and inside porphyroclasts mostly as Mode I fractures (Fig. 6.4c, e,f), but there appear to not be any continuity with the chlorites surrounding the clast an in its pressure shadows (Fig. 6.4 d|). Chlorites have fibrous habits and present syntaxial growth perpendicular to the fracture wall.

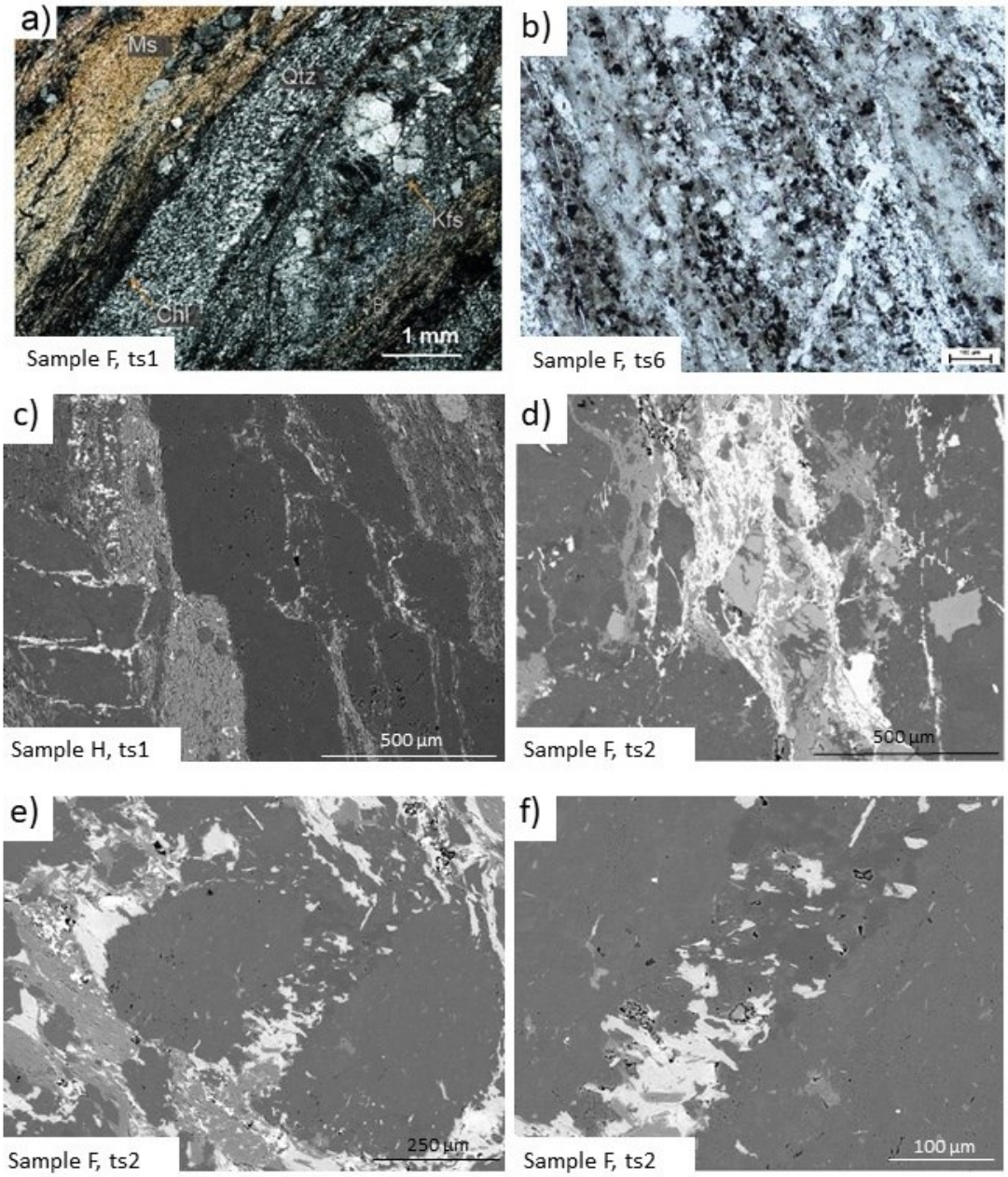

Figure 6.4 Chlorites in the mylonite at light microscope, SEM. a)Chlorites along the mylonitic foliation, b)chlorite veins elongated subparallel to the foliation c)overview of chlorite filled fracture and quartz-chlorite fracture parallel to the foliation d) conjugate set of chlorite fractures(left in the image) and chlorite matrix cutting feldspar grain e) Fractured porphyroclasts of plagioclase cut by quartz-chlorites fractures f) Detail of e, showing chlorite crystals are elongated perpendicular to fracture wall.

µ-CT images representing Chlorite volume Shows preferential orientation of chlorite along the anastomosing foliation (Fig 6.5). In the mylonitic samples (F, G) (Fig. 6.5) separation of chlorite veins of was not highly successful due to presence of chlorite and biotite along foliation, which resulted in a possible overestimation of chlorite volumes

along the foliation. Similarly, chlorite in the analysed 2D images of the mylonite samples appear to be mostly oriented along foliation, with chlorite fractures showing then a preferred orientation at ca. 120° and 140° to the mylonitic foliation (Fig 6.6).

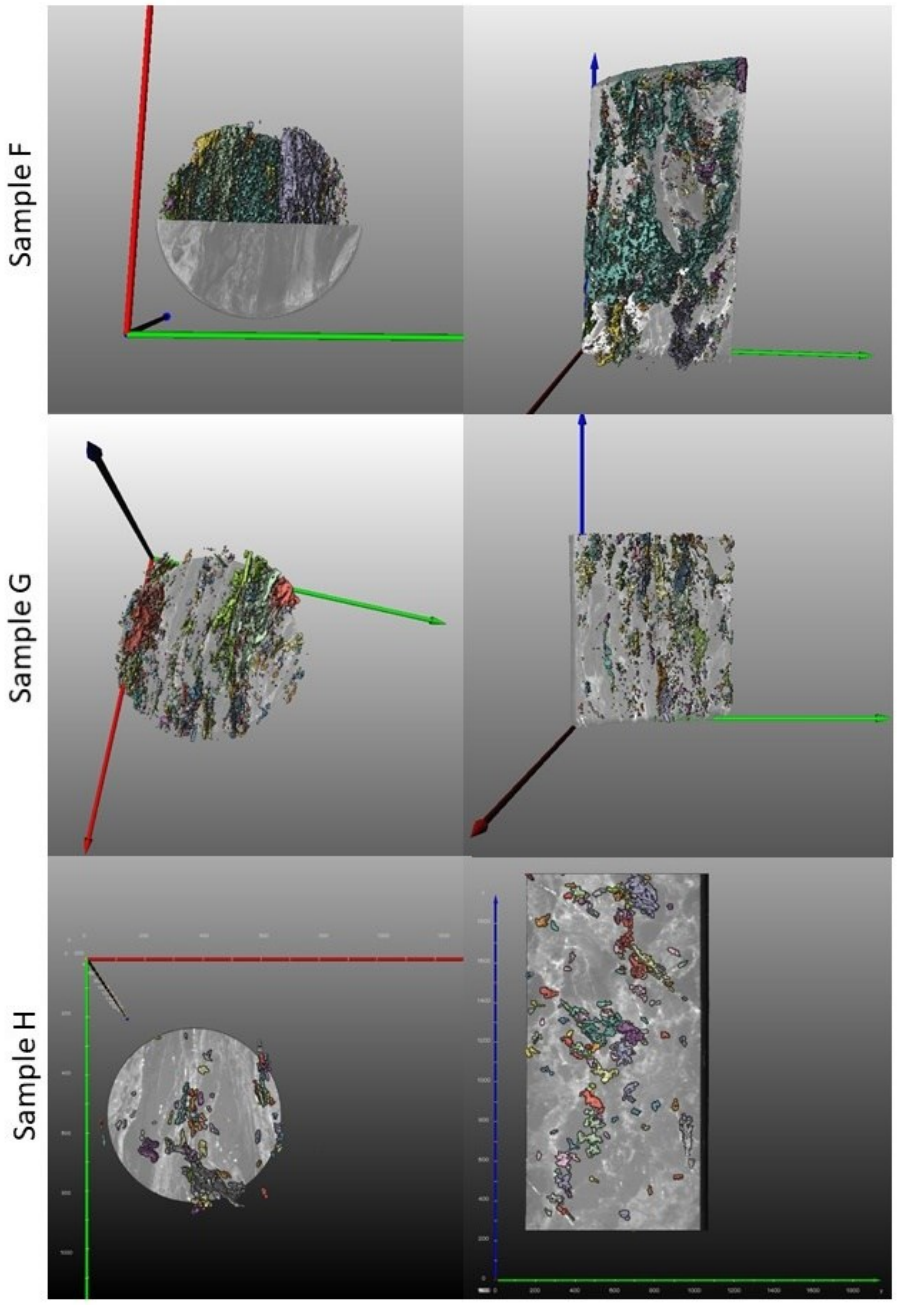

Figure 6.5 Mylonite 3d section. Blue axis =z; red axis= x and green axis =y of the Avizo™ reference system.

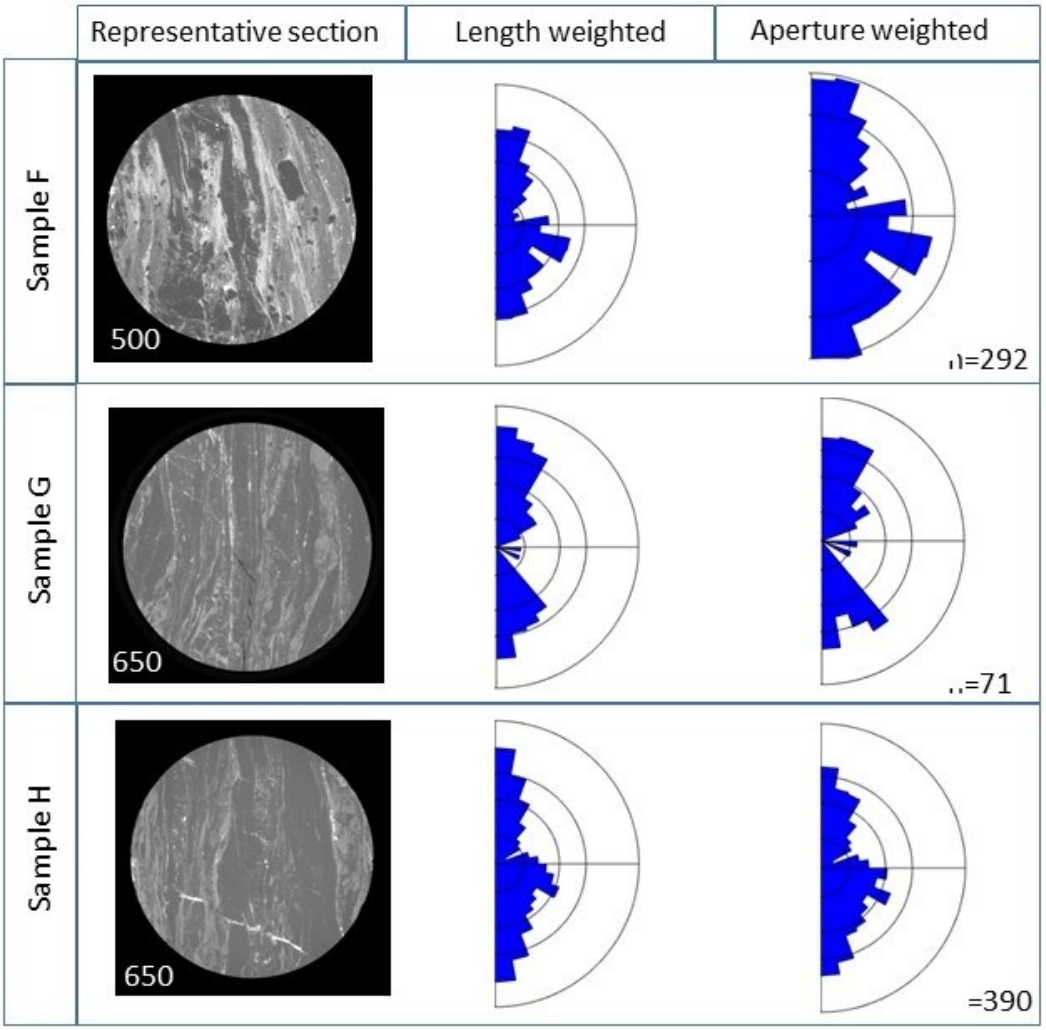

Figure 6.6 Orientation of chlorites for the mylonitic samples.. Images present the 2D orientation (in the XY plane) obtained for each sample in the mylonite. XY orthoslices are used whenever possible, to assess cross cutting relationship between veins and foliation trace.

6.3.2 Cataclasite (Sample E)

Cataclasites in Fault Zone BFZ045 are identified from the relative abundance of chlorite in hand samples, and are characterized by the occurrence of numerous chlorites fractures and bands of white mica (sample PH28_22, Fig 6.7a). Sample E has a foliated cataclastic texture with angular clasts surrounded by a fine-grained matrix composed of plagioclase, chlorite and white mica (e.g. Fig.6.7 c). Quartz-chlorite in the fracture in the cataclasite present syntaxial growth and lamellar habit, with crystals aligned perpendicular or slightly off-normal to the vein wall crystals (Fig 6.7 b). Chlorites in the

matrix (Fig 6.7c), have a texture that varies from flaky to massive. Locally, chlorite lamellae in the chlorite-quartz fractures are elongated parallel to the stretching lineation and at a high angle to the fracture wall (Fig. 6.7 d,e). Mostly chlorite-quartz fracture shows Mode I aperture (Fig. 6.7f) but occurs also as hybrid fracture interesting domino type fragmented clasts (Fig.6.7g). Separation of chlorites filled fractures in the cataclastic domain was not attempted, due to the prevalence of chlorite in the matrix.

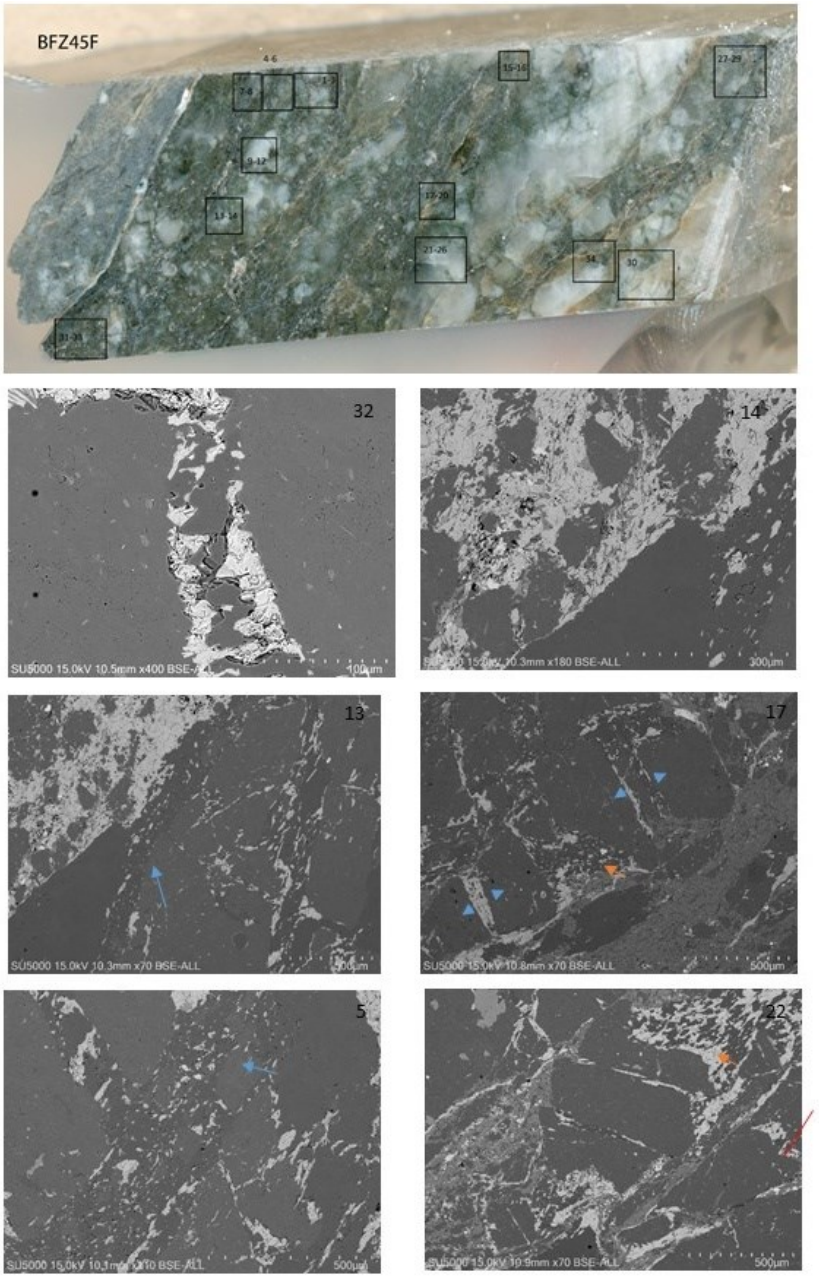

Figure 6.7 Chlorites in the cataclasite. SEM images

6.3.3 Damage zone

In the damage zone presence of chlorite-quartz fractures have been observed for only two sample (Samples B and E). In sample B chlorite-quartz veins forms a characteristic triangular texture, which is commonly associated with infilling of hydraulically brecciated rock, resembling a 'crackle breccia' style texture (Woodcock and Mort, 2008) (Fig 6.8a). Chlorite is showing syntaxial growth. For sample E the observed chlorite-quartz fracture cuts the mylonitic foliation at the contact with the cataclasite (Fig 6.8b) Chlorite grows radially from the fracture walls and intergrown quartz shows undulose extinction. Chlorite lined fractures are prevalent and are observed from thin extensional veins with aperture widths ~40-100 μm, to larger veins (up to ~400 μm aperture widths) with flaky texture (Fig 6.8 c-e). Chlorite is also present lining shear fractures, presenting a fine-grained fibrous habit parallel to the shear direction (Fig 6.8 f).

In samples from the damage zone, chlorite fractures appear either as homogeneous cataclastic band or as fractures (Fig 6.9). Cataclastic bands tend to have orientation semi parallel to the foliation (e.g Sample B Fig. 6.9). Chlorite fractures shows cross cutting relationship with small angles between fracture sets, however it was difficult to discern whether a specific orientation cuts another (e.g Sample B,C Fig. 6.9)

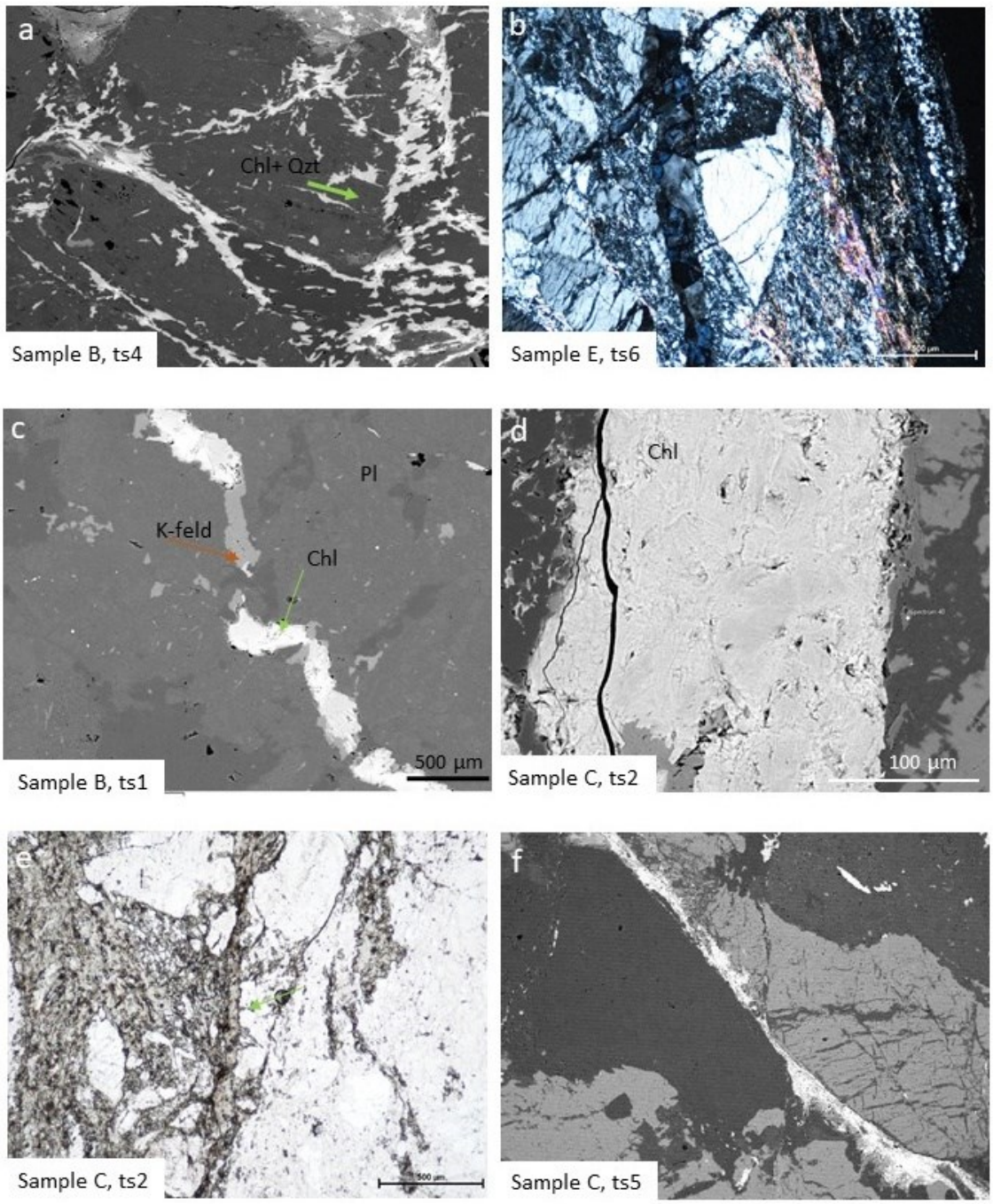

Figure 6.8 Chlorites in the damage zone. SEM images

Most of the traced chlorite-filled fractures are oriented sub-parallel to the foliation (Fig.6.9). Damage zone fractures can be separated based on the orientations determined in the segmented images: Sample A with trend parallel to foliation trace, sample B more homogenous, C- E with a trend toward 140-160 degrees angles to the foliation trace (Fig 6.9).

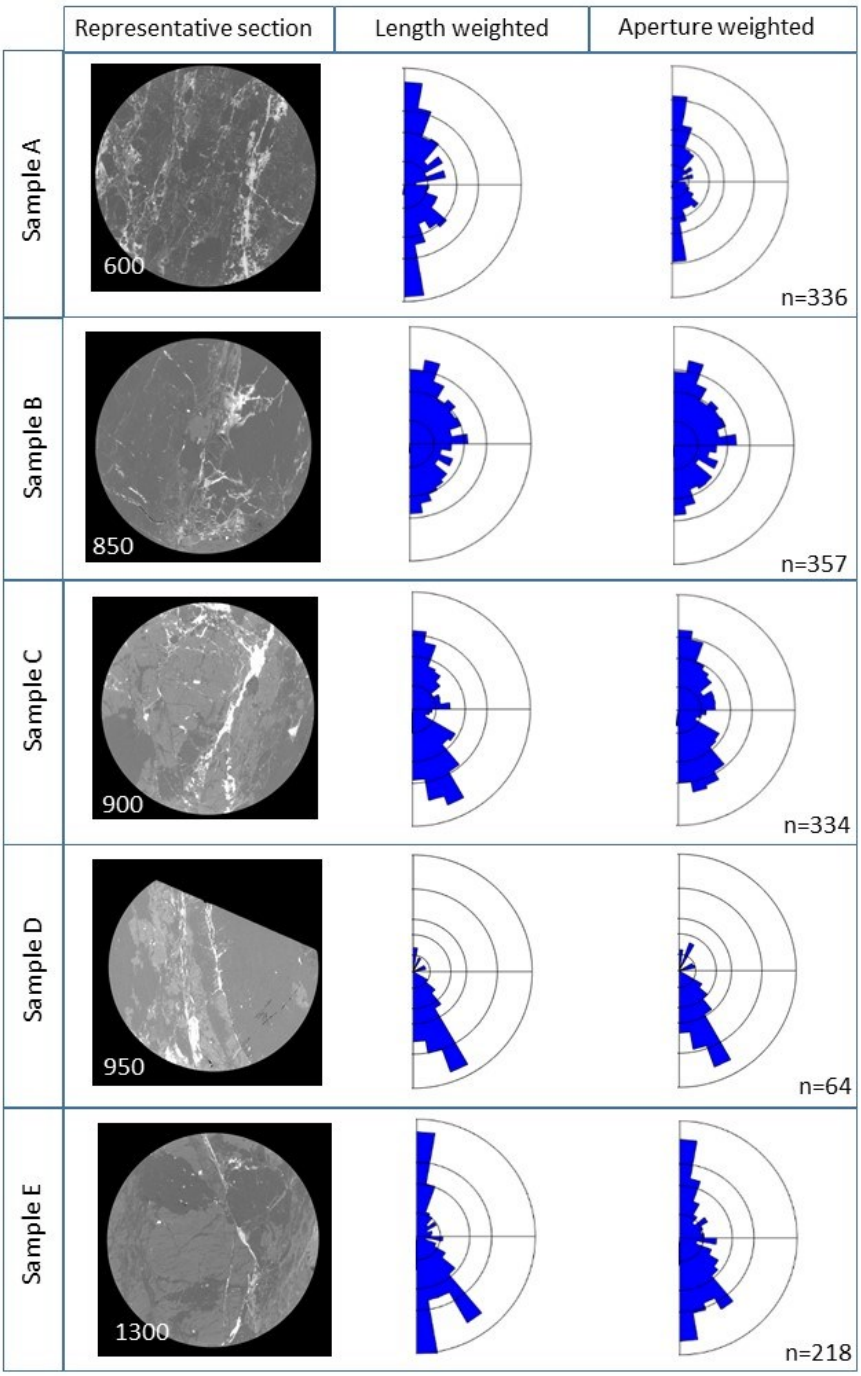

Figure 6.9 Damage zone fracture orientation. Images present the 2D orientation (in the XY plane) obtained for each sample in the damage zone. XY orthoslices are used whenever possible, to assess cross cutting relationship between veins and foliation trace.

6.4 Discussion

6.4.1 Distribution along fault

Mylonite (samples F.G and H, Fig 6.10) are characterised by a mix of both chlorite-lined fractures and quartz-chlorite filled fractures. Quartz-chlorite fractures appear to develop as dominantly mode I veins, oriented subparallel to the mylonitic foliation. Opening of the mode I extensional fractures parallel to the foliation could indicate a local variation on stress orientation due to elevated pore fluid pressure (Cox, 2005). Recrystallized quartz veins were observed with similar orientation in other samples of the BFZ045 (Chapter 4).

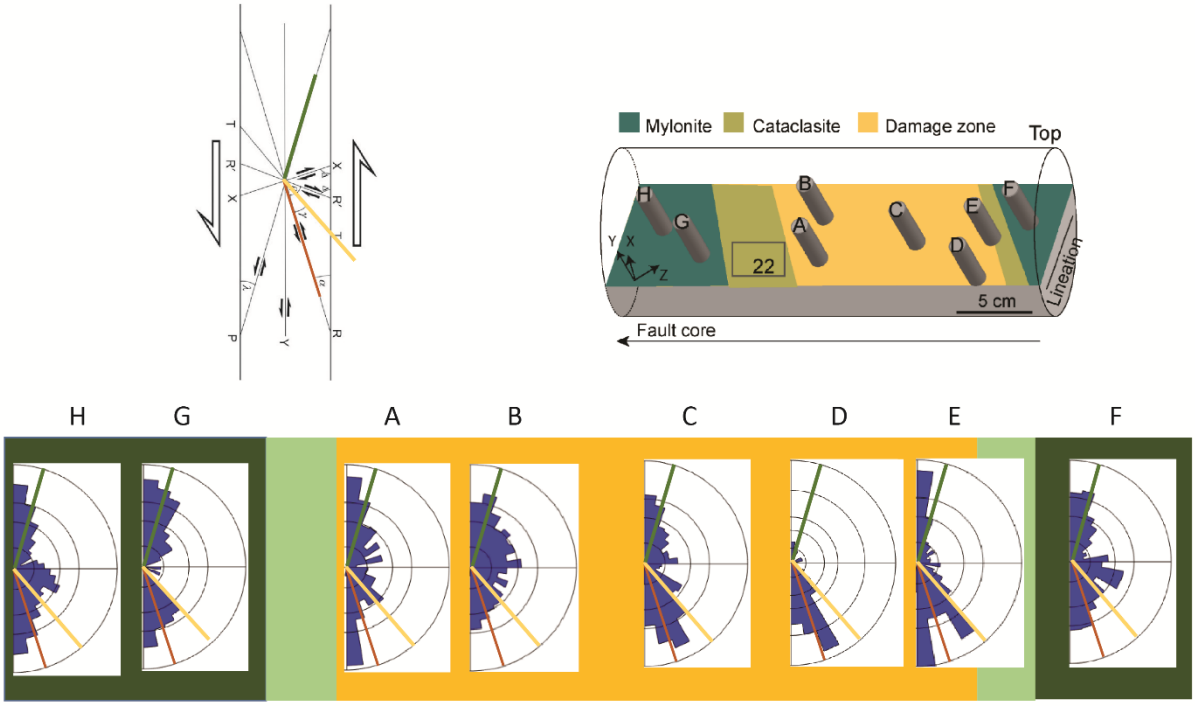

Figure 6.10 Distribution of sample orientation along fault

Chlorite filled fractures while also showing a preferred orientation parallel to foliation, presents a secondary orientation trending at ca. 140° to the foliation plane. Fractures

with the widest apertures are mostly oriented at 140-150°, forming angles of around 20-40° with the foliation plane. Assuming homogenous stress states in the crust and Coulomb failure behaviour following the Anderson model of faulting, the earliest fracture to form under brittle condition are expected at angles of ~25-30 with respect to the maximum principal stress driving the deformation (Anderson, 1942; Scholz, 2002). From Olkiluoto regional studies, it is assumed that the ductile precursor of BFZ045 was optimally oriented for the reactivation during the first stage of brittle deformation (Mattila and Viola, 2014). Chlorite secondary orientation trending at ca. 150° to the foliation plane could be consistent with R fractures for a sinistral fault (Fig 6.10).

The damage zone contrast with the mylonite in that they present dominantly chlorite filled fractures with variable orientations. Microstructural observations in the damage zone and neighbouring cataclasite zone identified chlorite filled veins having mostly extensional component, however present a component of shear.

In the cataclasite elongation, in quartz-chlorite veins, of chlorite lamellae parallel to the precursor foliation trace and dissolution-precipitation of quartz and chlorite in clast pressure shadows might suggest that ductile condition was still present during part of the cataclastic deformation.

While more detailed analysis of the data in regards of the fracture orientation, separated by fracture opening mode is needed to better understand the presented data, some preliminary points of discussion can be identified:

1. Regional studies of the Olkiluoto region propose the development of N-S faults due to the linkage of individual fault segments, which exploited the anastomosing network of shear zones related to a late stage of ductile deformation (D4). From microstructural observation there are evidence that the onset of brittle deformation in Olkiluoto was driven by multiple crack and seals

events of due to fluids overpressure, seen both in BFZ045 (Prando et al., 2020), and more evidently in the conjugated fault BFZ300 (Marchesini et al, 2019).

2. Ductile precursor of BFZ045, most clearly represented by the main mylonitic foliation, did play a role in the localization of brittle deformation. Possibly acting either as a fluid barrier or as a fluid pump (Fusseis et al., 2009) leading to a local variation of fluid pressure, and in turn promoting brittle failure (Sibson, 1990; Gratier et al., 2003). Quartz-chlorite fractures observed in the studied samples of BFZ045 present microstructures and geometries indicative of a fluid driven origin, through hydro fracturing (e.g., crackle breccia' style texture (Woodcock and Mort, 2008)), and could be used as evidence of a temporary permeability.
3. Precipitation of minerals, such as chlorite, in the fractures, under ductile condition, could result in an overall weakening under subsequent brittle deformation (reduced coefficient of sliding friction and/or cohesion). Preferred orientation of phyllosilicates along foliation, as seen in the cataclasite samples, could also impact the strength of early formed structures during later brittle deformation. Subsequent fracturing under ductile-brittle transition could then have been controlled from the interplay of regional stress orientation, for which the ductile precursor was optimally oriented (Mattila and Viola, 2014), and the presence of fluids. This may explain why observed fracture are oriented parallel and at ca. 140° to the foliation. Linkage of different fracture sets could have then evolved into the development of cataclasite under brittle conditions.

6.4.2 Summary

The core section studied presents two main type fractures: hybrid shear fractures lined with chlorite and extensional (mode I) fractures under the guise of chlorite and quartz-chlorite fractures. Orientation analysis revealed that fractures are predominantly developed along the mylonitic foliation, or at angles to the foliation consistent with orientations expected for R and T Riedel shears in a sinistral strike slip fault zone. Quartz-chlorite fractures are considered to reflect hydro-fracturing and have been observed mostly along the mylonitic foliation and as part of clasts in the cataclasite. Chlorite fractures overall have more variability of texture and orientation in comparison to the quartz-chlorite veins.

7 Conclusions

This thesis aimed to characterise the onset of brittle deformation under ductile conditions that define part of the long deformation history of BFZ045, a brittle fault zone exploiting a mylonitic precursor in the Paleoproterozoic basement in Olkiluoto, SW Finland. Major focus of the thesis was the study of deformation mechanisms and fluid pathways representative of the mechanical evolution of BFZ045 at the transition from ductile to brittle deformation. A multimethod approach was used to investigate the deformation mechanism and semi-quantify parameters that defined the fault evolution.

Fault zone geometry shows a cataclastic core that overprints the pre-existing mylonitic core structures. The presence of syn-kynematic quartz veins, which are in turn characterised by dynamic recrystallization with quartz grains undergoing subgrain rotation, suggests that the fault zone underwent transient brittle events under overall ductile conditions. Mylonitization of BFZ045 has been estimated to occur at ~450 C and 3.5 Kbar, corresponding to a depth of faulting at 13 km in the crust that locates the strike slip fault in the seismogenic zone.

Mylonitic creep occurred under increased differential stresses towards the shear zone centre and is presented as microscopic-scale complementary evidence of what had been previously observed at a larger scale: the discontinuous high-strain ductile structural elements that have been described to have strongly contributed to the localization of N-S sub-vertical faults during a late ductile deformation event in Olkiluoto (Skyttä and Torvela 2018).

The observation of fluid-related microstructures, together with the variation of differential stresses along the fault core section, shaped the proposed conceptual model of the evolution of BFZ045 slip behaviour. The model highlights the significant role of

transiently sub-lithostatic fluid pressure in triggering vein emplacement during ongoing mylonitic deformation, as well as the progressive increase in stress and strain rate during viscous creep towards peak conditions reached at the BDTZ in the BFZ045.

Reported microstructural observations indicate that pore fluid pressure played a crucial role in veins emplacement and deformation in the BFZ045, further research was aimed at characterising fluid pathways at different scales and their impact on the overall evolution of the BFZ045.

The results showed minimal variations in porosity distribution along the fault core, indicating that different porosity-generating and porosity-sealing mechanisms played a role in controlling porosity variation within different fault rocks.

The pore volumes obtained along the BFZ045 fault rocks are representative of its long deformation history. Overall low pore volume estimates for the mylonitic precursor might suggest its limited capacity to permit fluid flow capacity. This finding complements several permeability studies conducted in Olkiluoto, as the most permeable structures have been indicated to be fractures and fault zones within the Olkiluoto bedrock (Baxter et al., 2021). Multimethod approach was helpful to investigate pores at different scales and interpret volumetric measurements obtained from He-pycnometry and MIP in relationship to microstructural observation from SEM images and 3D porosity distribution from µ-CT data.

The presence of chlorite and quartz-chlorite filled fractures suggests that fluid-rock interactions played a significant role in their formation and evolution. Quartz-chlorite fractures have been interpreted to be mostly formed through process of hydro-fracturing, indicate that fluid infiltration and fluid pressure fluctuations were likely present during the faulting process. Additionally, the observed orientation of chlorites

lamellae filling the fractures coupled with quartz recrystallization evidence suggests that part of the formation of the described fracture occurred under partially ductile condition during the BFZ045 deformation history. Orientation analysis has shown that chlorite filled fractures predominantly developed along the mylonitic foliation, or at angles to the foliation consistent with orientations expected for R and T Riedel shears in a sinistral strike slip fault zone. Chlorite fractures overall have more variability of texture and orientation in comparison to the quartz-chlorite veins. The presence of chlorite fractures parallel to the mylonitic foliation indicates that they either may have formed during the mylonitization process, or that the mylonitic foliation acted as a preferred plane of weakness during the fault deformation history. Overall, the different textures and orientations of chlorite fractures suggest a more complex formation history compared to the quartz-chlorite veins. Limitations of the presented findings, such as missing age constrain, clear cross cutting relationship and composition analysis of the chlorite fractures represent a direction for future studies that could be applied for a better understanding of the events controlling the fracture formations in Olkiluoto. Moreover, the small size of the sample may not accurately represent the entire fracture population or elude cross cutting relationship. Future works should be expanded to add the rich dataset of fracture available for ONKALO underground mapping, therefore closing the gap from the existing micro and the regional scale analysis of fracture and fault zone orientations in Olkiluoto.

The key outcome of this thesis is the recognition of the importance of BFZ045 ductile precursor role in influencing the fault behaviour during its evolutionary history at seismogenic depth. This study shows that microstructural studies leading to the acquisition of independent constraints offer the potential to reconstruct in detail the evolutionary history of fault zones that experienced a transition in deformation mode at the BDTZ. Overall, the applied multimethod approach gives complementary

information on parameters that were in play at the onset of brittle deformation in Olkiluoto.

In addition to deriving a conceptual model of varying fault slip behaviours at the BDTZ, the methods and the results of this work complement and expand thorough site characterization studies of deep geological disposal facilities. In the case of Olkiluoto, detailed study of a continuous fault section from drill core samples contributed to a better understanding of Fault system I behaviour, that is part of the long and complex history deformation of the area, which might not have been fully grasped just from regional, larger scale studies.

References

Aaltonen, I., Engström, J., Gehör, S., Kosunen, P., Kärki, A., 2016. Geology of Olkiluoto. Posiva Work. Rep. 2016-16 Posiva Oy Eurajoki.

Aaltonen, I., Lahti, M., Engström, J., Mattila, J., Paananen, M., Paulamäki, S., Gehör, S., Kärki, A., Ahokas, T., Torvela, T., Front, K., 2010. Geological Model of the Olkiluoto Site. Version 2.0. Posiva Work. Rep. 2010-70 Posiva Oy Eurajoki.

Anderson, E. M., 1942. The Dynamics of Faulting and Dyke Formation with Applications to Britain. Edinburgh: Oliver & Boyd Ltd.

Anovitz, L.M., Cole, D.R., 2015. Characterization and Analysis of Porosity and Pore Structures. Rev. Mineral. Geochem. 80, 61–164. https://doi.org/10.2138/rmg.2015.80.04

Aoya, M., Kouketsu, Y., Endo, S., Shimizu, H., Mizukami, T., Nakamura, D., Wallis, S., 2010a. Extending the applicability of the Raman carbonaceous-material geothermometer using data from contact metamorphic rocks. J. Metamorph. Geol. 28, 895–914. https://doi.org/10.1111/j.1525-1314.2010.00896.x

Arganda-Carreras, I., Kaynig, V., Rueden, C., Eliceiri, K.W., Schindelin, J., Cardona, A., Sebastian Seung, H., 2017. Trainable Weka Segmentation: a machine learning tool for microscopy pixel classification. Bioinformatics 33, 2424–2426. https://doi.org/10.1093/bioinformatics/btx180

Austrheim, H., 2013. Fluid and deformation induced metamorphic processes around Moho beneath continent collision zones: Examples from the exposed root zone of the Caledonian mountain belt, W-Norway. Tectonophysics, Moho: 100 years after Andrija Mohorovicic 609, 620–635. https://doi.org/10.1016/j.tecto.2013.08.030

Barker, S.L.L., Cox, S.F., Eggins, S.M., Gagan, M.K., 2006. Microchemical evidence for episodic growth of antitaxial veins during fracture-controlled fluid flow. Earth Planet. Sci. Lett. 250, 331–344. https://doi.org/10.1016/j.epsl.2006.07.051

Barker, S.L.L., Bennett, V.C., Cox, S.F., Norman, M.D., Gagan, M.K., 2009. Sm–Nd, Sr, C and O isotope systematics in hydrothermal calcite–fluorite veins: Implications for fluid–rock reaction and geochronology. Chem. Geol. 268, 58–66. https://doi.org/10.1016/j.chemgeo.2009.07.009

Baker, D. R., L. Mancini, M. Polacci, M. D. Higgins, G. A. R. Gualda, R. J. Hill, and M. Rivers (2012). “An introduction to the application of X-ray microtomography to the threedimensional study of igneous rocks”. In: Lithos 148, pp. 262–276. DOI: 10.1016/j.lithos.2012.06.008.

Barnhoorn, A., Cox, S.F., Robinson, D.J., Senden, T., 2010. Stress- and fluid-driven failure during fracture array growth: Implications for coupled deformation and fluid flow in the crust. Geology 38, 779–782. https://doi.org/10.1130/G31010.1

Baxter, S., Bym, T., Doe, T., Hartley, L., Libby, S., Shi, C.;2021. Alternative Conceptual Models for Flow and Transport in Olkiluoto Fracture Systems. Working Report, 2021-15, Posiva Oy

Behr, W.M., Platt, J.P., 2011. A naturally constrained stress profile through the middle crust in an extensional terrane. Earth Planet. Sci. Lett. 303, 181–192. https://doi.org/10.1016/j.epsl.2010.11.044

Belgrano, T.M., Herwegh, M., Berger, A., 2016. Inherited structural controls on fault geometry, architecture and hydrothermal activity: an example from Grimsel Pass, Switzerland. Swiss J. Geosci. 109, 345–364. https://doi.org/10.1007/s00015-016-0212-9

Berg, S., Saxena, N., Shaik, M., and Pradhan, C.: Generation of ground truth images to validate micro-CT image-processing pipelines, https://doi.org/10.1190/tle37060412.1, 2018.

Bestmann, M., Prior, D.J., 2003. Intragranular dynamic recrystallization in naturally deformed calcite marble: diffusion accommodated grain boundary sliding as a result of subgrain rotation recrystallization. J. Struct. Geol. 25, 1597–1613. https://doi.org/10.1016/S0191-8141(03)00006-3

Beyssac, O., Goffé, B., Chopin, C., Rouzaud, J.N., 2002. Raman spectra of carbonaceous material in metasediments: a new geothermometer. J. Metamorph. Geol. 20, 859–871. https://doi.org/10.1046/j.1525-1314.2002.00408.x

Billia, M.A., 2013. Grain boundary dissolution porosity in quartzofeldspathic ultramylonites: Implications for permeability enhancement and weakening of mid-crustal shear zones. J. Struct. Geol. 13.

Blenkinsop, T.G., 2007. Deformation Microstructures and Mechanisms in Minerals and Rocks. Springer Science & Business Media.

Blenkinsop, T.G., Oliver, N.H.S., Dirks, P.G.H.M., Nugus, M., Tripp, G., Sanislav, I., 2020. Chapter 1: Structural Geology Applied to the Evaluation of Hydrothermal Gold Deposits, in: Rowland, J.V., Rhys, D.A. (Eds.), APPLIED STRUCTURAL GEOLOGY OF ORE-FORMING HYDROTHERMAL SYSTEMS. Society of Economic Geologists, p. 0. https://doi.org/10.5382/rev.21.01

Bons, P.D., 2000. The formation of veins and their microstructures. J. Virtual Explor. 02. https://doi.org/10.3809/jvirtex.2000.00007

Bons, P.D., Elburg, M.A., Gomez-Rivas, E., 2012. A review of the formation of tectonic veins and their microstructures. J. Struct. Geol. 43, 33–62. https://doi.org/10.1016/j.jsg.2012.07.005

Bos, B., Spiers, C.J., 2002. Frictional-viscous flow of phyllosilicate-bearing fault rock: Microphysical model and implications for crustal strength profiles. J. Geophys. Res. Solid Earth 107, ECV 1-1-ECV 1-13. https://doi.org/10.1029/2001JB000301

Byerlee, J., 1978. Friction of rocks. Pure Appl. Geophys. 116, 615–626. https://doi.org/10.1007/BF00876528

Caine, J.S., Evans, J.P., Forster, C.B., 1996. Fault zone architecture and permeability structure. Geology 24, 1025–1028. https://doi.org/10.1130/0091-7613(1996)024<1025:FZAAPS>2.3.CO;2

Ceccato, A., Menegon, L., Pennacchioni, G., Morales, L.F.G., 2018. Myrmekite and strain weakening in granitoid mylonites. Solid Earth 9, 1399–1419. https://doi.org/10.5194/se-9-1399-2018

Cnudde, V., Cwirzen, A., Masschaele, B., Jacobs, P.J.S., 2009. Porosity and microstructure characterization of building stones and concretes. Eng. Geol., Applications of X-ray Computed Tomography in Engineering Geology 103, 76–83. https://doi.org/10.1016/j.enggeo.2008.06.014

Cnudde V, Boone M. High-resolution X-ray computed tomography in geosciences: a review of the current technology and applications. EARTH-SCIENCE REVIEWS. 2013;123:1–17.

Connolly, J.A.D., 2010. The Mechanics of Metamorphic Fluid Expulsion. Elements 6, 165–172. https://doi.org/10.2113/gselements.6.3.165

Cox, S.F., Wall, V.J., Etheridge, M.A., Potter, T.F., 1991. Deformational and metamorphic processes in the formation of mesothermal vein-hosted gold deposits — examples from the Lachlan Fold Belt in central Victoria, Australia. Ore Geol. Rev., Ores and Metamorphism 6, 391–423. https://doi.org/10.1016/0169-1368(91)90038-9

Cox, S.F., 1995. Faulting processes at high fluid pressures: An example of fault valve behavior from the Wattle Gully Fault, Victoria, Australia. J. Geophys. Res. Solid Earth 100, 12841–12859. https://doi.org/10.1029/95JB00915

Cox, S.F., 1999. Deformational controls on the dynamics of fluid flow in mesothermal gold systems. Geol. Soc. Lond. Spec. Publ. 155, 123–140. https://doi.org/10.1144/GSL.SP.1999.155.01.10

Cox, S.F., Knackstedt, M.A., Braun, J., 2001. Principles of Structural Control on Permeability and Fluid Flow in Hydrothermal Systems, in: Richards, J.P., Tosdal, R.M. (Eds.), Structural Controls on Ore Genesis. Society of Economic Geologists, p. 0. https://doi.org/10.5382/Rev.14.01

Cox, S.F., 2002. Fluid flow in mid-to deep crustal shear systems: Experimental constraints, observations on exhumed high fluid flux shear systems, and implications for seismogenic processes. Earth Planets Space 54, 1121–1125. https://doi.org/10.1186/BF03353312

Cox, S.F., 2005. Coupling between Deformation, Fluid Pressures, and Fluid Flow in Ore-Producing Hydrothermal Systems at Depth in the Crust, in: Hedenquist, J.W., Thompson, J.F.H., Goldfarb, R.J., Richards, J.P. (Eds.), One Hundredth Anniversary Volume. Society of Economic Geologists, p. 0. https://doi.org/10.5382/AV100.04

Cox, S.F., 2007. Structural and isotopic constraints on fluid flow regimes and fluid pathways during upper crustal deformation: An example from the Taemas area of the

Lachlan Orogen, SE Australia. J. Geophys. Res. Solid Earth 112. https://doi.org/10.1029/2006JB004734

Cox, S.F., 2010. The application of failure mode diagrams for exploring the roles of fluid pressure and stress states in controlling styles of fracture-controlled permeability enhancement in faults and shear zones. Geofluids. https://doi.org/10.1111/j.1468-8123.2010.00281.x

Cross, A.J., Prior, D.J., Stipp, M., Kidder, S., 2017. The recrystallized grain size piezometer for quartz: An EBSD-based calibration: EBSD-Based Quartz Grain Size Piezometer. Geophys. Res. Lett. 44, 6667–6674. https://doi.org/10.1002/2017GL073836

Derez, T., Pennock, G., Drury, M., Sintubin, M., 2015. Low-temperature intracrystalline deformation microstructures in quartz. J. Struct. Geol., Special Issue: Deformation of the lithosphere -How small structures tell a big story 71, 3–23. https://doi.org/10.1016/j.jsg.2014.07.015

Drelich, J.W., Boinovich, L., Chibowski, E., Della Volpe, C., Hołysz, L., Marmur, A., Siboni, S., 2020. Contact angles: history of over 200 years of open questions. Surf. Innov. 8, 3–27. https://doi.org/10.1680/jsuin.19.00007

Dunlap, W.J., Hirth, G., Teyssier, C., 1997. Thermomechanical evolution of a ductile duplex. Tectonics 16, 983–1000. https://doi.org/10.1029/97TC00614

Eberlei, T., Habler, G., Grasemann, B., Abart, R., 2014. Upper–greenschist facies intragrain deformation of albite in mylonitic meta–pegmatite and the influence of crystallographic anisotropy on microstructure formation. J. Struct. Geol. 69, 47–58. https://doi.org/10.1016/j.jsg.2014.10.001

Egli, D., Baumann, R., Küng, S., Berger, A., Baron, L., Herwegh, M., 2018. Structural characteristics, bulk porosity and evolution of an exhumed long-lived hydrothermal system. Tectonophysics 747–748, 239–258. https://doi.org/10.1016/j.tecto.2018.10.008

Elburg, M.A., Bons, P.D., Foden, J., Passchier, C.W., 2002. The origin of fibrous veins: constraints from geochemistry. Geol. Soc. Lond. Spec. Publ. 200, 103–118. https://doi.org/10.1144/GSL.SP.2001.200.01.07

Elminen, T., Zwingmann, H., Kaakinen, A., 2018. Constraining the timing of brittle deformation and sedimentation in southern Finland: Implications for Neoproterozoic evolution of the eastern Fennoscandian shield. Precambrian Res. 304, 110–124. https://doi.org/10.1016/j.precamres.2017.10.014

Engvik, A.K., Putnis, A., Fitz Gerald, J.D., Austrheim, H., 2008. ALBITIZATION OF GRANITIC ROCKS: THE MECHANISM OF REPLACEMENT OF OLIGOCLASE BY ALBITE. Can. Mineral. 46, 1401–1415. https://doi.org/10.3749/canmin.46.6.1401

Evans, J.P., Forster, C.B., Goddard, J.V., 1997. Permeability of fault-related rocks, and implications for hydraulic structure of fault zones. J. Struct. Geol. 19, 1393–1404. https://doi.org/10.1016/S0191-8141(97)00057-6

Faulkner, D.R., Jackson, C.A.L., Lunn, R.J., Schlische, R.W., Shipton, Z.K., Wibberley, C.A.J., Withjack, M.O., 2010. A review of recent developments concerning the structure, mechanics and fluid flow properties of fault zones. J. Struct. Geol., Fault Zones 32, 1557–1575. https://doi.org/10.1016/j.jsg.2010.06.009

Faulkner, D.R., Mitchell, T.M., Jensen, E., Cembrano, J., 2011. Scaling of fault damage zones with displacement and the implications for fault growth processes. J. Geophys. Res.-Solid Earth, 116.

Fisher, D.M., Brantley, S.L., Everett, M., Dzvonik, J., 1995. Cyclic fluid flow through a regionally extensive fracture network within the Kodiak accretionary prism. J. Geophys. Res. Solid Earth 100, 12881–12894. https://doi.org/10.1029/94JB02816

Fitz Gerald, J.D., Stünitz, H., 1993. Deformation of granitoids at low metamorphic grade. I: Reactions and grain size reduction. Tectonophysics 221, 269–297. https://doi.org/10.1016/0040-1951(93)90163-E

Fossen, H., Cavalcante, G.C.G., 2017. Shear zones – A review. Earth-Sci. Rev. 171, 434–455. https://doi.org/10.1016/j.earscirev.2017.05.002

Freeman, J.J., Wang, A., Kuebler, K.E., Jolliff, B.L., Haskin, L.A., 2008. Characterization of natural feldspars by Raman spectroscopy for future planetary exploration. Can. Mineral. 46, 1477–1500.

Frelinger, S.N., Ledvina, M.D., Kyle, J.R. and Zhao, D., 2015. Scanning electron microscopy cathodoluminescence of quartz: Principles, techniques and applications in ore geology. Ore Geology Reviews, 65, pp.840-852.

Fusseis, F., Handy, M.R., 2008. Micromechanisms of shear zone propagation at the brittle–viscous transition. J. Struct. Geol. 30, 1242–1253. https://doi.org/10.1016/j.jsg.2008.06.005

Fusseis, F., Regenauer-Lieb, K., Liu, J., Hough, R.M., De Carlo, F., 2009. Creep cavitation can establish a dynamic granular fluid pump in ductile shear zones. Nature 459, 974–977. https://doi.org/10.1038/nature08051

Fusseis, F., Xiao, X., Schrank, C., and De Carlo, F.: A brief guide to synchrotron radiation-based microtomography in (structural) geology and rock mechanics, J. Struct. Geol., 65, 1–16, https://doi.org/10.1016/j.jsg.2014.02.005, 2014.

Géraud, Y., Caron, J., Faure, P., 1995. Porosity network of a ductile shear zone. J. Struct. Geol. 17, 1757–1769. https://doi.org/10.1016/0191-8141(95)00067-N

Giesche, H.: Mercury Porosimetry: A General (Practical) Overview, Part. Part. Syst. Charact., 23, 9–19, https://doi.org/10.1002/ppsc.200601009, 2006.

Giger, S.B., Tenthorey, E., Cox, S.F., Fitz Gerald, J.D., 2007. Permeability evolution in quartz fault gouges under hydrothermal conditions. J. Geophys. Res. 112, B07202. https://doi.org/10.1029/2006JB004828

Gilgannon, J., Fusseis, F., Menegon, L., Regenauer-Lieb, K., Buckman, J., 2017. Hierarchical creep cavity formation in an ultramylonite and implications for phase mixing. Solid Earth 8, 1193–1209. https://doi.org/10.5194/se-8-1193-2017

Gilgannon, J., Poulet, T., Berger, A., Barnhoorn, A., Herwegh, M., 2020. Dynamic Recrystallization Can Produce Porosity in Shear Zones. Geophys. Res. Lett. 47, e2019GL086172. https://doi.org/10.1029/2019GL086172

Giuntoli, F., Menegon, L., Warren, C.J., 2018. Replacement reactions and deformation by dissolution and precipitation processes in amphibolites. J. Metamorph. Geol. 36, 1263–1286. https://doi.org/10.1111/jmg.12445

Goldstein JI, Newbury DE, Michael JR, Ritchie NW, Scott JH, Joy DC. Scanning electron microscopy and X-ray microanalysis. Springer; 2017 Nov 17.

Gomila, R., Arancibia, G., Mery, D., Nehler, M., Bracke, R., Morata, D., 2019. Palaeopermeability anisotropy and geometrical properties of sealed-microfractures from micro-CT analyses: An open-source implementation. Micron 117, 29–39. https://doi.org/10.1016/j.micron.2018.11.001

Gomila, R., Arancibia, G., Mitchell, T.M., Cembrano, J.M., Faulkner, D.R., 2016. Palaeopermeability structure within fault-damage zones: A snap-shot from microfracture analyses in a strike-slip system. J. Struct. Geol. 83, 103–120. https://doi.org/10.1016/j.jsg.2015.12.002

Gratier, J.-P., Favreau, P., Renard, F., 2003. Modeling fluid transfer along California faults when integrating pressure solution crack sealing and compaction processes. J. Geophys. Res. Solid Earth 108. https://doi.org/10.1029/2001JB000380

Gratier, J.-P., Gueydan, F., 2007. Deformation in the Presence of Fluids and Mineral Reactions Effect of Fracturing and Fluid–Rock Interaction on Seismic Cycles. pp. 319–356.

Gudmundsson, A., 2022. The propagation paths of fluid-driven fractures in layered and faulted rocks. Geol. Mag. https://doi.org/10.1017/S0016756822000826

Gueydan, F., Leroy, Y.M., Jolivet, L., Agard, P., 2003. Analysis of continental midcrustal strain localization induced by microfracturing and reaction-softening. J. Geophys. Res. Solid Earth 108. https://doi.org/10.1029/2001JB000611

Guntoro, P. I., Ghorbani, Y., Koch, P.-H., and Rosenkranz, J.: X-ray Microcomputed Tomography (μCT) for Mineral Characterization: A Review of Data Analysis Methods, Minerals, 9, 183, https://doi.org/10.3390/min9030183, 2019.

Gürsoy, D., F. De Carlo, X. Xiao, and C. Jacobsen (2014). “TomoPy: a framework for the analysis of synchrotron tomographic data.” In: Journal of synchrotron radiation 21.Pt 5, pp. 1188–93. DOI: 10.1107/S1600577514013939.

Halisch, M., Steeb, H., Henkel, S., Krawczyk, C.M., 2016. Pore-scale tomography and imaging: applications, techniques and recommended practice. Solid Earth 7, 1141–1143. https://doi.org/10.5194/se-7-1141-2016

Handy, M.R., Brun, J.-P., 2004. Seismicity, structure and strength of the continental lithosphere. Earth Planet. Sci. Lett. 223, 427–441. https://doi.org/10.1016/j.epsl.2004.04.021

Handy, M.R., Hirth, G., Hovius, N., 2007. Continental Fault Structure and Rheology from the Frictional-to-Viscous Transition Downward, in: Tectonic Faults: Agents of Change on a Dynamic Earth. MITP.

Healy, D., Rizzo, R.E., Cornwell, D.G., Farrell, N.J.C., Watkins, H., Timms, N.E., Gomez-Rivas, E., Smith, M., 2017. FracPaQ: A MATLABTM toolbox for the quantification of fracture patterns. J. Struct. Geol. 95, 1–16. https://doi.org/10.1016/j.jsg.2016.12.003

Heilbronner, R. and Barrett, S.: Image Analysis in Earth Sciences: Microstructures and Textures of Earth Materials, Springer Science & Business Media, 521 pp., 2013.

Heilbronner, R., Tullis, J., 2006. Evolution of c axis pole figures and grain size during dynamic recrystallization: Results from experimentally sheared quartzite. J. Geophys. Res. Solid Earth 111. https://doi.org/10.1029/2005JB004194

Hellmuth, K.-H., Lukkarinen, S., Siitari-kauppi, M., 1994. Rock Matrix Studies with Carbon-14-Polymethylmethacrylate (PMMA); Method Development and Applications. Isot. Isot. Environ. Health Stud. 30, 47–60. https://doi.org/10.1080/00211919408046712

Hellmuth, K.-H., Siitari-Kauppi, M., Klobes, P., Meyer, K., Goebbels, J., 1999. Imaging and analyzing rock porosity by autoradiography and Hg-porosimetry/X-ray computertomography—Applications. Phys. Chem. Earth Part Solid Earth Geod. 24, 569–573. https://doi.org/10.1016/S1464-1895(99)00081-2

Hellmuth, K.H., Siitari-Kauppi, M., Lindberg, A., 1993. Study of porosity and migration pathways in crystalline rock by impregnation with 14C-polymethylmethacrylate. J. Contam. Hydrol., Chemistry and Migration of Actinides and Fission Products 13, 403–418. https://doi.org/10.1016/0169-7722(93)90073-2

Hentschel, F., Trepmann, C.A., Janots, E., 2019. Deformation of feldspar at greenschist facies conditions – the record of mylonitic pegmatites from the Pfunderer Mountains, Eastern Alps. Solid Earth 10, 95–116. https://doi.org/10.5194/se-10-95-2019

Herwegh, M., Berger, A., 2004. Deformation mechanisms in second-phase affected microstructures and their energy balance. J. Struct. Geol. 26, 1483–1498. https://doi.org/10.1016/j.jsg.2003.10.006

Herwegh, M., Linckens, J., Ebert, A., Berger, A., Brodhag, S.H., 2011. The role of second phases for controlling microstructural evolution in polymineralic rocks: A review. J. Struct. Geol. 33, 1728–1750. https://doi.org/10.1016/j.jsg.2011.08.011

Hirth, G., Beeler, N.M., 2015. The role of fluid pressure on frictional behavior at the base of the seismogenic zone. Geology 43, 223–226. https://doi.org/10.1130/G36361.1

Hirth, G., Teyssier, C., Dunlap, J.W., 2001. An evaluation of quartzite flow laws based on comparisons between experimentally and naturally deformed rocks. Int. J. Earth Sci. 90, 77–87. https://doi.org/10.1007/s005310000152

Hirth, G., Tullis, J., 1992. Dislocation creep regimes in quartz aggregates. J. Struct. Geol. 14, 145–159. https://doi.org/10.1016/0191-8141(92)90053-Y

Hirth, G., Tullis, J., 1994. The brittle-plastic transition in experimentally deformed quartz aggregates. J. Geophys. Res. Solid Earth 99, 11731–11747. https://doi.org/10.1029/93JB02873

Hövelmann, J., Putnis, A., Geisler, T., Schmidt, B.C., Golla-Schindler, U., 2010. The replacement of plagioclase feldspars by albite: observations from hydrothermal experiments. Contrib. Mineral. Petrol. 159, 43–59. https://doi.org/10.1007/s00410-009-0415-4

Ikonen, J.O., Sammaljärvi, J.K.W., Siitari-Kauppi, M.K., Voutilainen, M.A., Lindberg, A., Kuva, J., Timonen, J., 2015. Investigation of Rock Matrix Retention Properties Supporting Laboratory Studies I: Mineralogy, Porosity, and Pore Structure, Working Report. Posiva, Olkiluoto.

Jacobsson, L., Flansbjer, M., Johannesson, P., Lindqvist, J., Brander, L., Schouenborg, B., 2016. ONKALO POSE Experiment - Geological and Rock Mechanical Tests on Samples from a Heating Test at Olkiluoto, Work reports 2016-18.

Jaques, V.A.J., Plessis, A.D., Zemek, M., Šalplachta, J., Stubianová, Z., Zikmund, T., Kaiser, J., 2021. Review of porosity uncertainty estimation methods in computed tomography dataset. Meas. Sci. Technol. 32, 122001. https://doi.org/10.1088/1361-6501/ac1b40

Karato, S.-I., 2008. Deformation of Earth Materials. An Introduction to the Rheology of Solid Earth. x + 463 pp. Cambridge, New York, Melbourne: Cambridge University Press.

Kärki, A., Paulamäki, S., 2006. Petrology of Olkiluoto. Posiva Work. Rep. 2006-02 Posiva Oy Eurajoki.

Ketcham, R. A. and Carlson, W. D.: Acquisition, optimization and interpretation of X-ray computed tomographic imagery: applications to the geosciences, 20, 2001.

Kidder, S., Hirth, G., Avouac, J.-P., Behr, W., 2016. The influence of stress history on the grain size and microstructure of experimentally deformed quartzite. J. Struct. Geol. 83, 194–206. https://doi.org/10.1016/j.jsg.2015.12.004

Kidder, S., Avouac, J.-P., Chan, Y.-C., 2012. Constraints from rocks in the Taiwan orogen on crustal stress levels and rheology. J. Geophys. Res. Solid Earth 117. https://doi.org/10.1029/2012JB009303

Kilian, R., Heilbronner, R., Stünitz, H., 2011. Quartz grain size reduction in a granitoid rock and the transition from dislocation to diffusion creep. J. Struct. Geol. 33, 1265–1284. https://doi.org/10.1016/j.jsg.2011.05.004

Kirilova, M., Toy, V., Rooney, J.S., Giorgetti, C., Gordon, K.C., Collettini, C., Takeshita, T., 2018. Structural disorder of graphite and implications for graphite thermometry. Solid Earth 9.

Kirilova, M., Toy, V., Sauer, K., Renard, F., Gessner, K., Wirth, R., Xiao, X., Matsumura, R., 2020. Micro- and nano-porosity of the active Alpine Fault zone, New Zealand. Solid Earth 11, 2425–2438. https://doi.org/10.5194/se-11-2425-2020

Kjøll, H.J., Viola, G., Menegon, L., Sørensen, B.E., 2015. Brittle–viscous deformation of vein quartz under fluid-rich lower greenschist facies conditions. Solid Earth 6, 681–699. https://doi.org/10.5194/se-6-681-2015

Koehn, D., Bons, P.D., Hilgers, C. & Passchier, C.W. 2001. Animations of progressive fibrous vein and fringe formation. In: Ailleres, L. and Rawling, T. 2001. Animations in Geology. Journal of the Virtual Explorer, 4.

Kohlstedt, D.L., Evans, B., Mackwell, S.J., 1995. Strength of the lithosphere: Constraints imposed by laboratory experiments. J. Geophys. Res. Solid Earth 100, 17587–17602. https://doi.org/10.1029/95JB01460

Korja, A., Heikkinen, P., 2005. The accretionary Svecofennian orogen—insight from the BABEL profiles. Precambrian Res. 136, 241–268. https://doi.org/10.1016/j.precamres.2004.10.007

Korja, A., Heikkinen, P., Aaro, S., 2001. Crustal structure of the northern Baltic Sea palaeorift. Tectonophysics 331, 341–358. https://doi.org/10.1016/S0040-1951(00)00290-0

Kouketsu, Y., Mizukami, T., Mori, H., Endo, S., Aoya, M., Hara, H., Nakamura, D., Wallis, S., 2014. A new approach to develop the Raman carbonaceous material geothermometer for low-grade metamorphism using peak width. Isl. Arc 23, 33–50. https://doi.org/10.1111/iar.12057

Kukkonen, I.T., Lauri, L.S., 2009. Modelling the thermal evolution of a collisional Precambrian orogen: High heat production migmatitic granites of southern Finland. Precambrian Res. 168, 233–246. https://doi.org/10.1016/j.precamres.2008.10.004

Küster, M., Stöckhert, B., 1999. High differential stress and sublithostatic pore fluid pressure in the ductile regime — microstructural evidence for short-term post-seismic creep in the Sesia Zone, Western Alps. Tectonophysics 303, 263–277. https://doi.org/10.1016/S0040-1951(98)00256-X

Kuva, J., Sammaljärvi, J., Parkkonen, J., Siitari-Kauppi, M., Lehtonen, M., Turpeinen, T., Timonen, J., Voutilainen, M., 2018. Imaging connected porosity of crystalline rock by contrast agent-aided X-ray microtomography and scanning electron microscopy: IMAGING CONNECTED POROSITY OF CRYSTALLINE ROCK. J. Microsc. 270, 98–109. https://doi.org/10.1111/jmi.12661

Kuva, J., Siitari-Kauppi, M., Lindberg, A., Aaltonen, I., Turpeinen, T., Myllys, M., Timonen, J., 2012. Microstructure, porosity and mineralogy around fractures in

Olkiluoto bedrock. Eng. Geol. 139–140, 28–37. https://doi.org/10.1016/j.enggeo.2012.04.008

Kuva, J., Voutilainen, M., Kekäläinen, P., Siitari-Kauppi, M., Timonen, J., Koskinen, L., 2015. Gas Phase Measurements of Porosity, Diffusion Coefficient, and Permeability in Rock Samples from Olkiluoto Bedrock, Finland. Transp. Porous Media 107, 187–204. https://doi.org/10.1007/s11242-014-0432-2

Kyle, J. R., Ketcham, R. A., Kyle, J. R., and Ketcham, R. A.: Application of high resolution X-ray computed tomography to mineral deposit origin, evaluation, and processing, Part 4, 821–839, https://doi.org/10.1016/j.oregeorev.2014.09.034, 2015.

Lafuente, B., Downs, R.T., Yang, H., Stone, N., 2016. The power of databases: the RRUFF project, in: Highlights in Mineralogical Crystallography. Walter de Gruyter GmbH, pp. 1–29.

Lahtinen, R., 1994. Crustal evolution of the Svecofennian and Karelian domains during 2.1 - 1.79 Ga: with special emphasis on the geochemistry and origin of 1.93 - 1.91 Ga gneissic tonalites and associated supracrustal rocks in the Rautalampi area, central Finland ; with 7 tables, Bulletin / Geological Survey of Finland. Geologian Tutkimuskeskus, Espoo.

Lahtinen, R., Korja, A., Nironen, M., 2005. Chapter 11 Paleoproterozoic tectonic evolution, in: Lehtinen, M., Nurmi, P.A., Rämö, O.T. (Eds.), Developments in Precambrian Geology, Precambrian Geology of Finland Key to the Evolution of the Fennoscandian Shield. Elsevier, pp. 481–531. https://doi.org/10.1016/S0166-2635(05)80012-X

Lanari, P., Wagner, T., Vidal, O., 2014. A thermodynamic model for di-trioctahedral chlorite from experimental and natural data in the system MgO–FeO–Al 2 O 3–SiO 2–H 2 O: applications to P–T sections and geothermometry. Contrib. Mineral. Petrol. 167, 968.

Landis, E. N. and D. T. Keane (2010). “X-ray microtomography”. In: Materials Characterization 61, pp. 1305–1316. DOI: 10.1016/j.matchar.2010.09.012.

Lehtonen, M.L., 2005. Kimberlites in Finland: Information about the mantle of the Karelian Craton and implications for diamond exploration. Academic dissertation, University of Helsinki, Finland. http://hdl.handle.net/10138/21180

Macente, A., 2017. 4-DIMENSIONAL STUDIES OF FLUID-ROCK INTERACTION. PhD Thesis, University of Edinburgh.

Mancktelow, N., Grujic, D., Johnson, E., 1998. An SEM study of porosity and grain boundary microstructure in quartz mylonites, Simplon Fault Zone, Central Alps. Contrib. Mineral. Petrol. 131, 71–85. https://doi.org/10.1007/s004100050379

Mänttäri, I., Engstroem, J., Lahaye, Y., Pere, T., 2010. U-Pb ages for PGR dykes, KFP, and adjacent older leucosomic PGRs from ONKALO underground research facility, Olkiluoto, Eurajoki, SW Finland (No. Posiva Working Report 2010-31, Posiva Oy, Eurajoki). Posiva Oy.

Mänttäri, I., Mattila, J., Zwingmann, H., Todd, A.J., 2007. Illite K-Ar dating of fault breccia samples from ONKALO underground research facility, Olkiluoto, Eurajoki, SW Finland. Posiva Oy.

Mänttäri, I., Talikka, M., Paulamäki, S., Mattila, J., 2006. U-Pb ages for tonalitic gneiss, pegmatitic granite, and diabase dyke, Olkiluoto study site, Eurajoki, SW Finland (No. Posiva Working Report 2006-12, Posiva Oy, Eurajoki). Posiva Oy.

Marchesini, B., Garofalo, P.S., Menegon, L., Mattila, J., Viola, G., 2019. Fluid-mediated, brittle–ductile deformation at seismogenic depth – Part 1: Fluid record and deformation history of fault veins in a nuclear waste repository (Olkiluoto Island, Finland). Solid Earth 10, 809–838. https://doi.org/10.5194/se-10-809-2019

Marone, C., Raleigh, C.B., Scholz, C.H., 1990. Frictional behavior and constitutive modeling of simulated fault gouge. J. Geophys. Res. Solid Earth 95, 7007–7025. https://doi.org/10.1029/JB095iB05p07007

Massonne, H.-J., Schreyer, W., 1987. Phengite geobarometry based on the limiting assemblage with K-feldspar, phlogopite, and quartz. Contrib. Mineral. Petrol. 96, 212–224.

Mattila, J., Tammisto, E., 2012. Stress-controlled fluid flow in fractures at the site of a potential nuclear waste repository, Finland. Geology 40, 299–302. https://doi.org/10.1130/G32832.1

Mattila, J., Viola, G., 2014. New constraints on 1.7 Gyr of brittle tectonic evolution in southwestern Finland derived from a structural study at the site of a potential nuclear waste repository (Olkiluoto Island). J. Struct. Geol. 67, 50–74.

Melosh, B.L., Rowe, C.D., Gerbi, C., Smit, L., Macey, P., 2018. Seismic cycle feedbacks in a mid-crustal shear zone. J. Struct. Geol. 112, 95–111. https://doi.org/10.1016/j.jsg.2018.04.004

Menegon, L., Fusseis, F., Stünitz, H., Xiao, X., 2015. Creep cavitation bands control porosity and fluid flow in lower crustal shear zones. Geology 43, 227–230. https://doi.org/10.1130/G36307.1

Menegon, L., Pennacchioni, G., Malaspina, N., Harris, K., Wood, E., 2017. Earthquakes as Precursors of Ductile Shear Zones in the Dry and Strong Lower Crust. Geochem. Geophys. Geosystems 18, 4356–4374. https://doi.org/10.1002/2017GC007189

Menegon, L., Pennacchioni, G., Spiess, R., 2008. Dissolution-precipitation creep of K-feldspar in mid-crustal granite mylonites. J. Struct. Geol. 30, 565–579. https://doi.org/10.1016/j.jsg.2008.02.001

Micklethwaite, S., Cox, S.F., 2004. Fault-segment rupture, aftershock-zone fluid flow, and mineralization. Geology 32, 813–816. https://doi.org/10.1130/G20559.1

Mills, S.G., Gerbi, C., Marsh, J.H., Yates, M.G., Seaman, S.J., White, J.C., 2017. Tectonic and chemical implications of cathodoluminescent microstructures in quartz, Parry Sound domain, Ontario, Canada. Can. J. Earth Sci. 54, 677–692

Mizoguchi, K., Hirose, T., Shimamoto, T., Fukuyama, E., 2008. Internal structure and permeability of the Nojima fault, southwest Japan. J. Struct. Geol. 12.

Modrý, S., Svatá, M., Van Brakel, J., 1981. Thematic bibliography of mercury porosimetry. Powder Technol. 29, 13–43. https://doi.org/10.1016/0032-5910(81)85002-4

Molli, G., Menegon, L., Malasoma, A., 2017. Switching deformation mode and mechanisms during subduction of continental crust: a case study from Alpine Corsica. Solid Earth 8, 767–788. https://doi.org/10.5194/se-8-767-2017

Neimark, A. V., and Ravikovitch, P. I., 1997, Calibration of pore volume in adsorption experiments and theoretical models, Langmuir, 13, 5148–60

Nguyen, P.T., Harris, L.B., Powell, C.M., Cox, S.F., 1998. Fault-valve behaviour in optimally oriented shear zones: an example at the Revenge gold mine, Kambalda, Western Australia. J. Struct. Geol. 20, 1625–1640. https://doi.org/10.1016/S0191-8141(98)00054-6

Niemeijer, A.R., Spiers, C.J., 2005. Influence of phyllosilicates on fault strength in the brittle-ductile transition: insights from rock analogue experiments. Geol. Soc. Lond. Spec. Publ. 245, 303–327. https://doi.org/10.1144/GSL.SP.2005.245.01.15

Nironen, M., 1997. The Svecofennian Orogen: a tectonic model. Precambrian Res. 86, 21–44.

Nironen, M. 2017. Guide to the Geological Map of Finland – Bedrock 1:1 000 000. In: Nironen, M. (ed.) Bedrock of Finland at the scale 1:1 000 000 - Major stratigraphic units, metamorphism and tectonic evolution. Geological Survey of Finland, Special Paper 60, 41−76.

Nishimoto, S., Yoshida, H., 2010. Hydrothermal alteration of deep fractured granite: Effects of dissolution and precipitation. Lithos 115, 153–162. https://doi.org/10.1016/j.lithos.2009.11.015

Norberg, N., Neusser, G., Wirth, R., Harlov, D., 2011. Microstructural evolution during experimental albitization of K-rich alkali feldspar. Contrib. Mineral. Petrol. 162, 531–546. https://doi.org/10.1007/s00410-011-0610-y

Nordbäck, N., Mattila, J., 2018. Brittle Fault Systems of the ONKALO Underground Research Facility.

Nordbäck, N., Mattila, J., Zwingmann, H., Viola, G., 2022. Precambrian fault reactivation revealed by structural and K-Ar geochronological data from the spent nuclear fuel repository in Olkiluoto, southwestern Finland. Tectonophysics 824, 229208. https://doi.org/10.1016/j.tecto.2022.229208

Öhman, I., Heikkinen, E., Säävuori, H., Vuoriainen, S., Paulamäki, S., Aaltonen, I., 2009. Summary of petrophysical analysis of Olkiluoto core samples 1990-2008, Work reports 2009-11.

Oliver, N.H.S., 1996. Review and classification of structural controls on fluid flow during regional metamorphism. J. Metamorph. Geol. 14, 477–492. https://doi.org/10.1046/j.1525-1314.1996.00347.x

Oliver, N.H.S., Bons, P.D., 2001. Mechanisms of fluid flow and fluid–rock interaction in fossil metamorphic hydrothermal systems inferred from vein–wallrock patterns, geometry and microstructure. Geofluids 1, 137–162. https://doi.org/10.1046/j.1468-8123.2001.00013.x

Pajunen, M., Airo, M., Elminen, T., Mänttäri, I., Niemelä, R., Vaarma, M., Wasenius, P., Wennerström, M., 2008. Tectonic evolution of the Svecofennian crust in southern Finland. Geol. Surv. Finl. Spec. Pap. 47, 15–160.

Peacock, D., Nixon, C., Rotevatn, A., Sanderson, D., Zuluaga, L., 2016. Glossary of fault and other fracture networks. J. Struct. Geol. 92. https://doi.org/10.1016/j.jsg.2016.09.008

Peacock, D.C.P., Sanderson, D.J., 2018. Structural analyses and fracture network characterisation: Seven pillars of wisdom. Earth-Sci. Rev. 184, 13–28. https://doi.org/10.1016/j.earscirev.2018.06.006

Pennacchioni, G., Mancktelow, N.S., 2007. Nucleation and initial growth of a shear zone network within compositionally and structurally heterogeneous granitoids under amphibolite facies conditions. J. Struct. Geol. 29, 1757–1780. https://doi.org/10.1016/j.jsg.2007.06.002

Pere, T., 2009. Fault-related local phenomena in the bedrock of Olkiluoto with particular reference to fault zone OL-BFZ100. Posiva Oy.

Perona, P., Malik, J., 1990. Scale-space and edge detection using anisotropic diffusion. IEEE Trans. Pattern Anal. Mach. Intell. 12, 629–639. https://doi.org/10.1109/34.56205

Pfiffner, O.A., 2016. Basement-involved thin-skinned and thick-skinned tectonics in the Alps. Geol. Mag. 153, 1085–1109. https://doi.org/10.1017/S0016756815001090

Platt, J.P., Vissers, R.L.M., 1980. Extensional structures in anisotropic rocks. J. Struct. Geol. 2, 397–410. https://doi.org/10.1016/0191-8141(80)90002-4

Plümper, O., Botan, A., Los, C., Liu, Y., Malthe-Sørenssen, A., Jamtveit, B., 2017. Fluid-driven metamorphism of the continental crust governed by nanoscale fluid flow. Nat. Geosci. 10, 685–690. https://doi.org/10.1038/ngeo3009

Plümper, O., Putnis, A., 2009. The Complex Hydrothermal History of Granitic Rocks: Multiple Feldspar Replacement Reactions under Subsolidus Conditions. J. Petrol. 50, 967–987. https://doi.org/10.1093/petrology/egp028

Prando, F., Menegon, L., Anderson, M.W., Marchesini, B., Mattila, J., Viola, G., 2020. Fluid-mediated, brittle-ductile deformation at seismogenic depth: Part II – Stress history and fluid pressure variations in a shear zone in a nuclear waste repository (Olkiluoto Island, Finland) 41

Précigout, J., Ledoux, E., Arbaret, L., Spriet, C., 2022. Porosity induced by dislocation dynamics in quartz-rich shear bands of granitic rocks. Sci. Rep. 12, 6141. https://doi.org/10.1038/s41598-022-10053-x

Précigout, J., Stünitz, H., Villeneuve, J., 2019. Excess water storage induced by viscous strain localization during high-pressure shear experiment. Sci. Rep. 9, 3463. https://doi.org/10.1038/s41598-019-40020-y

Prieto, G.A., Froment, B., Yu, C., Poli, P., Abercrombie, R., 2017. Earthquake rupture below the brittle-ductile transition in continental lithospheric mantle. Sci. Adv. 3, e1602642. https://doi.org/10.1126/sciadv.1602642

Prior, D.J., Mariani, E., Wheeler, J., 2009. EBSD in the Earth Sciences: Applications, Common Practice, and Challenges. In: Schwartz A., Kumar M., Adams B., Field D. (eds), in: Electron Backscatter Diffraction in Materials Science. Springer, Boston, MA.

Putnis, A., 2015. Transient Porosity Resulting from Fluid–Mineral Interaction and its Consequences. Rev. Mineral. Geochem. 80, 1–23. https://doi.org/10.2138/rmg.2015.80.01

Ranalli, G., 1997. Rheology of the lithosphere in space and time. Geol. Soc. Lond. Spec. Publ. 121, 19–37. https://doi.org/10.1144/GSL.SP.1997.121.01.02

Reed SJ. Electron microprobe analysis and scanning electron microscopy in geology. Cambridge university press; 2005 Aug 25.

Renard, F., Gratier, J.-P., Jamtveit, B., 2000. Kinetics of crack-sealing, intergranular pressure solution, and compaction around active faults. J. Struct. Geol. 22, 1395–1407. https://doi.org/10.1016/S0191-8141(00)00064-X

Rouquerol, J., Avnir, D., Fairbridge, C.W., Everett, D.H., Haynes, J.H., Pernicone, N., Ramsay, J.D.F., Sing, K.S.W., Unger, K.K., 1994. Recommendations for the Characterization of Porous Solids. https://doi.org/10.1515/iupac.66.0925

Saintot, A., Stephens, M., Viola, G., Nordgulen, Ø., 2011. Brittle tectonic evolution and paleostress field reconstruction in the southwestern part of the Fennoscandian Shield, Forsmark, Sweden. Tectonics 30.

Salmas, C., Androutsopoulos, G., 2001. Mercury Porosimetry: Contact Angle Hysteresis of Materials with Controlled Pore Structure. J. Colloid Interface Sci. 239, 178–189. https://doi.org/10.1006/jcis.2001.7531

Sammaljärvi, J., Lindberg, A., Voutilainen, M., Ikonen, J., Siitari-Kauppi, M., Pitkänen, P., Koskinen, L., 2017. Multi-scale study of the mineral porosity of veined gneiss and pegmatitic granite from Olkiluoto, Western Finland. J. Radioanal. Nucl. Chem. 314, 1557–1575. https://doi.org/10.1007/s10967-017-5530-5

Sasanian, S., Newson, T.A., 2013. Use of mercury intrusion porosimetry for microstructural investigation of reconstituted clays at high water contents. Eng. Geol. 158, 15–22. https://doi.org/10.1016/j.enggeo.2013.03.002

Schindelin, J., Arganda-Carreras, I., Frise, E., Kaynig, V., Longair, M., Pietzsch, T., Preibisch, S., Rueden, C., Saalfeld, S., Schmid, B., Tinevez, J.-Y., White, D.J., Hartenstein, V., Eliceiri, K., Tomancak, P., Cardona, A., 2012. Fiji: an open-source platform for biological-image analysis. Nat. Methods 9, 676–682. https://doi.org/10.1038/nmeth.2019

Schlüter, S., Sheppard, A., Brown, K., Wildenschild, D., 2014. Image processing of multiphase images obtained via X-ray microtomography: A review. Water Resour. Res. 50, 3615–3639. https://doi.org/10.1002/2014WR015256

Scholz, C.H., 1998. Earthquakes and friction laws. Nature 391, 37. https://doi.org/10.1038/34097

Scholz, C.H., 2002. The mechanics of earthquakes and faulting. Cambridge university press

Schreurs, G., 2003. Fault development and interaction in distributed strike-slip shear zones: an experimental approach, in: Storti, F., Holdsworth, R.E., Salvini, F. (Eds.), Intraplate Strike-Slip Deformation Belts. Geological Society of London, p. 0. https://doi.org/10.1144/GSL.SP.2003.210.01.03

Schulz, B., Audren, C., Triboulet, C., 2002. Oxygen isotope record of fluid–rock–SiO2 interaction during Variscan progressive deformation and quartz veining in the meta-volcanosediments of Belle-Ile (Southern Brittany). J. Struct. Geol. 24, 1281–1297. https://doi.org/10.1016/S0191-8141(01)00135-3

Sibson, R.H., 1982. Fault zone models, heat flow, and the depth distribution of earthquakes in the continental crust of the United States. Bull. Seismol. Soc. Am. 72, 151–163.

Sibson, R.H., 1987. Earthquake rupturing as a mineralizing agent in hydrothermal systems. Geology 15, 701–704. https://doi.org/10.1130/0091-7613(1987)15<701:ERAAMA>2.0.CO;2

Sibson, R.H., 1989. Earthquake faulting as a structural process. J. Struct. Geol. 11, 1–14. https://doi.org/10.1016/0191-8141(89)90032-1

Sibson, R.H., 1990. Conditions for fault-valve behaviour. Geol. Soc. Lond. Spec. Publ. 54, 15–28. https://doi.org/10.1144/GSL.SP.1990.054.01.02

Sibson, R.H., 1992. Implications of fault-valve behaviour for rupture nucleation and recurrence. Tectonophysics 211, 283–293. https://doi.org/10.1016/0040-1951(92)90065-E

Sibson, R.H., 1993. Load-strengthening versus load-weakening faulting. J. Struct. Geol. 15, 123–128. https://doi.org/10.1016/0191-8141(93)90090-W

Sibson, R.H., 2000. Fluid involvement in normal faulting. J. Geodyn. 29, 469–499. https://doi.org/10.1016/S0264-3707(99)00042-3

Sibson, R.H., 1996. Structural permeability of fluid-driven fault-fracture meshes. J. Struct. Geol. 18, 1031–1042. https://doi.org/10.1016/0191-8141(96)00032-6

Sibson, R.H., 2001. Seismogenic Framework for Hydrothermal Transport and Ore Deposition, in: Richards, J.P., Tosdal, R.M. (Eds.), Structural Controls on Ore Genesis. Society of Economic Geologists, p. 0. https://doi.org/10.5382/Rev.14.02

Sibson, R.H., Rowland, J.V., 2003. Stress, fluid pressure and structural permeability in seismogenic crust, North Island, New Zealand. Geophys. J. Int. 154, 584–594. https://doi.org/10.1046/j.1365-246X.2003.01965.x

Siitari-Kauppi, M.K., Lindberg, A., Ikonen, J.O., Kauppi, I., 2010. Investigation of Porosity and Pore Structure by PMMA Method of Samples Taken from Deep Drillholes OL-KR38 and OL-KR39. Posiva.

Sing, K.S.W., 2004. Characterization of porous materials: past, present and future. Colloids Surf. Physicochem. Eng. Asp., Proceedings of the Third International TRI/Princeton Workshop "Characterization of Porous Materials: from Angstroms to Millimeters" 241, 3–7. https://doi.org/10.1016/j.colsurfa.2004.04.003

Skyttä, P., Torvela, T., 2018. Brittle reactivation of ductile precursor structures: The role of incomplete structural transposition at a nuclear waste disposal site, Olkiluoto, Finland. J. Struct. Geol. 116, 253–259.

Smith, E., and Dent G. "Modern Raman spectroscopy: a practical approach." (2005,2019): 129-150.

Smith, J.V., 1997. Initiation of convergent extension fracture vein arrays by displacement of discontinuous fault segments. J. Struct. Geol. 19, 1369–1373. https://doi.org/10.1016/S0191-8141(97)00054-0

Song, W.J., Johnson, S.E., Gerbi, C.C., 2020. Quartz fluid inclusion abundance and off-fault damage in a deeply exhumed, strike-slip, seismogenic fault. J. Struct. Geol. 139, 104118. https://doi.org/10.1016/j.jsg.2020.104118

Staněk, M., Géraud, Y., 2019. Granite microporosity changes due to fracturing and alteration: secondary mineral phases as proxies for porosity and permeability estimation. Solid Earth 10, 251–274. https://doi.org/10.5194/se-10-251-2019

Stewart, C.A., Miranda, E.A., 2017. The Rheological Evolution of Brittle-Ductile Transition Rocks During the Earthquake Cycle: Evidence for a Ductile Precursor to Pseudotachylyte in an Extensional Fault System, South Mountains, Arizona. J. Geophys. Res. Solid Earth 122, 10,643-10,665. https://doi.org/10.1002/2017JB014680

Stipp, M., Kunze, K., 2008. Dynamic recrystallization near the brittle-plastic transition in naturally and experimentally deformed quartz aggregates. Tectonophysics 448, 77–97. https://doi.org/10.1016/j.tecto.2007.11.041

Stipp, M., Stünitz, H., Heilbronner, R., Schmid, S.M., 2002. The eastern Tonale fault zone: a 'natural laboratory' for crystal plastic deformation of quartz over a temperature range from 250 to 700°C. J. Struct. Geol. 24, 1861–1884. https://doi.org/10.1016/S0191-8141(02)00035-4

Stipp, M., Tullis, J., 2003. The recrystallized grain size piezometer for quartz. Geophys. Res. Lett. 30. https://doi.org/10.1029/2003GL018444

Stipp, M., Tullis, J., Scherwath, M., Behrmann, J.H., 2010. A new perspective on paleopiezometry: Dynamically recrystallized grain size distributions indicate mechanism changes. Geology 38, 759–762. https://doi.org/10.1130/G31162.1

Streit, J.E., Cox, S.F., 2001. Fluid pressures at hypocenters of moderate to large earthquakes. J. Geophys. Res. Solid Earth 106, 2235–2243. https://doi.org/10.1029/2000JB900359

Stünitz, H., Fitz Gerald, J.D., Tullis, J., 2003. Dislocation generation, slip systems, and dynamic recrystallization in experimentally deformed plagioclase single crystals. Tectonophysics 372, 215–233. https://doi.org/10.1016/S0040-1951(03)00241-5

Suominen, V., 1991. The chronostratigraphy of southwestern Finland with special reference to Postjotnian and Subjotnian diabases, Bulletin / Geological Survey of Finland. Espoo.

Supek, F., Peharec, P., Krsnik-Rasol, M., Šmuc, T., 2008. Enhanced analytical power of SDS-PAGE using machine learning algorithms. PROTEOMICS 8, 28–31. https://doi.org/10.1002/pmic.200700555

Talu, O., and Myers, A., 2001, Molecular simulation of adsorption: Gibbs dividing surface and comparison with experiment, AIChE Journal, 47, 1160–8.

Tamari, S., 2004, Optimum design of the constant-volume gas pycnometer for determining the volume of solid particles, Measurement Science and Technology, 15, 549–58.

Tiensuu, K., Heikkinen, E., Ravimo, I., Kiuru, R., 2017. Geophysical logging and imaging of drillholes OL-KR56, OLKR57 and OL-KR57B at Olkiluoto in 2012-2015: Working Report 2016-58

Tillberg, M., Drake, H., Zack, T., Hogmalm, J., Kooijman, E., Åström, M., 2021. Reconstructing craton-scale tectonic events via in situ Rb-Sr geochronology of poly-phased vein mineralization. Terra Nova 33, 502–510. https://doi.org/10.1111/ter.12542.

Torgersen, E., Viola, G., Zwingmann, H., Harris, C., 2015. Structural and temporal evolution of a reactivated brittle–ductile fault – Part II: Timing of fault initiation and reactivation by K–Ar dating of synkinematic illite/muscovite. Earth Planet. Sci. Lett. 410, 212–224. https://doi.org/10.1016/j.epsl.2014.09.051

Torvela, T., Ehlers, C., 2010. From ductile to brittle deformation: structural development and strain distribution along a crustal-scale shear zone in SW Finland. Int. J. Earth Sci. 99, 1133–1152.

Torvela, T., Mänttäri, I., Hermansson, T., 2008. Timing of deformation phases within the South Finland shear zone, SW Finland. Precambrian Res. 160, 277–298. https://doi.org/10.1016/j.precamres.2007.08.002

Trepmann, C.A., Hsu, C., Hentschel, F., Döhler, K., Schneider, C., Wichmann, V., 2017. Recrystallization of quartz after low-temperature plasticity – The record of stress relaxation below the seismogenic zone. J. Struct. Geol. 95, 77–92. https://doi.org/10.1016/j.jsg.2016.12.004

Trepmann, C.A., Seybold, L., 2019. Deformation at low and high stress-loading rates. Geosci. Front. 10, 43–54. https://doi.org/10.1016/j.gsf.2018.05.002

Trepmann, C.A., Stöckhert, B., 2003. Quartz microstructures developed during non-steady state plastic flow at rapidly decaying stress and strain rate. J. Struct. Geol. 25, 2035–2051. https://doi.org/10.1016/S0191-8141(03)00073-7

Trepmann, C.A., Stöckhert, B., 2013. Short-wavelength undulatory extinction in quartz recording coseismic deformation in the middle crust – an experimental study. Solid Earth 4, 263–276. https://doi.org/10.5194/se-4-263-2013

Trepmann, C.A., Stöckhert, B., Dorner, D., Moghadam, R.H., Küster, M., Röller, K., 2007. Simulating coseismic deformation of quartz in the middle crust and fabric evolution during postseismic stress relaxation — An experimental study. Tectonophysics 442, 83–104. https://doi.org/10.1016/j.tecto.2007.05.005

Tschumperle, D., Deriche, R., 2005. Vector-Valued Image Regularization with PDEs: A Common Framework for Different Applications. IEEE Trans. PATTERN Anal. Mach. Intell. 27.

Tuisku, P., Kärki, A., 2010. Metamorphic petrology of Olkiluoto. Posiva Oy.

Tullborg, E.-L., Larson, S.Å., 2006. Porosity in crystalline rocks – A matter of scale. Eng. Geol. 84, 75–83. https://doi.org/10.1016/j.enggeo.2005.12.001

Urai, J.L., Williams, P.F., van Roermund, H.L.M., 1991. Kinematics of crystal growth in syntectonic fibrous veins. J. Struct. Geol. 13, 823–836. https://doi.org/10.1016/0191-8141(91)90007-6

Vaasjoki, M., Korsman, K., Koistinen, T., 2005. Chapter 1 Over view, in: Developments in Precambrian Geology. Elsevier, pp. 1–17. https://doi.org/10.1016/S0166-2635(05)80002-7

Viola, G., Mancktelow, N.S., Miller, J.A., 2006. Cyclic frictional-viscous slip oscillations along the base of an advancing nappe complex: Insights into brittle-ductile nappe emplacement mechanisms from the Naukluft Nappe Complex, central Namibia. Tectonics 25. https://doi.org/10.1029/2005TC001939

Viola, G., Venvik Ganerød, G., Wahlgren, C.-H., 2009. Unraveling 1.5 Ga of brittle deformation history in the Laxemar-Simpevarp area, southeast Sweden: A contribution to the Swedish site investigation study for the disposal of highly radioactive nuclear waste. Tectonics 28. https://doi.org/10.1029/2009TC002461

Viola, G., Mattila, J., Zwingmann, H., Todd, A., & Raven, M. (2011). Structural and K/Ar Illite geochronological constraints on the brittle deformation history of the Olkiluoto Region, Southwest Finland (No. POSIVA-WR--11-37). Posiva Oy

Violay, M., Heap, M.J., Acosta, M., Madonna, C., 2017. Porosity evolution at the brittle-ductile transition in the continental crust: Implications for deep hydro-geothermal circulation. Sci. Rep. 7, 7705. https://doi.org/10.1038/s41598-017-08108-5

Voorn, M., Exner, U., Barnhoorn, A., Baud, P., Reuschlé, T., 2015. Porosity, permeability and 3D fracture network characterisation of dolomite reservoir rock samples. J. Pet. Sci. Eng. 127, 270–285. https://doi.org/10.1016/j.petrol.2014.12.019

Voutilainen, M., Siitari-Kauppi, M., Sardini, P., Lindberg, A., Timonen, J., 2012. Pore-space characterization of an altered tonalite by X-ray computed microtomography and the14C-labeled-polymethylmethacrylate method. J. Geophys. Res. Solid Earth 117. https://doi.org/10.1029/2011JB008622

Walker, F.D., Lee, M., Parsons, I., n.d. Micropores and micropermeable texture in alkali feldspars: geochemical and geophysical implications 30.

Wardlaw, N. C. and McKellar, M.: Mercury porosimetry and the interpretation of pore geometry in sedimentary rocks and artificial models, Powder Technol., 29(1), 127–143, doi:10.1016/0032-5910(81)85011-5, 1981.

Wardlaw, N. C., Li, Y. and Forbes, D.: Pore-throat size correlation from capillary pressure curves, Transp. Porous Media, 2(6), doi:10.1007/BF00192157, 1987.

Washburn, E.W., 1921. The Dynamics of Capillary Flow. Phys. Rev. 17, 273–283. https://doi.org/10.1103/PhysRev.17.273

Webb, P. A.: An Introduction To The Physical Characterization of Materials by Mercury Intrusion Porosimetry with Emphasis On Reduction And Presentation of Experimental Data, 23, 2001.

Weber, J., and Bastick, M., 1968, Influence de la température sur la détermination de la masse volumique de divers carbones par pycnométrie dans l'helium, Bulletin de la Société Chimique de France, 7, 2702–6.

Wehrens, P., Berger, A., Peters, M., Spillmann, T., Herwegh, M., 2016. Deformation at the frictional-viscous transition: Evidence for cycles of fluid-assisted embrittlement and ductile deformation in the granitoid crust. Tectonophysics 693, 66–84. https://doi.org/10.1016/j.tecto.2016.10.022

White, S.H., Burrows, S.E., Carreras, J., Shaw, N.D., Humphreys, F.J., 1980. On mylonites in ductile shear zones. Shear Zones Rocks 2, 175–187. https://doi.org/10.1016/0191-8141(80)90048-6

White, J.C., 1996. Transient discontinuities revisited: pseudotachylyte, plastic instability and the influence of low pore fluid pressure on deformation processes in the mid-crust. J. Struct. Geol. 18, 1471–1486. https://doi.org/10.1016/S0191-8141(96)00059-4

White, J.C., 2012. Paradoxical pseudotachylyte – Fault melt outside the seismogenic zone. J. Struct. Geol., Physico-Chemical Processes in Seismic Faults 38, 11–20. https://doi.org/10.1016/j.jsg.2011.11.016

Wildenschild, D. and Sheppard, A. P.: X-ray imaging and analysis techniques for quantifying pore-scale structure and processes in subsurface porous medium systems, Advances in Water Resources, 51, 217–246, https://doi.org/10.1016/j.advwatres.2012.07.018, 2013.

Wilson, J.E., Chester, J.S., Chester, F.M., 2003. Microfracture analysis of fault growth and wear processes, Punchbowl Fault, San Andreas system, California. J. Struct. Geol. 25, 1855–1873. https://doi.org/10.1016/S0191-8141(03)00036-1

Wirth, R., Kruhl, J.H., Morales, L.F.G., Schreiber, A., 2022. Partially open grain and phase boundaries as fluid pathways in metamorphic and magmatic rocks. J. Metamorph. Geol. 40, 67–85. https://doi.org/10.1111/jmg.12610

Withers, P.J., Bouman, C., Carmignato, S. et al. X-ray computed tomography. Nat Rev Methods Primers 1, 18 (2021). https://doi.org/10.1038/s43586-021-00015-4

Woodcock, N.H., Mort, K., 2008. Classification of fault breccias and related fault rocks. Geol. Mag. 145, 435–440. https://doi.org/10.1017/S0016756808004883

Worden, R.H., Walker, F.D.L., Parsons, I., Brown, W.L., 1990. Development of microporosity, diffusion channels and deuteric coarsening in perthitic alkali feldspars. Contrib. Mineral. Petrol. 104, 507–515. https://doi.org/10.1007/BF00306660

Xing, T., Zhu, W., Fusseis, F., Lisabeth, H., 2018. Generating porosity during olivine carbonation via dissolution channels and expansion cracks. Solid Earth 9, 879–896. https://doi.org/10.5194/se-9-879-2018

Yardley, B., Baumgartner, L., 2007. Fluid processes in deep crustal fault zones. Tecton. Faults–Agents Change Dyn. Earth 295–318.

Zhang, Z., Kruschwitz, S., Weller, A., Halisch, M., 2018. Enhanced pore space analysis by use of μ-CT, MIP, NMR, and SIP. Solid Earth 9, 1225–1238. https://doi.org/10.5194/se-9-1225-2018

Appendix A

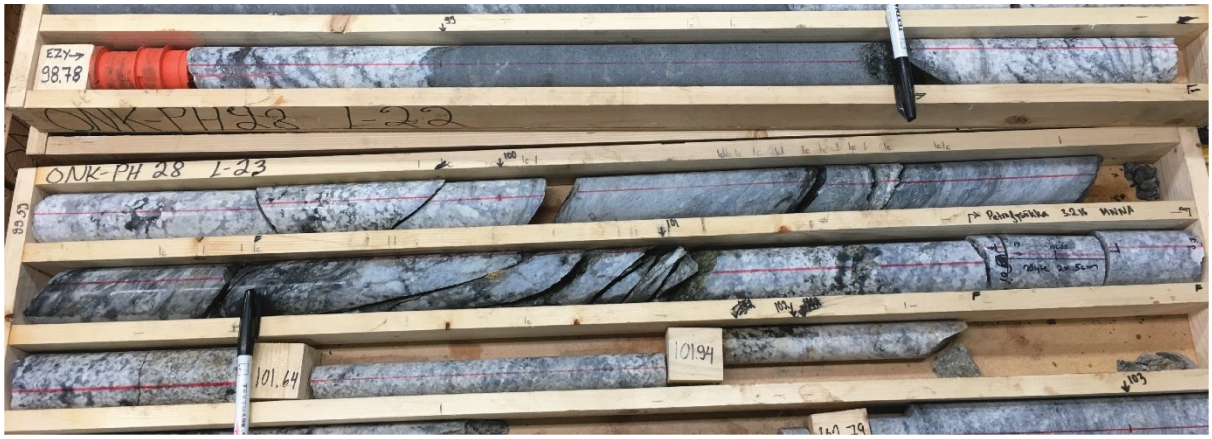

Figure A 4 Photo of selected dill cores. Core section from horizontal drill core ONK_PH28. Photo shows the extracted core length at the 98.78- 102.13 m distance from the start of the drill core

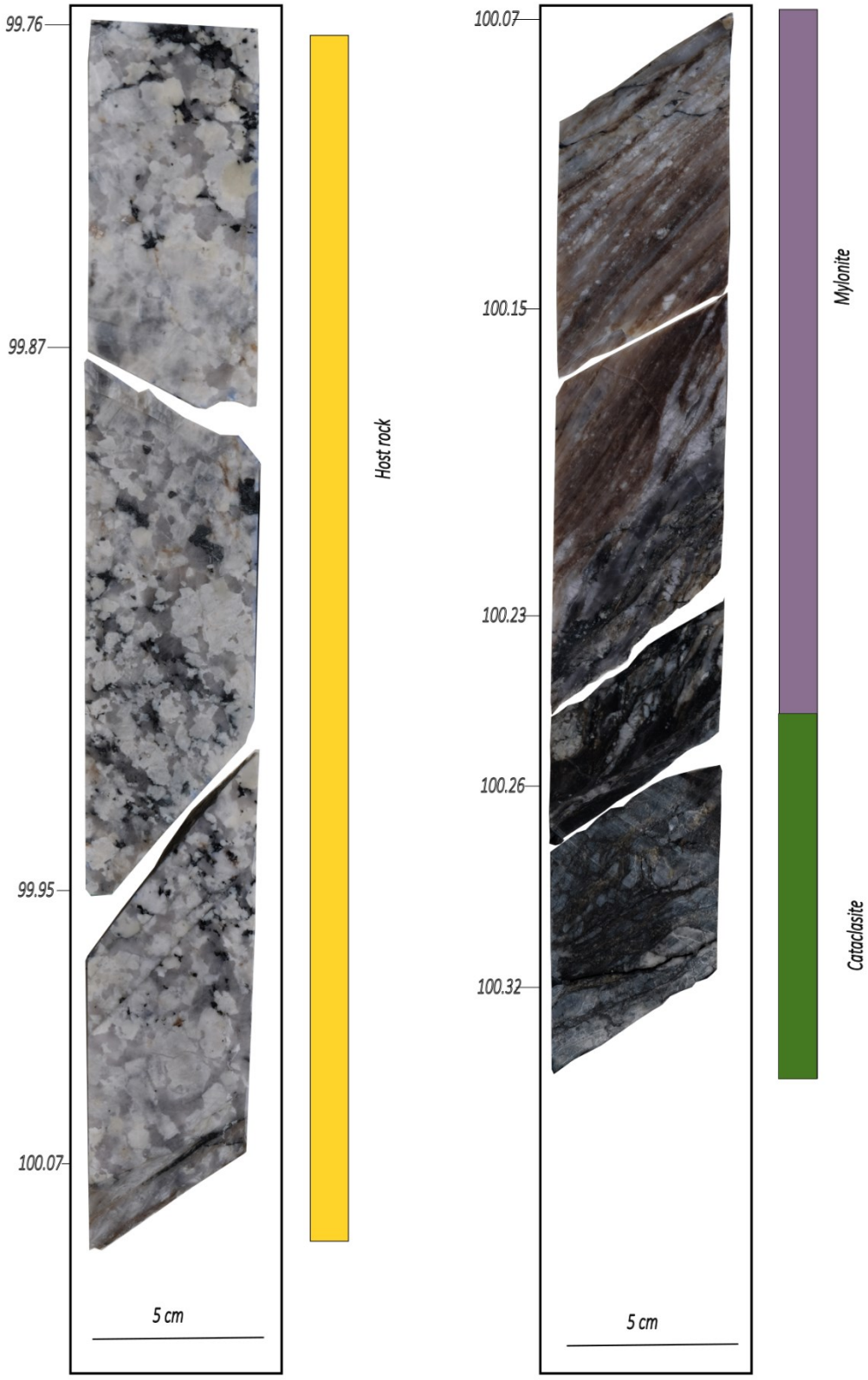

Figure A 5 Scans of ONK_PH28 upper half-core and schematic diagram of the sampled lithologies from core descriptions and -photos. Represented section at 99.76- 100.32 m distance from the start of the drill core. Separation of the pieces of drill core are due to open fractures occurring during the core extraction or to subsequent sample preparation. Comprehensive descriptions of drill core is provided in Chapter 3.

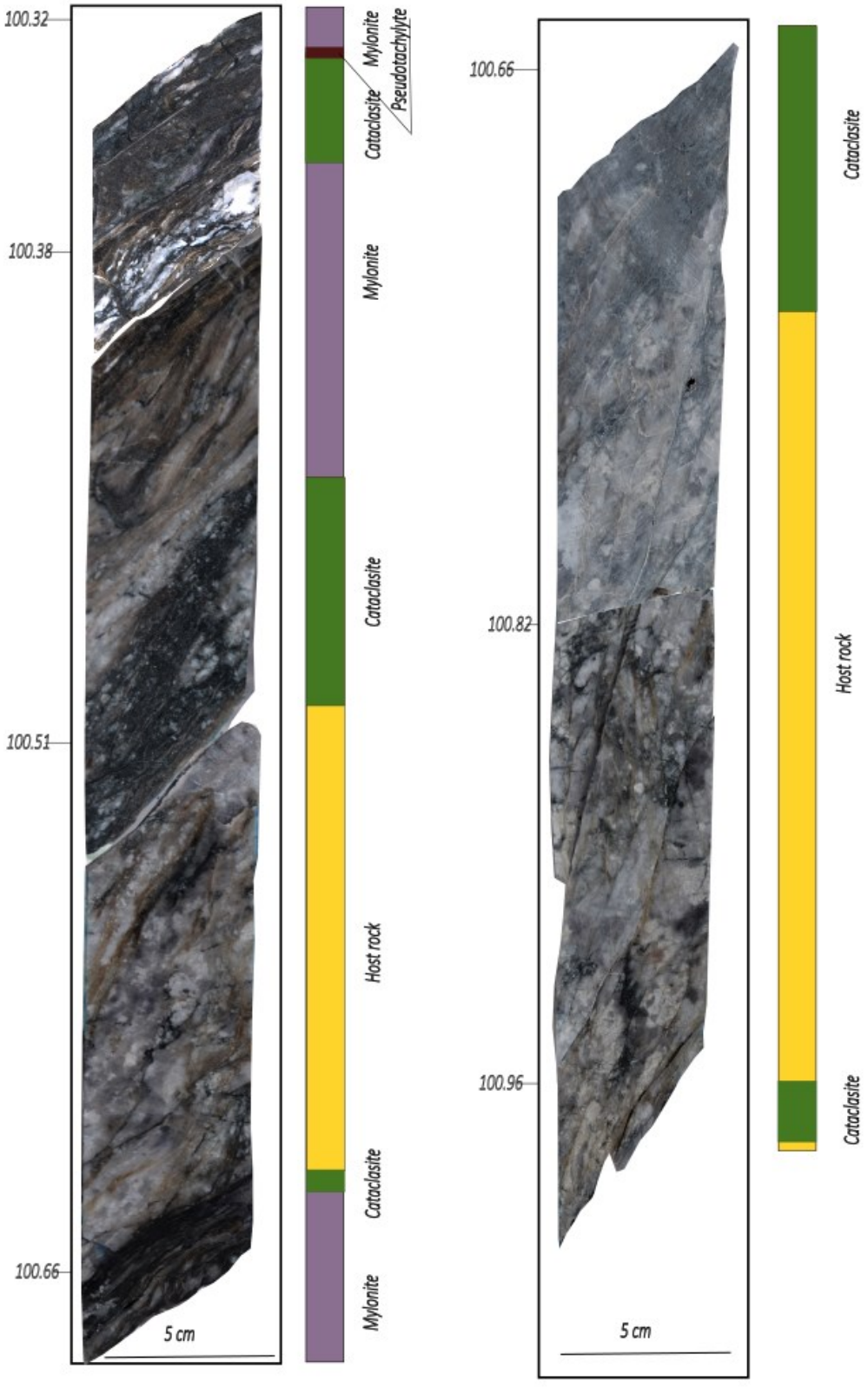

Figure A 6 Scans of ONK_PH28 upper half-core and schematic diagram of the sampled lithologies from core descriptions and -photos. Represented section at 100.32- 102.13 m distance from the start of the drill core. Comprehensive descriptions of drill core is provided in Chapter 3.